ABSTRACT

Title of Dissertation: THE TIBETAN PLATEAU SURFACE ENERGY BUDGET AND ITS TELECONNECTION WITH THE EAST ASIAN SUMMER MONSOON: EVIDENCE FROM GROUND OBSERVATIONS, REMOTE SENSING, AND REANALYSIS DATASETS

Qinqing Shi, Doctor of Philosophy, 2015

Dissertation directed by: Dr. Shunlin Liang, Professor
Department of Geographical Sciences

Estimations from meteorological stations indicate that the surface sensible heat flux over the Tibetan Plateau has been decreasing continuously since the 1980s. Modeling studies suggest that such change is physically linked to the weakening of the East Asian summer monsoon through Rossby wave trains. However, the relationship between the surface energy budget over the entire Tibetan Plateau and the East Asian summer monsoon rainfall has rarely been examined.

The objective of this study is to quantify the relationship between the surface energy budget over the Tibetan Plateau and the East Asian summer monsoon, using ground observations, remote sensing, and reanalysis datasets with three specific questions: What are the spatiotemporal characteristics of the surface radiation and energy budgets over the Tibetan Plateau in recent decades? How does the interannual variation of the surface radiation and energy budgets correlate to, respond to, and impact the

observed regional surface and atmospheric anomalies? And can the changes of the surface energy budget component over the Tibetan Plateau explain the weakening of the East Asian summer monsoon and associated precipitation changes in China?

To address those questions, I 1) develop a fused monthly surface radiation and energy budgets dataset over the Tibetan Plateau using ground and satellite observations and reanalysis datasets; 2) analyze the spatial distribution of the fused surface radiation and energy budgets, and assess its correlations with the observed surface and atmospheric conditions over the Tibetan Plateau; and 3) test the hypothesis of whether the Asian summer monsoon rainfall is under the impact of the spring sensible heat flux over the Tibetan Plateau through correlation analysis, regression analysis, Granger causality test, and composite analysis.

The root mean square errors from cross validation are 18.9 Wm^{-2}, 10.3 Wm^{-2}, 14.3 Wm^{-2} for the fused monthly surface net radiation, latent heat flux, and sensible heat flux. The fused downward shortwave irradiance, sensible heat flux, and latent heat flux anomalies are consistent with those estimated from meteorological stations. The associations among the fused surface radiation and energy budgets and the related surface anomalies such as mean temperature, temperature range, snow cover, and Normalized Difference Vegetation Index in addition to the atmospheric anomalies such as cloud cover and water vapor show seasonal dependence over the Tibetan Plateau. The decreased late spring sensible heat flux, which is sustained throughout the summer, has been associated with suppressed summer rainfall in the north of China and the north of Indian and enhanced rainfall in the west of India. The mechanism of those associations is found through a lower-level Rossby wave train as a result of anomalous sensible heating

over the Tibetan Plateau. The decreased late spring sensible heat flux has also been associated with dry weather in the Yangtze River basin through a descending motion to the east of the Tibetan Plateau.

This dissertation is the first synthesized analysis of the surface radiation and energy budgets at a spatial scale covering the entire Tibetan Plateau over a temporal period of two decades. The results of this study could contribute to a better understanding of the land-atmosphere interactions over the Tibetan Plateau, and the role of the Tibetan Plateau sensible heating in regulating the strength of the Asian summer monsoon. This study demonstrates a linkage between the spring sensible heat over the Tibetan Plateau and the Asian summer monsoon rainfall that affect about one fourth of the world's population, which has implications that will benefit local agriculture practices, disaster management, and climate change mitigation.

THE TIBETAN PLATEAU SURFACE ENERGY BUDGET AND ITS TELECONNECTION WITH THE EAST ASIAN SUMMER MONSOON: EVIDENCE FROM GROUND OBSERVATIONS, REMOTE SENSING, AND REANALYSIS DATASETS

by

Qinqing Shi

Dissertation submitted to the Faculty of the Graduate School of the
University of Maryland, College Park, in partial fulfillment
of the requirements for the degree of
Doctor of Philosophy
2015

Advisory Committee:

Professor Shunlin Liang, Chair
Professor John R. Townshend
Professor Samuel N. Goward
Professor Ralph Dubayah
Professor Rachel T. Pinker
Dr. Muthuvel Chelliah

Dedication

To my parents.

Acknowledgements

I would like to particular thank Dr. Shunlin Liang for all his guidance and support as my advisor. He is the person who introduced me into the world of scientific research, inspired me with new ideas, and encouraged me to overcome challenges. I also would like to express my appreciation to all of my committee members, Dr. John R. Townshend, Dr. Samuel N. Goward, Dr. Ralph Dubayah, and Dr. Rachel T. Pinker, and Dr. Muthuvel Chelliah, for their continuous help and critical suggestions.

In addition, special thanks to my colleagues in our research group, including Dr. Dongdong Wang, Dr. Tao He, Dr. Wonkook Kim, Dr. Xiufang Zhu, Dr. Bo Jiang, Dr. Yuzhen Zhang, Dr. Quanfang Wang, Dr. Lin Sun, Dr. Fengming Hui, Dr. Junmin Liu, Xin Tao, Yuan Zhou, Yunfeng Cao, Xiaona Chen, Yuhan Rao, Yi Zhang, Zhen Song, Hongya Zhang, and Meredith G. L. Brown, for their instructive discussions and selfless help.

Finally, I am grateful for the endless love and support from my parents and my husband. Without their blessings and encouragement, I would not have been able to complete this dissertation.

I would also like to thank the National Oceanic and Atmospheric Administration and the Chinese Scholarship Council for their financial support.

Table of Contents

List of Tables

List of Figures

Chapter 1 Introduction

1.1 Background

The Tibetan Plateau is the highest plateau on Earth, covering proximately one fourth of the total land of the China (about 25 million km^2). The Tibetan Plateau is defined as area within 75–105°E and 26°N–40°N at elevations above 3000m (Figure 1-1). The average elevation of the Tibetan Plateau is about 4500 m, reaching the middle troposphere and impacting atmospheric circulation through mechanical forcing, partitioning the jet stream so that it descends in the north (causing the dry climate in northwest China) and ascends in the south (corresponding to the warm, wet climate of Yunnan Province). Another characteristic of the Tibetan Plateau is the thermal forcing which is the dominant mechanism for the East Asian monsoon, where the air centers and ascends in summer to create a region of high pressure in the upper atmosphere, resulting in droughts and floods in the East China; conversely, the air descends in winter to increase high pressure over the continental areas, resulting in a cold continental climate in China [*Ye and Gao*, 1979; *Yanai et al.*, 1992; *Wu et al.*, 2007; *Wu et al.*, 2015].

The surface radiation budget is characterized by surface shortwave and longwave radiative fluxes:

$$NR = (1-\alpha)\times DSW + DLW + ULW \qquad \textbf{Equation 1-1}$$

Where α is albedo, and *DSW*, *DLW*, *ULW*, *NR* are the downward shortwave irradiance, downward longwave flux, upward longwave flux and net radiation [*Liang et al.*, 2013b]. The net radiation is the largest term in the surface energy budget, which governs the

hydrological, biogeochemical, ecological processes at the Earth surface [*Liang et al.*, 2010]. The surface energy balance states the ability of the land surface to partition the net radiation into heat fluxes:

$$NR = H + LE + G \qquad \textbf{Equation 1-2}$$

Where H is sensible heat flux, LE latent heat flux, and G ground heat flux. In contrast to the surface radiation and energy budgets (Figure 1-2) that have been quantified using the surface observations, remote sensing, and reanalysis datasets at the global scale, less attention has been paid to analyzing the spatiotemporal characteristics of the land surface radiation and energy budgets at the regional scale due to the limit number of ground observation sites and the lack of comprehensive validation [*Kiehl and Trenberth*, 1997; *Trenberth et al.*, 2009; *Jung et al.*, 2011; *Stephens et al.*, 2012; *Stevens and Schwartz*, 2012; *Wild et al.*, 2014]. Recent studies suggest that the Root Mean Square Errors (RMSEs) of the retrieved latent heat flux (sensible heat flux) of cropland and grassland are within 30–66 Wm^{-2} (23–66 Wm^{-2}) and 35–50 Wm^{-2} (34–50 Wm^{-2}) at the hourly scale, respectively, which decrease to within 17–31 Wm^{-2} (30–46 Wm^{-2}) and 17–29 Wm^{-2} (20–34 Wm^{-2}) at the daily scale, respectively [*Zhang et al.*, 2010; *Mu et al.*, 2011; *Vinukollu et al.*, 2011a; *Yao et al.*, 2011a; *Liu et al.*, 2012b]. It is important to conduct comprehensive validation and comparison before applying global datasets at the regional scale, because the reliability of such datasets is largely dependent on the characteristics of inputs such as the homogeneity of satellite products and the distribution of stations [*Mueller et al.*, 2013].

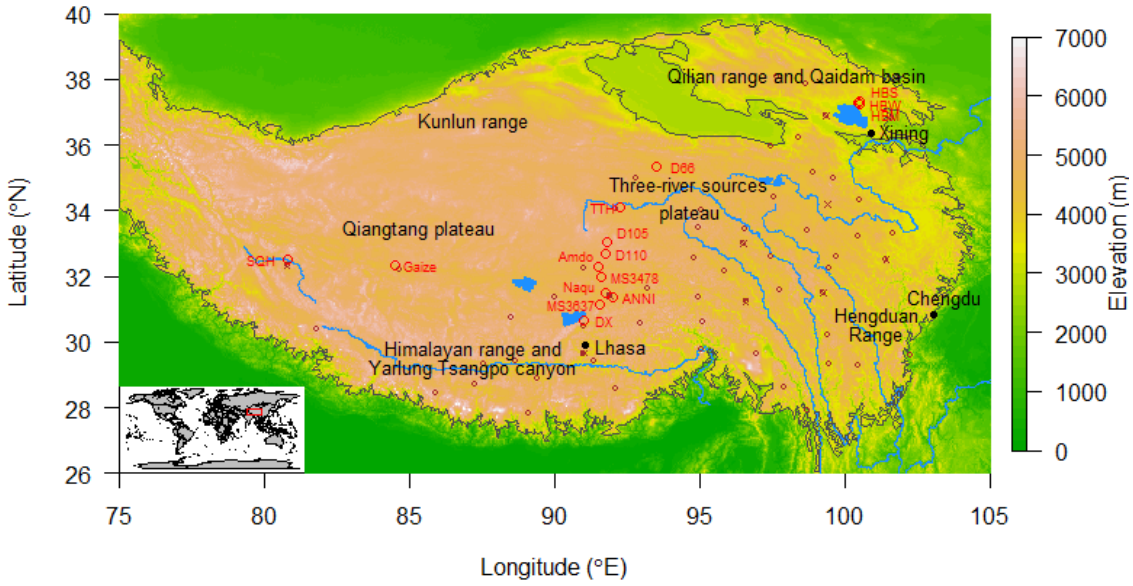

Figure 1-1 Study area (dark grey line) with major lakes, rivers, validation sites (red circle), capitals of provinces in China, and stations for comparison (brown circles are meteorological stations, brown crosses are radiation stations).

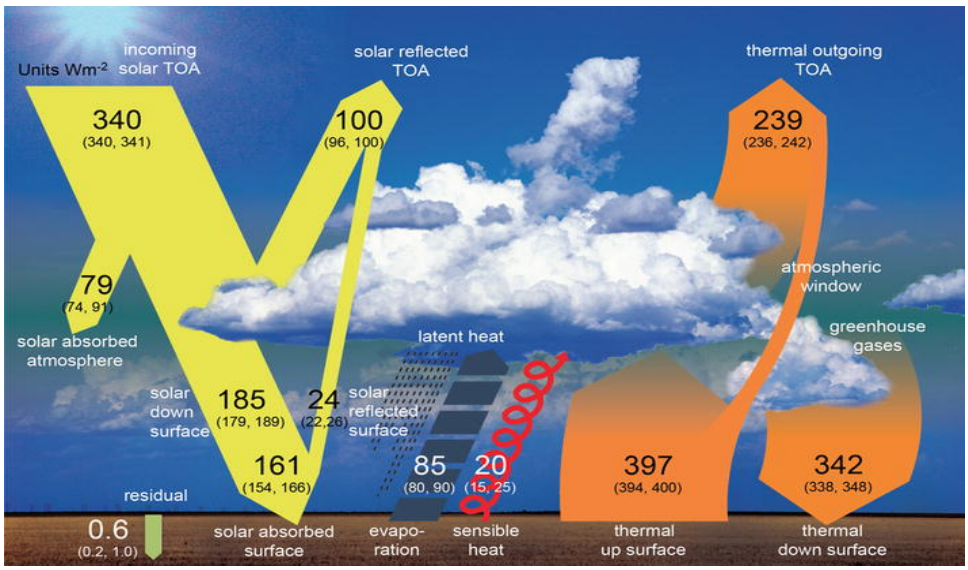

Figure 1-2 Schematic diagram of the annual mean radiation and energy fluxes of the Earth with estimated uncertainty ranges in parentheses from Wild et al., [2013] (units are Wm^{-2}).

To investigate the variability of the land surface energy budget, advanced methods have been developed based on remote sensing data by using radiative transfer model [*Ma et al.*, 2011; *Wonsick and Pinker*, 2014a], and to retrieve surface energy budget from routine meteorological observations [*Yang et al.*, 2009], satellite observations [*Jiménez et al.*, 2009; *Zhang et al.*, 2010], or integrating both sources of data [*Wang and Liang*, 2008; *Jung et al.*, 2009; *Yao et al.*, 2011b]. However, annual and decadal trends of the surface radiation and energy budgets over the Tibetan Plateau derived from reanalysis or remote sensing datasets have been found to be inconsistent with ground measurements in magnitude or direction [*Tang et al.*, 2011; *Wang et al.*, 2012; *Zhu et al.*, 2012]. Moreover, ground observations are inadequate to infer regional pattern of the surface radiation and energy budgets over the entire Tibetan Plateau due to the unbalanced distribution, while the sparse temporal coverage (under the requirement of clear-sky conditions) limits the use of most remote sensing estimations [*Ma et al.*, 2006; *Ma et al.*, 2011] (Table 1-1). The reliability of modeling results is largely limited by not only the error propagations through the retrieval [*Wang and Dickinson*, 2012] but also the uncertainties of the parameterization under complex terrain [*Chen et al.*, 2013].

Table 1-1 Comparison of the surface energy budget from ground observation, remote sensing-based estimation, and reanalysis datasets.

	Ground observation	Remote sensing	Reanalysis
Advantage	• Eddy covariance method offers direct measurement • Independent	• Global coverage • Empirical methods have low accuracy requirement of surface/air temperature	• Global coverage • No missing data • Assimilating satellite and ground observations
Disadvantage	• Missing data • Energy closure issue • Sparse spatial distribution • Limited temporal coverage	• Missing data • Uncertainty of inputs • Uncertainty of empirical method dependent on calibration sites • Clear-sky condition	• Inconsistency • Uncertainty of assimilated inputs • Uncertainty from complex terrain

The surface energy budget over the Tibetan Plateau is of increasing research interest because of its physical link to the Asian Monsoon which sustains about one fourth of the world's population [*Wang et al.*, 2008c; *Immerzeel et al.*, 2010]. At the geological scale, numerical experiments and geologic proxies showed that the formation of the Asian monsoon is related to the uplift of the Tibetan Plateau [*Kutzbach et al.*, 1993; *An et al.*, 2001]. It is since the 1970s that the thermal forcing of the Tibetan Plateau has been related to the formation of the Asian monsoon from the shift of the jet stream, the formation of the South Asia High, the diurnal variation of meteorological observations over the Tibetan Plateau, and the numerical experiments [*Ye and Gao*, 1979; *Yanai and Li*, 1994; *Ye and Wu*, 1998; *Wu et al.*, 2012a]. The mechanism of the thermal forcing of the Tibetan Plateau is essential to the onset of the Asian summer monsoon through the elevated sensible-heating over Tibetan Plateau and radiative cooling in the environment, driving ascends and descends over the Tibetan Plateau and surrounding area, respectively [*He et al.*, 1987; *Yanai and Li*, 1994; *Ye and Wu*, 1998]. Recent study has proposed the concept of "sensible-heat driven air-pump" over the Tibetan Plateau through investigating the effect of the elevated heating over the Tibetan Plateau [*Wu et al.*, 2007]. Modeling result suggests that the surface heating in summer would cause the air column centers and ascends, regulating both the local climate and the North Hemisphere circulation (Figure 1-3) [*Wang et al.*, 2008c]. Furthermore, such processes create the South Asia High in the upper atmosphere in summer, likely contributing to the "droughts in the north and floods in the south" pattern in China [*Duan et al.*, 2013].

It is well known that the interannual variability and long-term trends of the Asian monsoon are also related to variability in the sea surface temperature (SST) of the Pacific

and Atlantic oceans through alteration of the Walker circulation, atmosphere-ocean feedback, and the development of teleconnections [*Goswami et al.*, 2006; *Lu et al.*, 2006; *Wu et al.*, 2009; *Fan et al.*, 2013]. Relationships have been established between the interannual variability of the Asian monsoon and the El Niño Southern Oscillation (ENSO), and the correlation between the two is shown to have weakened for the Indian summer monsoon but strengthened for the East Asian summer monsoon and the western North Pacific summer monsoon since the 1970s [*Kumar et al.*, 1999; *Wang et al.*, 2001; *Wang et al.*, 2008b; *Yim et al.*, 2013]. The strength of the East Asian summer monsoon has also been related to the preceding spring North Atlantic Oscillation (NAO) and the Arctic Oscillation (AO) through the SST anomalies in the North Atlantic and the equatorial Pacific, respectively, which are sustained throughout the following summer [*Wu et al.*, 2009; *Gong et al.*, 2011].

Using numerical simulations, the variability in the Asian summer monsoon has been attributed to anthropogenic aerosols (i.e., black carbon). These cause changes in atmospheric vertical motion, thereby affecting large-scale circulations [*Menon et al.*, 2002; *Ramanathan et al.*, 2005; *Bollasina et al.*, 2011]. The hypothesis of the "elevated heat pump" suggests an association between absorbing aerosols and the enhanced heating of the upper troposphere, which creates a warm-core anticyclone over the Tibetan Plateau in late spring, and results in increased and decreased rainfall in the Indian subcontinent and eastern China, respectively [*Lau and Kim*, 2006; *Lau et al.*, 2006]. However, a recent study has suggested that the anomalous upper troposphere warming and the enhanced Indian rainfall are not observed consistently in high-aerosol years [*Wonsick et al.*, 2014b]. The preceding Tibetan Plateau and Eurasian winter and spring snow conditions

have long been recognized as important factors contributing to the strength of the Asian summer monsoon [*Hahn and Shukla*, 1976; *Zhang et al.*, 2004b]. Recent simulations have suggested that positive feedback from the decreased snow albedo, which is related to depositions of black carbon and dust over the Tibetan Plateau, also influences the Asian monsoon through the spring sensible heat flux over the Tibetan Plateau [*Qian et al.*, 2011]. However, it has not been clarified whether these aerosols are dominant factors causing changes in the Asian summer monsoon, and such a concept is challenged by both the lack of long-term high quality aerosol measurements and the complexity involved in extracting the impact of aerosols from observations [*Ramanathan et al.*, 2001; *Ramanathan et al.*, 2005; *Vinoj et al.*, 2014].

Meteorological observations, reanalysis data, and global circulation modeling are providing prolific evidences that a teleconnection possibly exists between the Tibetan Plateau sensible heat flux and the strength of the Asian summer monsoon. Teleconnection is defined as a linkage between the weather changes occurring in widely separated regions of the world [*Bjerknes*, 1969]. Observational studies have identified correlations between the precipitation over East Asia and the sensible heat anomalies over the central and eastern Tibetan Plateau (using its leading mode or related meteorological variables), and modeling studies have investigated physical processes from the ensemble mean differences of experiments with varied intensities of surface albedo or sensible heat flux over the Tibetan Plateau [*Wang et al.*, 2008c; *Liu et al.*, 2012a; *Duan et al.*, 2013; *Wang et al.*, 2013b]. The proposed physical mechanism linking the Tibetan Plateau sensible heating with the strength of the Asian summer monsoon includes the dominant effect of the sensible heat flux on the local thermally driven

vertical circulation, and the resulting changes in remote circulation patterns (such as subtropical anticyclones and the East Asian southerly through Rossby wave trains), which alter water vapor transport and precipitation over Asia. Furthermore, the suppressed sensible heat flux over the Tibetan Plateau is considered likely to have contributed to droughts and floods in northern and southern China, respectively, through a weakened East Asian summer monsoon circulation in relation to circulations such as the western Pacific subtropical high, the upper-level South Asian High, and the lower-level southwesterly [*Duan et al.*, 2013].

Figure 1-3 Schematic diagram of the potential impact of the sensible heat flux over the Tibetan Plateau on the East Asian monsoon by two Rossby wave trains as demoted by the dashed arrow crossing the cyclone (C) and anticyclone (A) from Wang et al., [2008c].

However, it is unknown to what extent those model-based explanations are valid in nature. Disentangling the relationship between the surface energy budget over the entire Tibetan Plateau and the East Asian summer monsoon has yet been performed, nor have previous studies quantified the physical evidence through which the East Asian monsoon has been regulated by the sensible heating over the Tibetan Plateau by using

integrated multi-source information, including both observational and reanalysis datasets. Therefore, this dissertation will address the following questions: 1) what are the spatiotemporal characteristics of the surface radiation and energy budgets over the Tibetan Plateau in recent decades? 2) How does the interannual variation of the surface radiation and energy budgets correlate to, respond to, and impact the observed surface and atmospheric anomalies over the Tibetan Plateau? And 3) can the changes of the surface energy budget components over the Tibetan Plateau explain the weakening of the East Asian summer monsoon and associated precipitation changes in China (drought in the north and flood in the south)?

1.2 Objectives

The overall objective of this study is to quantify the relationship between the surface energy budget over the Tibetan Plateau and the East Asian summer monsoon by synthesizing ground observations, remote sensing, and reanalysis datasets. Specifically,

1) Developing a monthly surface radiation and energy budgets dataset by 0.5° over the Tibetan Plateau, integrating ground and satellite observations and reanalysis datasets.

2) Quantifying the spatial distribution and temporal variability of the surface radiation and energy budgets over the Tibetan Plateau based on the fused data, and assessing its correlations with the observed surface and atmospheric conditions over the Tibetan Plateau.

3) Testing the hypothesis of whether the Asian summer monsoon rainfall is under the impact of the spring sensible heat flux over the Tibetan Plateau by using the fused surface energy budget.

1.3 Outline of the dissertation

Chapter 2 estimates the monthly surface radiation budget over the Tibetan Plateau from ground-measurement, reanalysis, and remote sensing datasets by applying multiple linear regression data fusion method. Site validations of reanalysis and remote sensing datasets are given, results from leave-one-site-out cross-validation are summarized, and comparison with long-term in situ observation of downward shortwave irradiance is made. The climatology and interannual variability of downward shortwave irradiance, albedo, downward and upward longwave flux, and net radiation from the fused data are presented and analyzed in conjunction with atmospheric and surface conditions over the Tibetan Plateau.

Chapter 3 generates the monthly fused surface energy budget over the Tibetan Plateau from ground-measurement, reanalysis, and remote sensing datasets. Net radiation from the fused surface radiation budget in Chapter 2 is used as input, multiple linear regression data fusion method is applied to fuse the latent heat flux and ground heat flux, and the sensible heat flux is estimated based the surface energy balance. Validations of reanalysis and remote sensing datasets at stations are performed, cross-validation results of the fused surface energy budget are given, and comparison with estimations of sensible and latent heat flux over meteorological sites is made. The seasonal and annual mean and standard deviation of sensible and latent heat flux from the fused data are shown, and the

anomalies are correlated with atmospheric and surface conditions as well as the surface radiation budget components over the Tibetan Plateau.

Chapter 4 assesses the impact of the spring Tibetan Plateau sensible heat flux on the Asian summer monsoon rainfall, based on the sensible heat flux over the Tibetan Plateau from the fused surface energy budget in Chapter 3, precipitation and SST from observations, and wind and water vapor transport from reanalysis. Variability of the March, April, and May sensible heat flux over the Tibetan Plateau is presented and its correlation with atmospheric and surface variables as well as surface radiation budget components are analyzed. Based on regression analysis and the Granger causality test, the spatial pattern of the relationship between the late spring sensible heat flux over the Tibetan Plateau and the Asian summer monsoon rainfall is analyzes, and its supporting physical mechanisms are inferred from the composite analysis of the monsoon circulations.

Chapter 5 concludes the main findings and contributions of this dissertation. Future study directions are also discussed based on the results and limitations of current work.

Chapter 2 Characterizing the Surface Radiation Budget over the Tibetan Plateau

The surface radiation budget over the Tibetan Plateau, often referred to as the "third pole" of the Earth, is of great importance in the study of significant climate change over recent decades [*Qiu,* 2008]. Climatic changes over the Tibetan Plateau include surface warming [*Qin et al.*, 2009], solar dimming [*Yang et al.*, 2012], moistening, wind stilling [*Yang et al.*, 2011c], and variations in snow cover [*Pu and Xu*, 2009; *Gao et al.*, 2012]. Such changes have invited crucial questions, such as how atmospheric variations and surface changes impact the surface radiation budget over the Tibetan Plateau, how the decadal dimming and brightening affect the environment and climate [*Wild*, 2012], and how the surface radiation budget over the Tibetan Plateau responds to rapid warming [*Qin et al.*, 2009]. However, few studies have attempted spatiotemporal characterization of surface radiation budgets over the entire Tibetan Plateau in recent decades, for several reasons: limited sites for ground measurement, poor accuracy of remote sensing products, and large errors of reanalysis data sets.

This chapter first develops a data fusion method for the characterization of the monthly surface radiation budget over the Tibetan Plateau by integrating ground measurements, reanalysis data, and remote sensing data. The annual and seasonal spatial pattern and temporal variation in the fused surface radiation budget over the Tibetan Plateau were then analyzed. The following sections describe the three data sources and methodologies (section 3.1 and section 2.2), present results and discussions (section 2.3), and summarize conclusions (section 2.4). Two paper-series about the work in this chapter have been published [*Shi and Liang,* 2013a; b].

2.1 Datasets

Three data sources are utilized in this study: 1) ground measurement data from four major measurement networks and experiments, including AsiaFlux, ChinaFLUX, GAME/Tibet, and CAMP/Tibet; 2) two long-term remote sensing products, namely the Global Energy and Water Cycle Experiment Surface Radiation Budget (GEWEX-SRB) and the International Satellite Cloud Climatology Project ISCCP-FD dataset; and 3) four state-of-the-art reanalysis products, including the Climate Forecast System Reanalysis (CFSR), the Modern-Era Retrospective Analysis for Research and Applications (MERRA), the ERA-Interim reanalysis, and the Japanese 25-year Reanalysis (JRA-25). These products were selected owing to their complete coverage of the temporal period from 1984 to 2007 for which both remote sensing data and ground measurements are available. The spatiotemporal characteristics of the three source datasets are summarized in Table 2-1**,** and described in detail in sections 2.1.1–2.1.3.

2.1.1 Ground-measured datasets

Ground observations of the surface radiation fluxes over the Tibetan Plateau were sourced from three projects/networks: the Coordinated Energy and Water Cycle Observation Project (CEOP) [*Koike*, 2004], the Asian Automatic Weather Station Network (AAN), and FLUXNET [*Baldocchi et al.*, 2001]. FLUXNET is a global network of micrometeorological towers at more than 500 sites in 30 regional networks. To ensure that the reliable existing (1997–2007) ground measurements of surface radiative fluxes were used, 23 observation sites were selected from AsiaFlux [*Kim et al.*, 2009], ChinaFLUX [*Yu et al.*, 2006], the GEWEX Asian Monsoon Experiment on the Tibetan

Plateau (GAME/Tibet), and the CEOP Asia–Australia Monsoon Project on the Tibetan Plateau (CAMP/Tibet) (Table 2-1).

Ground measurement sites were all located above 3000 m and were not used in the estimation from remote sensing and reanalysis products, which applied high-quality instruments of the surface radiation fluxes. Specifically, EKO S-100 pyranometer has an estimated accuracy by ±5% at the daily scale; LiCor Li-200SA and VAISALA CM6B (compliant with ISO 9060 first class specification) are pyranometers has an uncertainty by 5% of the daily total at 95% confidence level. The other pyranometers (compliant with ISO 9060 secondary standard specification), including Kipp & Zonen CM11, Kipp & Zonen CM21, Kipp & Zonen CM3, Kipp & Zonen PCM-01, EKO MS-601, EKO MS-801, and EKO MS-802 has an uncertainty by 2% of the daily total at 95% confidence level. Although they are not categorized by a general standard classification system similar to that for pyranometers [*WMO*, 1981], pygeometers can be divided into two groups according to their approximate accuracy at the daily scale: Kipp & Zonen CG3 with factory-estimated accuracy of ±10% of the daily total, and Eppley PIR, EKO MS-201, and EKO MS-202 with accuracy of ±5% [*Fairall et al.*, 1998; *Wang et al.*, 2005].

AsiaFlux and ChinaFLUX are part of a regional scientific branch of FLUXNET that focuses on the regional carbon and hydrological cycles and energy exchange between terrestrial ecosystems and the atmosphere. One of the AsiaFlux sites is located in alpine meadow grassland at Haibei (HBM), China, and offers 15-min four radiation fluxes [*Gu et al.*, 2003; *Gu et al.*, 2005]. Quality control is in the form of an absolute threshold that removes unreliable data [*Vickers and Mahrt*, 1997]. ChinaFLUX provides long-term measurement of the exchange of energy between terrestrial ecosystems and the

atmosphere in China. The radiation fluxes from three sites with routine meteorological measurement systems in the ChinaFLUX network were selected for this study; here, shortwave and longwave fluxes were measured at 30-min intervals from 2003 to 2007 at the Damxung (DX) and Haibei Wetland (HBW) sites and from November 2002 to 2007 at the Haibei Shrubland site (HBS).

GAME/Tibet is an international field experiment over the Tibetan Plateau that was supported by the World Climate Research Programme (WCRP)/GEWEX Asian Monsoon Experiment. The dataset includes the prephased observation period in 1997 and the intensive observation period in 1998, and has been proven to be the most reliable radiation flux dataset for elevated regions globally [*Yang et al.*, 2008b]. The observation network includes various components: 1) six automated weather stations at the D66, Tuotuohe (TTH), D110, MS3637, Shiquanhe (SQH), and Gaize sites; 2) two portable automated mesonets at the MS3478 and MS3637; 3) planetary boundary layer tower measurements of radiation fluxes at the Amdo site, and 4) turbulent flux measurements at the Naqu flux site (BJ).

The CAMP/Tibet surface radiation dataset contains the enhanced observing period 3 and 4 of CEOP from October 2002 through December 31 2004. It consists of 12 stations covering an area of 150 km^2 (91°E –92.5°E, 30.7°N–33.3°N) in the center of the Tibetan Plateau; 9 of these stations provide radiation flux measurements. Most CAMP/Tibet sites correspond to GAME/Tibet, although different instruments are used. Therefore, sites with continuous observations from multiple datasets were extracted separately and combined before analysis. The original measured fluxes were first sampled every second and averaged for each minute before being visually examined for

extreme (low, high) or constant values using the CAMP Quality Control Web Interface. The objective of this study was to generate the best estimate of the monthly surface radiation budget; thus, only CAMP/Tibet data with sufficient quality (i.e., quality flagged as good or interpolated) were used in validation.

Additional radiation observation sites with decadal daily radiation measurements are provided by the National Meteorological Information Center, China Meteorological Administration (NMIC/CMA). Measurement of downward shortwave irradiance was initiated in 1957, and most stations within the study area started obtaining the downward shortwave irradiance measurements after 1960. Measurements of downward shortwave irradiance were conducted using instruments identical to those used by the former Soviet Union (e.g., Yanishevsky thermoelectric pyranometer) and instruments manufactured in China (e.g., DFY-4 pyranometers) before and after early 1990s, respectively [*CMA*, 1996]. In this study, the monthly mean downward shortwave irradiance was obtained from 9 stations (Geer, Naqu, Lhasa, Yushu, Changdu, Gangcha, Guoluo, Ganzi, and Hongyuan); the spatial distribution of these sites is illustrated in Figure 1-1. Recent studies argued that the changes of the instrument were unlikely to cause inconsistent measurements over CMA radiation sites, because both instruments have similar estimated accuracy (5%) [*Shi et al.*, 2008; *Tang et al.*, 2011; *You et al.*, 2012]. To ensure the reliability of downward shortwave irradiance from CMA radiation sites, suspected or inhomogeneous data were identified and excluded before 1994 in previous studies [*Tang et al.*, 2011; *You et al.*, 2012]. Based on the fact that inhomogeneity was found to exist in the early 1990s for four sites (Geer, Naqu, Lhasa, Yushu), and the other four sites only

commenced measurement in the early 1990s, the study period for the downward shortwave irradiance comparison was set to 1994–2007.

2.1.2 Remote sensing datasets

The latest GEWEX-SRB product (versions 3.0 and 3.1 for shortwave and longwave radiation, respectively) is provided by the National Aeronautics and Space Administration (NASA) Langley Research Center to support study of the earth's radiation budget in global and regional climate change [*Stackhouse et al.,* 2011]. GEWEX-SRB aims to offer global surface and atmospheric shortwave and longwave fluxes at 1° to analyze climate variation and decadal trends from July 1983 to December 2007. The shortwave and longwave fluxes are estimated using the Pinker/Laszlo shortwave algorithm [*Pinker and Ewing,* 1985; *Pinker and Laszlo,* 1992] and the thermal infrared radiative transfer code of Fu et al., [1997], respectively. Both of these algorithms require primary inputs of visible and infrared radiance, cloud and surface properties from ISCCP pixel-level data, temperature and moisture from the GEOS-4 reanalysis product from NASA Global Modeling and Assimilation Office, and column ozone from the Total Ozone Mapping Spectrometer, the TIROS Operational Vertical Sounder archives, and Stratospheric Monitoring Group's Ozone Blended Analysis.

ISCCP-FD is offered by NASA Goddard Institute for Space Studies at a spatial resolution of 2.5° for the period from July 1983 to December 2009. The longwave and shortwave fluxes were derived based on a radiative transfer model [*Zhang et al.,* 1995; *Zhang et al.,* 2004a] with input parameters primarily from cloud and surface properties of the ISCCP-D1 dataset, temperature and humidity from TIROS Operational Vertical

Sounder archives, and ozone from the Total Ozone Mapping Spectrometer. Recent evaluation of the albedo of ISCCP-FD and GEWEX-SRB based on the calibrated Moderate Resolution Imaging Spectroradiometer (MODIS) albedo product over the Tibetan Plateau indicated that both datasets underestimate the albedo in the central and western Tibetan Plateau [*Qin et al.*, 2011]; moreover, these two products were found to underestimate the downward shortwave irradiance but overestimate the downward longwave radiation over the Tibetan Plateau [*Yang et al.*, 2008b; *Gui et al.*, 2010].

2.1.3 Reanalysis datasets

CFSR is the latest global reanalysis data from the National Centers for Environmental Prediction (NCEP) from 1979 to the present day [*Saha et al.*, 2010]. CFSR couples atmosphere and ocean models for six-hourly runs and assimilates satellite radiance for a global atmosphere resolution of T382 (about 0.3°) with 64 levels. Compared to previous NCEP reanalysis datasets, CFSR has been proven to improve the representation of freshwater flux, precipitation distribution and monthly trends at global scales [*Ebisuzaki and Zhang*, 2011; *Wang et al.*, 2011b]. Comparison of CFSR and other reanalysis data has demonstrated that CFSR exhibits the best overall performance over the Tibetan Plateau [*Wang and Zeng*, 2012].

MERRA is a new reanalysis dataset provided by NASA Global Modeling and Assimilation Office for the satellite era from 1979 until the present day. MERRA was designed to integrate with NASA's Earth Observing System satellite data (which are more accurate for precipitation and water vapor climatology) for use in climate analysis [*Rienecker et al.*, 2011]. This study used the hourly two-dimensional diagnostics of

surface fluxes at full spatial resolution (0.5° latitude × 0.67° longitude). MERRA has been applied to test decadal trends of solar dimming in Asia [*Kambezidis et al.*, 2012], and exhibits a high correlation with the observations from the CMA stations over the Tibetan Plateau [*Wang and Zeng*, 2012].

ERA-Interim is another new reanalysis dataset produced by the European Centre for Medium-Range Weather Forecasts (ECMWF). It was developed to replace an older successful reanalysis dataset, ERA-40 [*Uppala et al.*, 2005], with improved atmospheric models and four-dimensional variational assimilation at a horizontal resolution of T255 (about 0.70°) at 60 model levels since 1979 [*Dee et al.*, 2011]. ERA-Interim improved the global land surface energy balance (to 0.5 Wm^{-2} from 1.3 Wm^{-2} for ERA-40) by improving global observation systems. A recent study found that ERA-Interim performed well in prediction of daily temperature over China [*Mao et al.*, 2010].

JRA-25 is the first long-term reanalysis undertaken in Asia using the Japan Meteorological Agency numerical assimilation and forecast system from 1979 to 2011[*Onogi et al.*, 2007]. The purpose of JRA-25 was to provide high-quality data for the Asian region; it is a coproduction of the Japan Meteorological Agency and the Central Research Institute of Electric Power Industry (JMA/CRIEPI). The global model has a spatial resolution of T106 (about 0.125°) in 40 vertical layers. It assimilates remote sensing datasets such as atmospheric motion vector wind from geostationary satellites, brightness temperature from TOVS, and perceptible water retrieved from the Special Sensor Microwave Imager using a three-dimensional variation method. JRA-25 has been demonstrated to exhibit good performance in analysis of global precipitation and snow depth.

Table 2-1 Summary of data sources (*, dataset for comparison) of the surface radiation and energy budgets with organization, spatial resolution, temporal resolution, and temporal coverage, sourced from NCEP, NASA, ECMWF, JMA/CRIEPI, National Center for Atmospheric Research (NCAR), WCRP, University of Bristol (UB), Princeton University (PU), FLUXNET, AAN, CEOP, NMIC/CMA, and the Institute of Tibetan Plateau Research, Chinese Academy of Sciences (ITPR CAS).

Name	Organization	Spatial resolution	Spatial resolution in this study	Temporal resolution	Temporal coverage	Temporal period in this study
			Reanalysis datasets			
CFSR	NCEP	T382 (38km)	0.5°×0.5°	6 hourly	01/1979–12/2009	01/1984–12/2007
MERRA	NASA	0.50°×0.67°	0.5°×0.5°	hourly	01/1979–12/2014	01/1984–12/2007
ERA-Interim	ECMWF	T255 (80km)	0.5°×0.5°	3 hourly	01/1979–12/2014	01/1984–12/2007
JRA-25	JMA/CRIEPI	T106 (110km)	0.5°×0.5°	3 hourly	01/1979–12/2011	01/1984–12/2007
NRA-1*	NCEP/NCAR	T62 (200km)	0.5°×0.5°	6 hourly	01/1948–12/2014	01/1984–12/2007
NRA-2*	NCEP	T62 (200km)	0.5°×0.5°	6 hourly	01/1979–12/2014	01/1984–12/2007
GLDAS-1-CLM *	NASA	1.00°×1.00°	0.5°×0.5°	3 hourly	01/1979–11/2014	01/1984–12/2007
GLDAS-1-MOS*	NASA	1.00°×1.00°	0.5°×0.5°	3 hourly	01/1979–11/2014	01/1984–12/2007
GLDAS-1-NOAH*	NASA	1.00°×1.00°	0.5°×0.5°	3 hourly	01/1979–11/2014	01/1984–12/2007
GLDAS-2-NOAH*	NASA	0.25°×0.25°	0.5°×0.5°	3 hourly	01/1948–12/2010	01/1984–12/2007
			Remote sensing datasets			
GEWEX-SRB	NASA	1.00°×1.00°	0.5°×0.5°	3 hourly	07/1983–12/2007	01/1984–12/2007
ISCCP-FD	WCRP	2.50°×2.50°	0.5°×0.5°	3 hourly	07/1983–12/ 2009	01/1984–12/2007
Zhang10	NASA	8km	0.5°×0.5°	monthly	01/1983–12/2006	01/1984–12/2006
GLEAM-LE	UB	0.25°	0.5°×0.5°	daily	01/1984–12/2007	01/1984–12/2007
PU-LE*	PU	0.50°	0.5°×0.5°	3 hourly	01/1984–12/2007	01/1984–12/2007
CERES SYN*	NASA	1.00°×1.00°	0.5°×0.5°	3 hourly	03/2000–07/2014	03/2000–12/2007
			Ground-measured datasets			
AsiaFlux	FLUXNET	1 stations	-	15 min	07/ 2002–12/2004	07/ 2002–12/2004
ChinaFLUX	FLUXNET	3 station	-	30 min	11/2002–12/2007	11/2002–12/2007
GAME/Tibet	AAN	10 stations	-	30 min	12/1994–04/2005	01/1997–04/2005
CAMP/Tibet	CEOP	9 stations	-	hourly	10/2002–12/2004	10/2002–12/2004
CMA radiation sites*	NMIC/CMA	9 stations	-	daily	01/1959–12/2010	01/1994–12/2007
Yang09, Yang11*	ITPR CAS	85 stations	-	daily	01/1984–12/2006	01/1984–12/2006

Table 2-2 Summary of the in situ sites with the downward and upward shortwave radiation (DSW and USW) and longwave radiation (DLW and ULW) measurement over the Tibetan Plateau.

Name	Lat (°N)	Lon (°S)	Ele (m)	Height	Instruments of Shortwave Radiation	Instruments of Longwave Radiation	Data Period	Date Length of DSW, USW, DLW, ULW
					AsiaFlux			
HBM	37.61	101.31	3250	1.5 m	Kipp & Zonen CM3	Kipp & Zonen CG3	Jul 2002–Dec 2004	1017, 854, 728, 937
					CAMP/Tibet			
Amdo	32.24	91.62	4695	1.58 m, 1.28 m	Kipp & Zonen CM21	Eppley PIR	Oct 2002–Dec 2004	424, 350, 424, 368
ANNI	31.25	92.17	4480	1.58 m, 1.28 m	Kipp & Zonen CM21	Eppley PIR	Oct 2002–Dec 2004	681, 588, -, 587
D105	33.06	91.94	5038	1.58 m, 1.28 m	Kipp & Zonen CM21	Eppley PIR	Oct 2002–Dec 2004	765, 503, 73, 5690
MS3478	31.92	91.71	4619	1.58 m, 1.28 m	Kipp & Zonen CM21	Eppley PIR	Oct 2002–Dec 2004	820, 811, 820, -
BJ	31.37	91.9	4509	1.58 m, 1.28 m	Kipp & Zonen CM21	Eppley PIR	Oct 2002–Dec 2004	654, 552, 654, 573
D110	32.69	91.87	4984	2.45 m, 2.43 m	Kipp & Zonen PCM-01	-	Oct 2002–Dec 2004	363, -, -, -
D66	35.52	93.78	4585	6 m	EKO MS-601	-	Oct 2002–Dec 2004	820, -, -, -
Gaize	32.3	84.05	4416	1.67 m, 1.30 m	EKO MS-802	EKO MS-202	Oct 2002–Dec 2004	820, 692, 817, 644
					ChinaFLUX			
DX	30.5	91.07	4751	1.2 m	Kipp & Zonen CM3	Kipp & Zonen CG3	Jun 2003–Dec 2007	1565, 1490, 1587, 1559
HBS	37.67	101.33	3400	1.2 m	Kipp & Zonen CM3	Kipp & Zonen CG3	Dec 2002–Dec 2007	1725, 1537, 1726, 1701
HBW	37.61	101.32	3400	1.2 m	Kipp & Zonen CM3	Kipp & Zonen CG3	Sep 2003–Dec 2007	1431, 1142, -, 1383
					GAME/Tibet			
Amdo	32.24	91.63	4700	1.5 m	EKO MS-801	Eppley PIR	Jan 1998–May 2003	1555, 1441, 1590, 1219
D110	32.69	91.88	5070	6 m	EKO S-100	-	Jan 1998–Sep 1998	126, -, -, -
D66	35.52	93.78	4600	6 m	EKO S-100	-	Jan 1998–Jul 2004	364, -, -, -
MS3478	31.93	91.72	5063	1.5 m	Kipp & Zonen CM11	Eppley PIR	May 1998–Sep 1998	114, 40, 118, 188
MS3637	31.02	91.66	4820	1.5 m	Licor LI-200SA	Eppley PIR	Jul 1998–Sep 1998	70, 57, -, -
TTH	34.22	92.44	4535	6 m	EKO S-100	-	Jan 1998–May 2003	424, -, -, -
Gaize	32.3	84.05	4420	1.5 m	EKO MS-801	EKO MS-201	May 1998–Sep 1998	148, 132, -, -
BJ	31.37	91.9	4580	1.5 m	Kipp & Zonen CM3	Kipp & Zonen CG3	May 1998–Sep 1998	102, 104, 103, 79
SQH	32.5	80.08	4279	1.5 m	EKO MS-801	EKO MS-201	May 1998–Sep 1998	135, 136, -, -

2.2 Methodologies

The methods for characterizing the surface radiation budget over the Tibetan Plateau are shown in Figure 2-1. The input datasets were processed to extract monthly mean values; this was followed by the data fusion to overcome the limitations of existing products. The performance of the fused data were compared to that using individual calibrated data sets. Next, the fused data were used to quantify the relationship to the selected surface or atmospheric variables.

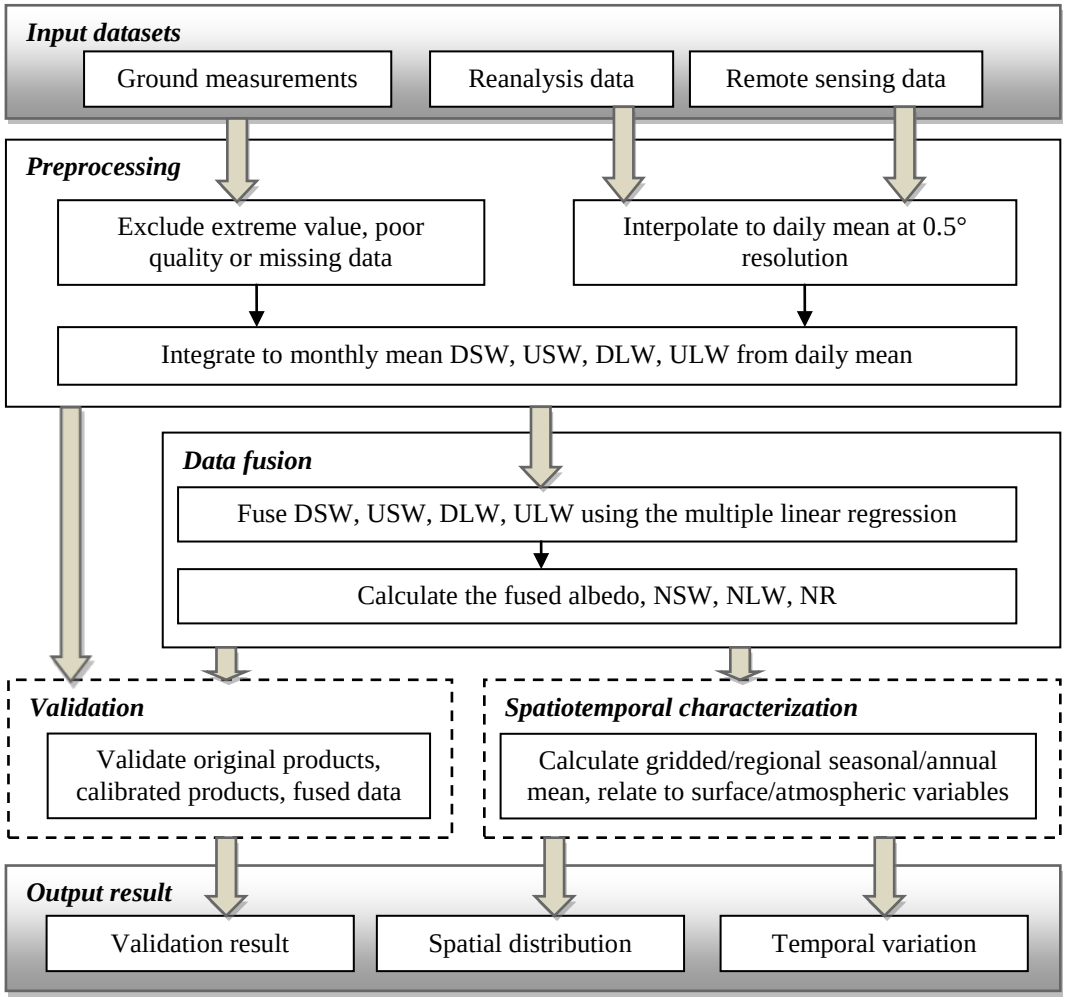

Figure 2-1 Flowchart of the methods for characterizing the surface radiation budget over the Tibetan Plateau. DSW and USW are downward and upward shortwave radiation, DLW and ULW are downward and upward longwave radiation, and NSW, NLW, and NR are net shortwave, longwave, and all-wave radiation.

2.2.1 Preprocessing

Data preprocessing was conducted to interpolate the original ground-measured, reanalysis, and remote sensing data to monthly mean values for each site or each grid at 0.5° spatial resolution. For 23 sites from ground measurement networks, daily measurements were extracted and integrated to daily hourly means under criteria that excluded extreme low or high values and poor quality or missing data. Specifically, the extreme low or high values were eliminated by use of threshold intervals (0–1500 Wm^{-2} for the downward shortwave irradiance, 0–300 Wm^{-2} for the upward shortwave radiation, 100–500 Wm^{-2} for the downward longwave radiation, and 200–600 Wm^{-2} for the upward longwave radiation). Then, daily averaged values were calculated from daily hourly mean values with less than half missing, and the monthly mean values were calculated from daily mean value in instances where valid daily averaged value were found for more than 15 days in a given month. Meanwhile, the value of surface radiative fluxes from the reanalysis and remote sensing datasets were first extracted in their original projection and temporal resolution and then temporally interpolated to daily means by calculating the mean value of each product. The six gridded datasets were then interpolated to 0.5° resolution by extracting data from the nearest original grid or from the mean value of the nearest original grids covered by the newly projected grid (for product with resolution lower than 0.5°). Finally, monthly surface radiative fluxes were generated from the daily mean values from the reanalysis and remote sensing datasets.

2.2.2 Data fusion

The monthly surface radiation budgets from four reanalysis datasets and two remote sensing datasets were integrated with ground-measured data by using the multiple linear regression method:

$$Y = \beta_0 + \sum_{i=1}^{p} \beta_i X_i + \varepsilon, \varepsilon \sim N(0, \sigma^2),\ p > 1 \qquad \textbf{Equation 2-1}$$

where Y is the ground-measured data, β_0 the intercept, p the number of the original datasets that are used in the multiple linear regression, β_i the coefficient for dataset I, X_i the estimation from dataset I, ε the residual following the assumption of normal distribution ($N(0, \sigma^2)$). The intercept and coefficient are estimated to minimize the sum of the square residuals.

This study first applied multiple linear regression to the downward and upward shortwave fluxes, and the downward and upward longwave radiation fluxes, and then generated albedo from the ratio of the upward shortwave flux to the downward shortwave irradiance and the net radiation using Equation 1-1. The multiple linear regression in this study was conducted in the environment of R [2012]. The downward and upward longwave radiation fluxes from ISCCP-FD were excluded from the calculation of fused longwave fluxes, because the absolute bias error of most months exceeded 20 Wm^{-2}. Those biases are related to large errors of input hydrological parameters of ISCCP-FD [*Gui et al.*, 2010]. In addition, CFSR is not included in the upward shortwave and longwave radiation fusion, because significant biases occurred from 1995 to 1999 and in 2007. The RMSE, the mean bias error (MBE), and the coefficient of determination after

deseasonalization (D_R^2) were used to quantify accuracy of each input products. To validate the fused surface radiation budget, the cross validation was conducted by removing a site, applying the fusion model in the remaining sites, and validating with the unused site. The RMSE from the exclude-one-site-out cross validation (RMSE_CV) was the average RMSE achieved by applying this process multiple times, omitting one site for validation each time.

In the case of high-level data fusion for the surface energy budget, such as feature-level image fusion according to Pohl and Van Genderen [*Pohl and Van Genderen*, 1998]), the multiple linear regression data fused method constrains the error of the fused surface energy budget through minimization of the residue error. To quantify the potential uncertainty from the selection of the data fusion method, experiments were conducted in which the same inputs were used for different linear regression models, including stepwise regression, which selects datasets by excluding those from the starting model to minimize the Bayesian information criterion (BIC); principle analysis regression (PCA), which inherits from the multiple linear regression but uses the first two or three principle components of input datasets (PCA_2 and PCA_3); and adapted lasso regression, which improves the lasso regularization technique in the selection of datasets to simultaneously estimate and select variables with adaptive weights [*Zou*, 2006]. Advanced statistical methods with the potential for revealing unseen (i.e., nonlinear) processes by linear approximations were selected for comparison with the MLR results, including Supported Vector Regression (SVM) [*Vapnik*, 1999] and Random Forest (RF) regression [*Breiman*, 2001]. SVM computes optimized hyperplanes that maximize the deviations from the targets, and RF realizes the concept of ensemble learning from the

group of regression trees through processes of boosting and bagging. An additional commonly used method, particularly in multi-model fusion, is Bayesian model averaging (BMA), which was implemented to optimize weights to integrate predictive distributions from multi-models such as the mapping of longwave radiative fluxes from multiple models [*Raftery et al.*, 2005; *Wu et al.*, 2012b].

2.2.3 Spatiotemporal characterizations

The spatial pattern of the mean value and STD of the surface radiation budget over the Tibetan Plateau were calculated for annual and four seasons. The four seasons were defined as spring (March –April –May), summer (June –July –August), autumn (September –October –November), and winter (December–January–February). The uncertainty of the annual and seasonal mean and STD of the fused data was assessed by applying the Monte Carlo method with 1000 ensembles. Ensembles were generated following the distribution with mean value as the predicted value and standard deviation calculated from the 95% prediction interval by using R.

The surface radiation budget anomalies over the Tibetan Plateau was compared to selected variables of atmospheric and surface conditions, and the relationship of two variables was quantified using the Pearson correlation coefficient. The selected variables included cloud cover and temperature (monthly mean of daily mean temperature and temperature range) from the Climate Research Unit (CRU) TS3.1[*Harris et al.*, 2014], Rutgers snow cover data [*Robinson et al.*, 1993], the Global Inventory Modeling and Mapping Studies (GIMMS) normalized difference vegetation index (NDVI) derived from the Advanced Very High Resolution Radiometer (AVHRR) [*Tucker et al.*, 2005], and

MERRA water vapor (Table 2-3). A recent validation using radiosonde observations over China suggests that MERRA water vapor outperforms other reanalysis datasets [*Jiang and Liang*, 2013].

Table 2-3 Data sources for surface and atmospheric conditions over the TP, sourced from four organizations (UMD GLCF, University of Maryland, the Global Land Cover Facility; NASA; UAE, University of East Anglia; NOAA, the National Oceanic and Atmospheric Administration).

Name	Organization	Spatial resolution	Temporal resolution	Temporal coverage
GIMMS NDVI	UMD GLCF	8 km	Bi-monthly	07/1981–12/2012
MERRA water vapor	NASA	0.50°×0.67°	Hourly	01/1979–12/2014
CRU TS3.1 temperature and cloud cover	UAE	0.50°×0.50°	Monthly	01/1901–12/2009
Rutgers snow cover	NOAA	100 km	Weekly	11/1966–04/2014 2010

2.3 Results and discussions

2.3.1 Validation results

The total number of the monthly ground measured data used for validation is shown in Table 2-4. The validation results for six reanalysis/remote sensing data products suggests that reanalysis products overestimate the downward shortwave irradiance and albedo, while remote sensing products underestimate the downward shortwave irradiance but overestimate the downward longwave radiation (Table 2-5). CFSR exhibits the lowest RMSEs of all six products for longwave fluxes but the largest RMSE for the albedo. MERRA displays significant positive bias for downward shortwave irradiance by 32.1 Wm^{-2} and the lowest RMSE for albedo (0.04) of all products. GEWEX-SRB has the lowest RMSE for the downward shortwave irradiance and the net shortwave radiation of all six products (by 18.3 Wm^{-2} and 19.7 Wm^{-2}, respectively). ISCCP-FD exhibits the

lowest RMSE for the upward shortwave radiation (11.6 Wm^{-2}), but its RMSEs for longwave fluxes are the largest.

Table 2-6 reports the coefficients of the four radiative fluxes used to generate the fused data over the Tibetan Plateau. The coefficients were determined by the multiple linear regression method based on eleven years (1997–2007) of ground measurements. In general, the largest absolute coefficient exists for the product with highest R^2 for each shortwave or longwave flux, and products with weaker correlation with ground measurements are assigned coefficients smaller than 0.1. CFSR and ERA-Interim contribute most to fused downward longwave radiation; MERRA dominates the upward shortwave and longwave radiation; and GEWEX-SRB exhibits the highest coefficient for downward shortwave radiation.

Table 2-4 Number of available ground measurement of surface energy budget in each month.

	Jan	Feb	Mar	Apr	May	Jun	Jul	Aug	Sep	Oct	Nov	Dec
Downward shortwave irradiance	34	32	33	34	39	39	39	40	38	40	42	43
Upward shortwave radiation	22	24	25	26	29	33	34	34	29	28	35	35
Albedo	22	24	25	26	29	33	34	34	29	28	35	35
Net shortwave radiation	22	24	25	26	29	33	34	34	29	28	35	35
Downward longwave radiation	23	23	23	24	26	25	25	25	25	28	30	30
Upward longwave radiation	19	24	26	25	26	27	30	30	25	30	32	31
Net longwave radiation	15	20	21	20	21	20	23	23	22	25	27	26
Net Radiation	13	19	21	16	17	19	22	22	21	20	27	26

Table 2-5 Validation results of the surface radiation budget of reanalysis and remote sensing datasets.

	Validation statistics	CFSR	MERRA	ERA-Interim	JRA-25	GEWEX-SRB	ISCCP-FD
Downward shortwave irradiance	RMSE (Wm^{-2})	34.8	42.8	29.3	37.0	18.3	19.3
	MBE (Wm^{-2})	22.3	32.1	14.1	29.2	-8.8	-8.0
	D_R^2	0.43	0.47	0.42	0.47	0.60	0.54
Upward shortwave radiation	RMSE (Wm^{-2})	38.3	11.1	31.0	25.9	11.7	11.6
	MBE (Wm^{-2})	32.2	6.3	21.7	19.6	-5.2	1.9
	D_R^2	0.15	0.37	0.00	0.02	0.13	0.11
Downward longwave radiation	RMSE (Wm^{-2})	14.7	31.0	19.7	23.5	16.7	30.4
	MBE (Wm^{-2})	-10.0	-28.6	-14.5	-20.2	7.5	15.9
	D_R^2	0.33	0.35	0.18	0.40	0.24	0.12
Upward longwave radiation	RMSE (Wm^{-2})	14.8	18.6	17.6	23.0	17.0	24.2
	MBE (Wm^{-2})	-7.0	-16.6	-12.9	-5.1	6.0	-0.4
	D_R^2	0.23	0.58	0.05	0.03	0.04	0.00
Albedo	RMSE	0.15	0.04	0.11	0.11	0.06	0.07
	MBE	0.12	0.00	0.08	0.07	-0.01	0.02
	D_R^2	0.05	0.02	0.18	0.14	0.04	0.10
Net shortwave radiation	RMSE (Wm^{-2})	27.9	36.5	23.7	26.5	19.7	22.0
	MBE (Wm^{-2})	-12.1	25.7	-9.5	8.8	-4.6	-10.3
	D_R^2	0.24	0.21	0.26	0.32	0.31	0.29
Net longwave radiation	RMSE (Wm^{-2})	14.4	18.0	17.6	21.8	18.5	24.4
	MBE (Wm^{-2})	-2.9	-11.5	-1.5	-12.3	2.7	14.5
	D_R^2	0.40	0.54	0.06	0.02	0.23	0.19
Net Radiation	RMSE (Wm^{-2})	27.0	26.8	21.7	29.6	23.5	24.2
	MBE (Wm^{-2})	-13.1	14.8	-10.3	-2.4	-1.3	4.5
	D_R^2	0.13	0.00	0.18	0.14	0.04	0.04

Table 2-6 Coefficients and intercepts to calculate the fused surface radiation budget from six datasets. Coefficients and intercepts with p-value <0.05 are in bold.

	Intercept (Wm^{-2})	CFSR	MERRA	ERA-Interim	JRA-25	GEWEX-SRB	ISCCP-FD
Downward shortwave irradiance	**20.0473**	-0.0165	0.0836	0.0233	**0.2101**	**0.4508**	**0.1391**
Upward shortwave radiation	**8.2946**	-	**0.6806**	-0.0138	**-0.0689**	0.0807	0.0822
Downward longwave radiation	**22.6352**	**0.3471**	**0.1971**	**0.3477**	0.0543	0.0212	-
Upward longwave radiation	**44.7885**	-	**0.8975**	**0.1246**	**-0.2988**	**0.1814**	-

Table 2-7 compares RMSE_CV of the surface radiation budget components between CFSR, MERRA, ERA-Interim, JRA-25, GEWEX-SRB, and ISCCP-FD and the fused data. The fused downward shortwave irradiation, albedo, and net shortwave, longwave, and all-wave radiation exhibited the lowest RMSE_CVs over those by using individual datasets by 15.1 Wm^{-2}, 0.05, 15.8 Wm^{-2}, 13.4 Wm^{-2}, and 18.9 Wm^{-2}, respectively. The RMSE_CV of the fused upward shortwave radiation (9.7 Wm^{-2}) and upward longwave radiation (8.4 Wm^{-2}) is the second lowest after MERRA, while the RMSE_CV differences in the downward longwave radiation between JRA-25, CFSR, and the fused data are relatively small (<0.1 Wm^{-2}). Figure 2-2 illustrates scatter plots between fused data and ground measurements. The limited accuracy of the fused albedo may be explained by the error propagation in estimating the albedo as the ratio of upward shortwave radiation and downward shortwave irradiance. Nevertheless, the fused data maintain R^2 for the net radiation as high as 0.90 while keeping all other surface radiation budget components in good correlation with ground measurements.

Table 2-7 RMSE_CV of the downward, upward, and net shortwave radiation (DSW, USW, NSW) and longwave radiation (DLW, ULW, NLW), albedo, and net radiation (NR) from the fused data, other data fusion approaches (MLR: multiple linear regression; stepwise: stepwise regression; lasso: adapted lasso regression; PCA_2: principle analysis regression using first two principle components; PCA_3: principle analysis regression using first three principle components; BMA: Bayesian model averaging; RF: random forest; SVM: supported vector regression), reanalysis, and remote sensing datasets.

RMSE_CV	DSW (Wm^{-2})	USW (Wm^{-2})	Albedo	NSW (Wm^{-2})	DLW (Wm^{-2})	ULW (Wm^{-2})	NLW (Wm^{-2})	NR (Wm^{-2})
				1997-2007				
Fusion, MLR	15.1	9.7	0.05	15.8	13.3	8.4	13.4	18.9
Fusion. Stepwise	15.1	9.8	0.05	15.9	11.2	9.2	12.9	17.0
Fusion, lasso	15.2	9.7	0.05	15.8	10.8	9.3	13.0	17.1
Fusion, PCA_2	15.3	10.2	0.05	16.6	10.3	9.5	13.6	16.9
Fusion, PCA_3	15.0	10.3	0.05	15.7	10.4	9.3	13.1	16.0
Fusion, BMA	15.1	9.7	0.05	15.7	10.8	9.6	13.3	17.7
Fusion, RF	14.3	9.8	0.05	15.3	11.0	10.8	14.1	17.7
Fusion, SVM	14.6	10.5	0.05	16.0	10.7	9.6	13.8	16.9
CFSR	21.2	11.2	0.06	22.0	13.2	11.6	14.2	24.2
MERRA	18.1	9.2	0.05	18.1	15.1	8.1	13.9	18.9
ERA-Interim	22.6	12.6	0.06	21.2	14.2	13.5	19.0	26.7
JRA25	17.8	13.8	0.06	16.1	13.2	23.5	20.0	24.4
GEWEX-SRB	16.4	11.3	0.06	20.0	19.8	17.6	18.4	22.6
ISCCP-FD	16.9	11.3	0.06	18.6	32.2	28.1	19.9	21.4
GLDAS-1-CLM	27.2	13.9	0.06	23.3	21.8	16.2	22.1	24.9
GLDAS-1-MOS	27.2	13.0	0.05	22.1	21.8	16.0	22.1	23.1
GLDAS-1-NOAH	27.2	11.7	0.05	23.9	21.8	18.5	23.3	23.2
GLDAS-2-NOAH	17.2	10.2	0.05	18.2	21.2	13.6	18.9	20.1
NRA-1	20.3	12.5	0.05	15.8	16.4	24.5	20.7	21.8
NRA-2	22.9	13.7	0.05	16.4	18.4	21.8	21.3	23.4
				2000-2007				
Fusion	14.8	8.9	0.05	16.2	14.1	8.6	13.8	17.8
CERES SYN	16.5	8.8	0.05	17.6	17.6	16.2	18.2	22.5

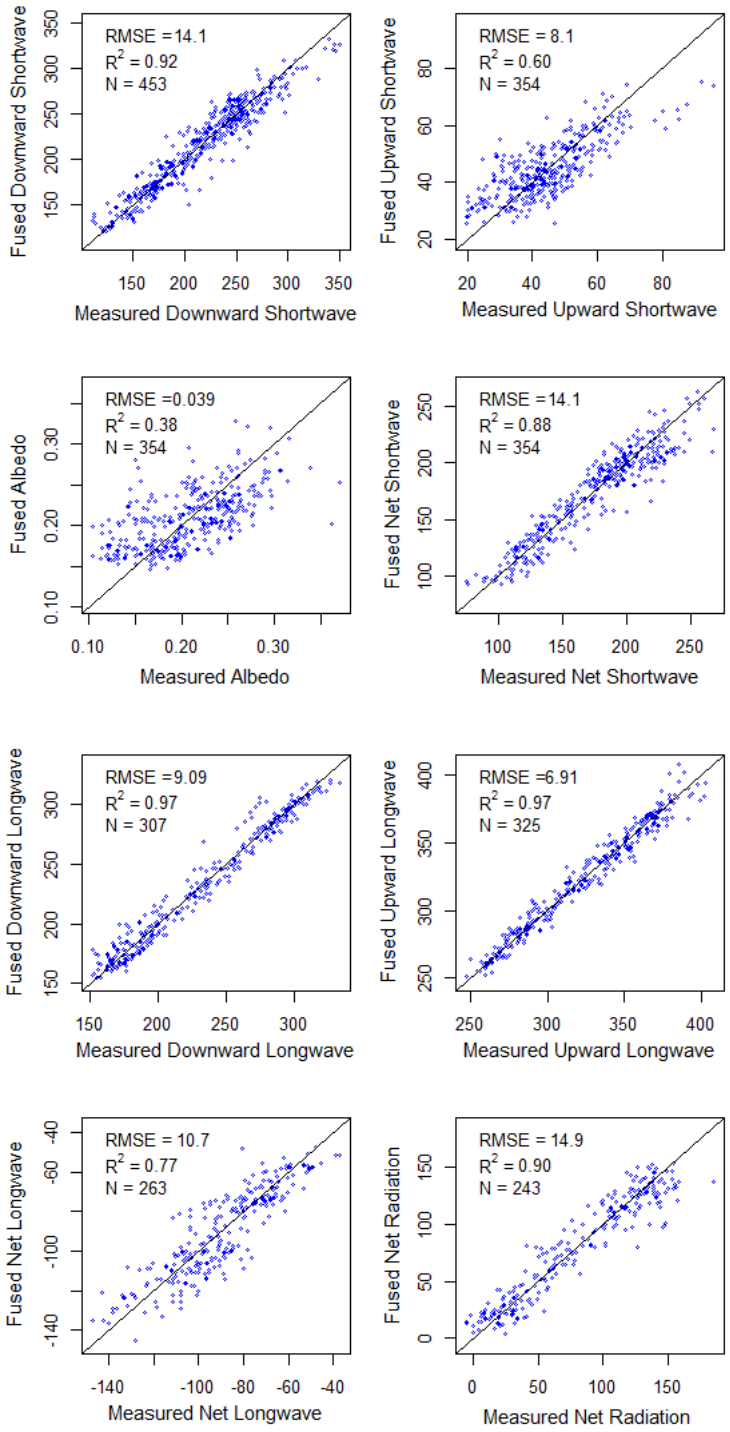

Figure 2-2 Comparison of the fused downward, upward, and net shortwave radiation, albedo, and net radiation with ground measurements from AsiaFlux, ChinaFLUX, CAME/Tibet, and CAMP/Tibet. Units are Wm^{-2} except for albedo.

In order to quantify the advantages of the data fusion method comprehensively, the fused data was compared with multiple datasets during all available years, including the NCEP and National Center for Atmospheric Research (NCAR) reanalysis 1 (NRA-1) [*Kalnay et al.*, 1996], the NCEP Department of Energy (NCEP–DOE) Atmospheric Model Intercomparison Project reanalysis (NRA-2) [*Kanamitsu et al.*, 2002], the 1° Regional Radiative Fluxes and Clouds product from the Clouds and the Earth's Radiant Energy System (CERES SYN, edition 3A) [*Wielicki et al.*, 1996], and the Global Land Data Assimilation Systems version 1 and version 2 products (GLDAS-1, GLDAS-2) [*Rodell et al.*, 2004], including three offline models: the Common Land Model version 2.0 (GLDAS-1-CLM) [*Oleson et al.*, 2004], the Mosaic Model (GLDAS-1-MOS) [*Koster and Suarez*, 1996], and the National Centers for Environmental Prediction/Oregon State University/Air Force/Hydrologic Research Lab Model version 2.7 (GLDAS-1-NOAH, GLDAS-2-NOAH) [*Chen et al.*, 1996; *Koren et al.*, 1999; *Ek et al.*, 2003]. The results in Table 2-7 prove that the fused data are more accurate, that they exhibit lower RMSE_CV than that obtained using the corrected products individually, except in the case of fused upward shortwave radiation, where they exhibit a difference of less than 0.1 Wm^{-2} from CERES SYN. The RMSE_CV of albedo from the fused data is lower than that from most of the corrected datasets and is similar to GLDAS-2-NOAH and CERES SYN. In contrast to the data assimilation framework of GLDAS using offline modeling, the data fusion method presented in this study integrates estimations of shortwave and longwave radiation from reanalysis and remote sensing products directly using the multiple linear regression data fusion method, while also attaining RMSE_CV of less than 20 Wm^{-2} for all monthly shortwave and longwave fluxes over the Tibetan Plateau.

2.3.2 Comparisons of seasonal and interannual variability

The seasonal variations in the surface radiation budget from six products are compared with the ground-measured values averaged over all available sites as shown in Figure 2-3. The fused products are also plotted, merely to illustrate the seasonal cycles of surface radiation budget components after data fusion using six products and ground observations. GEWEX-SRB and ISCCP-FD underestimate downward shortwave irradiance in late autumn and winter. By contrast, CFSR and ERA-Interim exhibit large positive bias in spring with sharp decreases in summer, and MERRA and JRA-25 overestimate downward shortwave irradiance significantly in spring and summer. ISCCP overestimates albedo in winter and spring, and CFSR, ERA-Interim, and JRA-25 overestimate albedo in winter and spring. All datasets except ISCCP-FD are more consistent with ground measurements for longwave fluxes than for shortwave fluxes. Previous studies have found that the positive biases of the downward longwave radiation over the Tibetan Plateau in ISCCP-FD result primarily from errors sourced introduced by input data and elevation differences [*Yang et al.*, 2006; *Gui et al.*, 2010], while the temporally insufficient sampling of ISCCP cloud data limits the accuracy of downward longwave radiation for GEWEX-SRB and ISCCP-FD. Overall, the monthly biases from each reanalysis and remote sensing dataset vary seasonally, and no product is better than other products in all surface radiation budget components, which indicates the importance to synthesize multiple datasets to minimize the limitations from each product. After data fusion, the fused surface radiation budget components capture seasonal cycles well when compared to ground measurement, overcoming the significant differences of monthly bias error in the six original products.

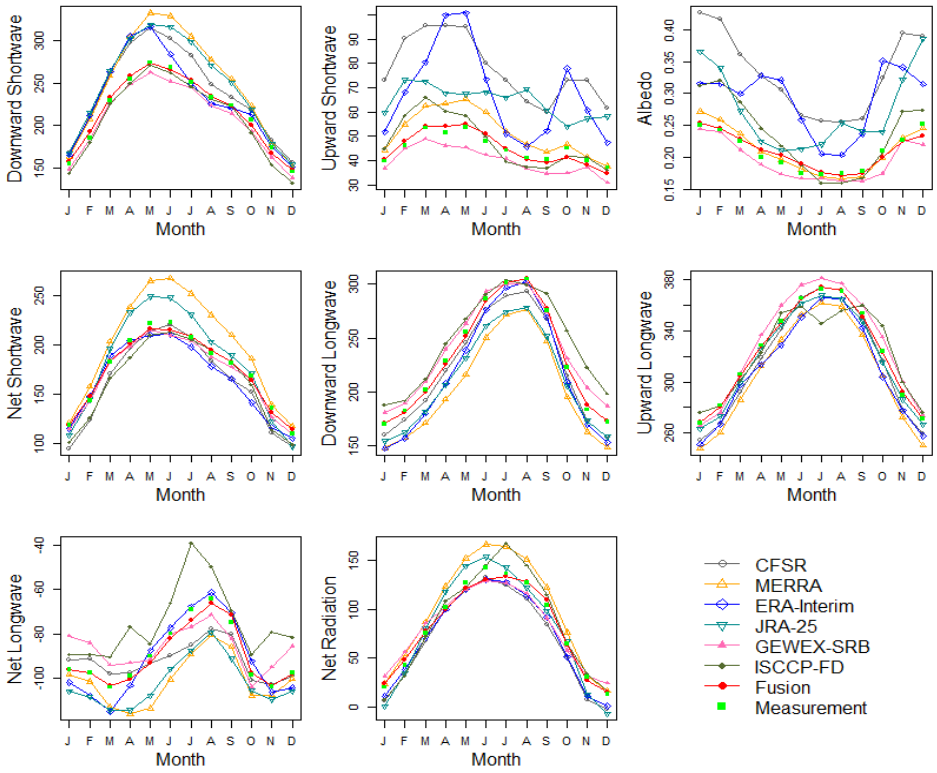

Figure 2-3 Monthly cycles of the surface radiation budget from multiple datasets and fused data with ground measurements averaged for all available sites from AsiaFlux, ChinaFLUX, CAME/Tibet, and CAMP/Tibet. Units are Wm^{-2}, except for albedo.

A comparison between the original reanalysis, remote sensing, and fused datasets and the ground-measured data of nine sites, using extended downward shortwave irradiance records from CMA radiation sites, is necessary to test whether the fused dataset is adequate to represent decadal trends and annual/seasonal variation. Figure 2-4 compares the annual and seasonal downward shortwave irradiance anomalies (relative to the average value from 1995 to 2005) from six original datasets, the fused dataset, and the ground observations**,** and Table 2-8 reports the correlations and decadal changes of the downward shortwave irradiance in four seasons and at the annual scale. The decadal trend was detected using the linear regression method and student t-test for significance. Although not calibrated to CMA radiation sites, the correlation is the highest between the

fused downward shortwave irradiance and CMA radiation sites in most seasons, suggesting that the data fusion method advances the fidelity of the downward shortwave irradiance through the synthesis of multiple products. Furthermore, the fused data as well as CFSR, GEWEX-SRB, and ISCCP-FD captures the significant decreasing trend (p-value < 0.05) of the downward shortwave irradiance in summer and at the annual scale. Therefore, it could be argued that the fused monthly surface radiation budget over the Tibetan Plateau is a valid synthesis for environmental and climatic studies, based on its higher correlation to independent observed downward shortwave irradiance (Table 2-8) and the greater accuracy (RMSE_CV) achieved by this method than by correcting each product individually (Table 2-7).

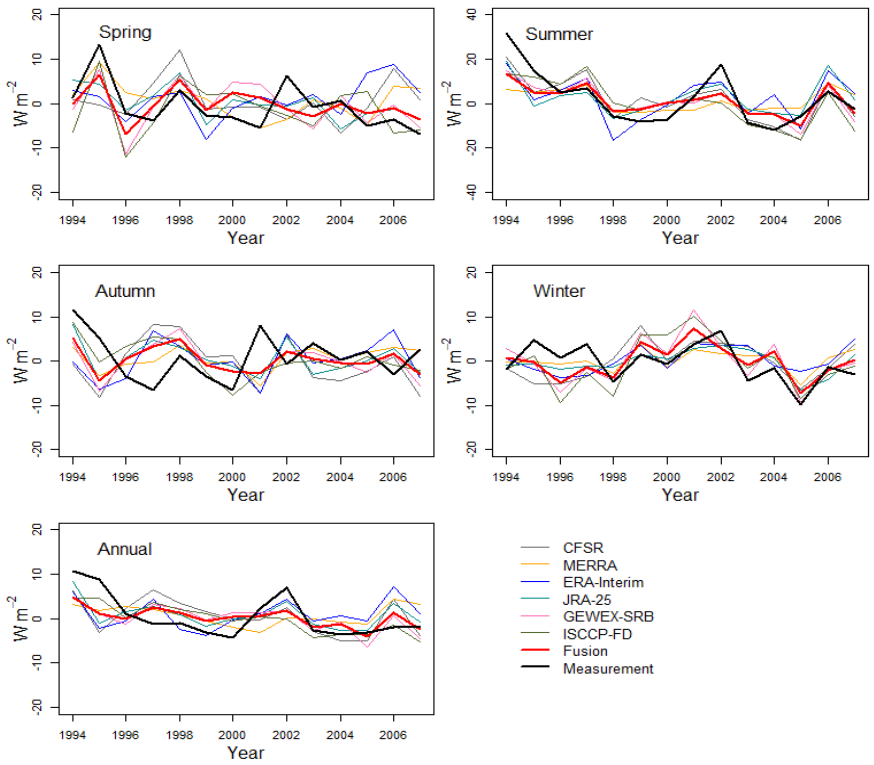

Figure 2-4 Comparison of the downward shortwave irradiance anomalies from original datasets, fused data, and ground measurements averaged over nine CMA radiation sites over the Tibetan Plateau.

Table 2-8 Correlation and decadal changes (Wm^{-2} $decade^{-1}$) of the downward shortwave irradiance from fused data, six original products, and CMA radiation sites averaged over nine available sites (correlation coefficient and slopes of decadal changes with p-value <0.05 is in bold).

	Spring	Summer	Autumn	Winter	Annual
		Correlation coefficient (1994-2007)			
CFSR	-0.06	0.80	-0.58	0.23	0.31
MERRA	0.46	0.65	-0.07	0.58	0.30
ERA-Interim	-0.09	0.69	-0.49	0.13	0.31
JRA25	0.48	0.77	-0.10	0.55	0.63
GEWEX-SRB	0.46	0.80	-0.10	0.58	0.53
ISCCP-FD	0.49	0.71	**0.32**	0.59	0.64
Fusion	**0.58**	**0.83**	-0.03	**0.61**	**0.65**
		Decadal changes (1994-2007)			
CMA radiation sites	-7.3	**-18.8**	-1.9	-5.0	**-8.1**
CFSR	-1.1	**-18.4**	-4.5	3.3	**-5.8**
MERRA	-3.9	-3.0	2.3	0.8	-0.8
ERA-Interim	4.5	-3.1	2.9	3.3	1.3
JRA25	**-6.6**	-3.0	-3.4	-0.2	-3.5
GEWEX-SRB	-3.1	**-14.5**	-2.8	-0.9	**-5.8**
ISCCP-FD	-1.8	**-23.0**	-6.1	0.9	**-8.3**
Fusion	-3.3	**-10.4**	-2.5	-0.2	**-4.4**

2.3.3 Uncertainties of the fused surface radiation budget

Uncertainties from reanalysis datasets (CFSR, MERRA, ERA-Interim, JRA-25) are introduced from multiple sources, including the assimilated observations, assimilation schemes, and numerical models. The lack of ground observations impedes assessment of the uncertainty of the surface radiation budget over the Tibetan Plateau; similarly, the currently available ground measurements are spatially sparse, particularly in the western plateau and the southeastern valley and ranges, and temporally limited (few stations have continuous observations for multiple years). In addition, the instrumental error and operation-related error could also contribute to the uncertainty of the ground-observed radiation budget over the Tibetan Plateau [*You et al.*, 2012]. The uncertainties within the

radiative transfer model and inputs (such as water vapor, cloud, and aerosol) may also impact the accuracy of surface radiation budget from GEWEX-SRB and ISCCP-FD. A previous study has shown that the errors in longwave fluxes are contributed from inputs errors of skin temperature (the upward longwave radiation) and water vapor (the downward longwave radiation) over the Tibetan Plateau [*Gui et al.*, 2010]. Moreover, the factors affecting the uncertainty in the downward shortwave irradiance from GEWEX-SRB and ISCCP-FD have been identified in full-sky (terrain complexity) and clear-sky (inputs and models) conditions [*Yang et al.*, 2008b]. The weak D_R^2 values of the albedo and longwave fluxes from ISCCP-FD and GEWEX-SRB indicate that large uncertainties remain in monthly in all-sky conditions.

The horizontal scale and spatial homogeneity is of great importance in determining the surface radiation budget in the Tibetan Plateau. To assess the impact of spatial scale on the fused data, the data fusion method was applied at seven spatial resolutions (scales): 0.1°, 0.3°, 0.5°, 1.0°, 1.5°, 2.0°, and 2.5°. In general, RMSE_CV of the fused data exhibits limited change (<15 Wm^{-2}) at multiple scales, and changes of RMSE_CV across scales are much smaller for the downward shortwave/longwave radiation than that for the upward shortwave/longwave radiation and albedo (Figure 2-5). RMSE_CV of the fusion data is smaller than or similar to that of the corrected product, with lowest RMSE_CV values at all seven scales for downward/upward shortwave/upward fluxes, providing evidence that accuracy can be improved by combining information from multiple products within the multiple linear regression fusion method. A scale of 0.5° was selected for three reasons: 1) it exhibits the lowest RMSE_CV of the downward shortwave irradiance and the upward longwave radiation at

all scales; 2) the difference in RMSE_CV for the downward/upward shortwave and longwave radiation at spatial resolutions between 0.5° and 0.1°, 0.3° is less than 1 Wm^{-2}; and 3) the scale of input datasets varies from 0.31° for CFSR to 2.5° for ISCCP.

Since radiation fluxes are related to elevation, the elevation adjustment was conducted according to the difference between the elevation of in situ sites and the corresponding grids. The altitudinal dependence followed the relationship defined by the alpine surface radiation budget network, and was 1.3 $Wm^{-2}100m^{-1}$, 2.4 $Wm^{-2}100m^{-1}$, -2.9 $Wm^{-2}100m^{-1}$, and -2.6 $Wm^{-2}100m^{-1}$ for the downward shortwave irradiance, the upward shortwave radiation, the downward longwave radiation, and the upward longwave radiation, respectively [*Marty et al.*, 2002]. The results are shown in Figure 2-6, which indicate that the impact of elevation adjustment on the RMSE_CV of the shortwave fluxes from the fused datasets is relatively low (<2 Wm^{-2}). Conversely, RMSE_CV of the longwave fluxes for most of the products decrease significantly after elevation adjustment, improving D_R^2 for most products. Therefore, this study only applied elevation adjustments to the downward and upward longwave radiation.

The method of generating the fused datasets is another crucial factor that may affect the accuracy of the fused surface radiation budget over the Tibetan Plateau; thus, RMSE_CV for the multiple linear regression data fusion method was compared with other multiple linear regression models (stepwise regression, lasso regression, and PCA regression) and advanced statistical methods (BMA, RF, and SVM) as shown in Table 2-7. Even though none of the those models outperformed in all eight surface radiation budget components, the multiple linear regression data fusion method was used in this study for its simplicity, relatively low RMSE_CV, and limited difference below 3 Wm^{-2}

(for surface radiation budget components except albedo by 0.001) compared to those models with the lowest RMSE_CVs.

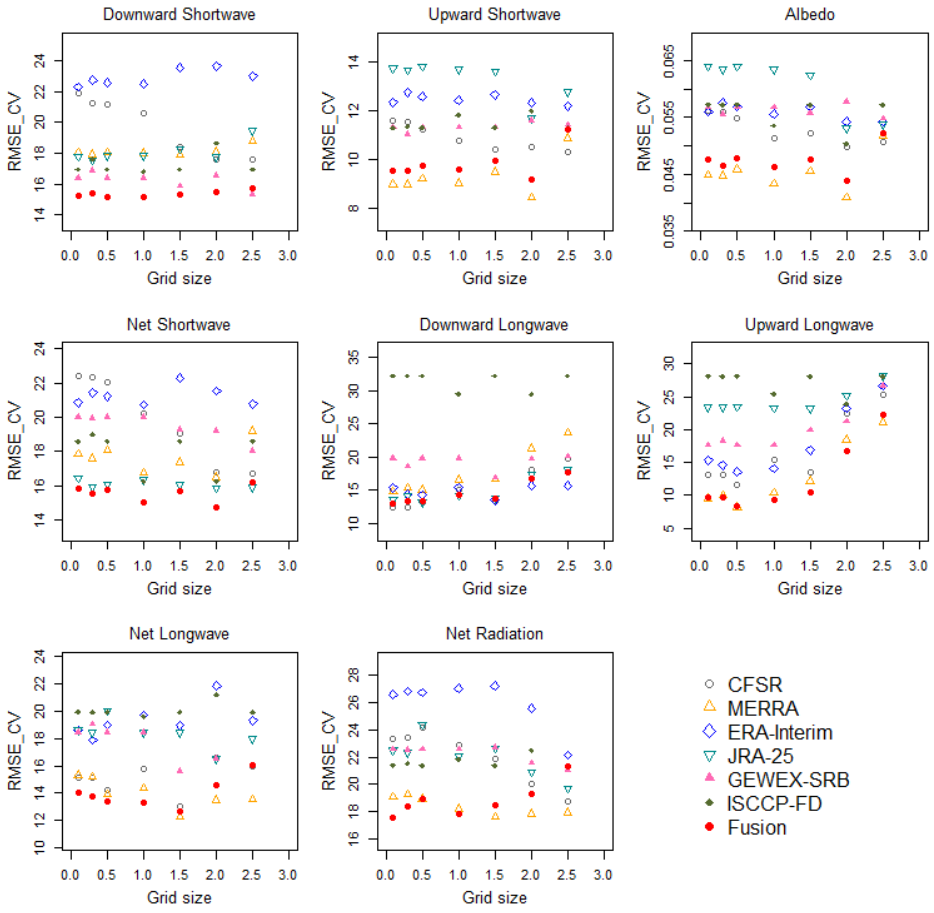

Figure 2-5 Comparison of the RMSE_CV (units are Wm^{-2}, except for albedo) of the surface energy budget components at multiple scales (°) from original datasets and fused data.

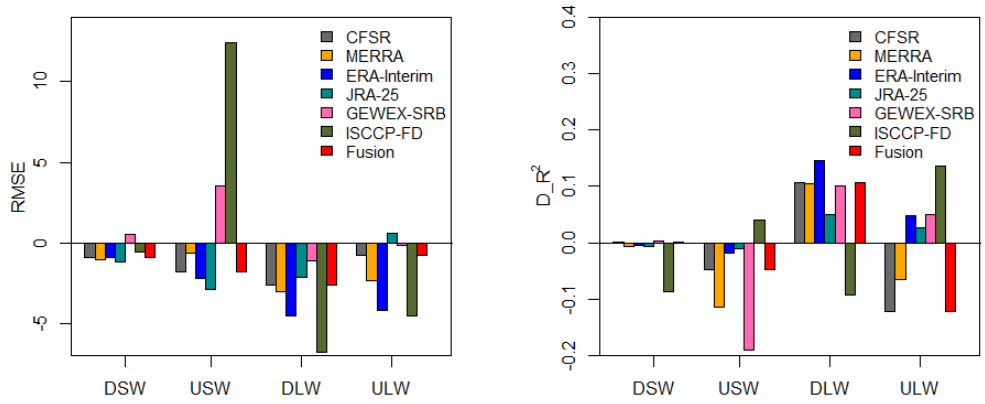

Figure 2-6 Difference of RMSE (left) and D_R^2 (right) after elevation adjustment of downward and upward shortwave radiation (DSW, USW) and longwave radiation (DLW, ULW) from fused data and original datasets.

2.3.4 Spatial and seasonal variability of the shortwave radiation fluxes

The spatial distribution of annual and seasonal means and STD in the downward shortwave irradiance is shown in Figure 2-7 for the fused data over the entire Tibetan Plateau calculated from 1984 to 2007. The seasonal downward shortwave irradiance varies with latitude in the western Tibetan Plateau and with elevation in the eastern Tibetan Plateau, and there is a significant seasonal migration of the high downward shortwave irradiance areas over the Tibetan Plateau. The STD of downward shortwave irradiance exhibits the greatest spatial variation in autumn and the least differences in winter when the climate is cold and dry. Annually, the downward shortwave irradiance is high in the southwestern Tibetan Plateau and low in valleys in the southeastern Tibetan Plateau, while the STD is high in the northern Tibetan Plateau and low in the southeastern Tibetan Plateau. The uncertainty (2σ) of the mean and STD is below 2 Wm^{-2} with high value in the western Tibetan Plateau and the southern ranges and valleys (Figure 2-8). The seasonal and annual downward shortwave irradiance anomalies

averaged over the Tibetan Plateau are negatively correlated to cloud cover and positively correlated to temperature range anomalies (Table 2-9). It is noteworthy that cloud cover observations from ground stations often lack representative coverage at the regional scale owing to the high variability in cloud cover both temporally and spatially; therefore, temperature range is also compared with downward shortwave irradiance to infer integrated changes from cloud cover, duration, and types indirectly. In summer cloud cover and temperature range exhibit the highest correlation with the downward shortwave irradiance (by -0.66 and 0.92, respectively). A significant negative (positive) correlation can also be found between the downward shortwave irradiance and cloud cover (temperature range) in autumn and winter.

The analysis of the downward shortwave irradiance in association with cloud cover and temperature range indicates that cloud cover is an essential factor that is related to the interannual variability of downward shortwave irradiance in all four seasons. The underlying processes include the absorption and reflection of radiation by cloud; thus, the results presented here confirm that the interannual variability of the amount of solar irradiance reaching the surface is largely determined by the presence of cloud. In the Tibetan Plateau, with average elevations above 4000 m, both the direct impact of aerosol absorption and scattering and the indirect impact of aerosols on cloud formation have been suggested to be much lower than the observed dimming [*Yang et al.*, 2012]. The third actor contributing to the downward shortwave irradiance is the absorption from various radiative active gases, which induces the summer dimming over the Tibetan Plateau that is consistent with the observed moistening trend [*Yang et al.*, 2012]. However, in those exceptional years when the downward shortwave irradiance and cloud

cover anomalies covary (i.e., both exhibit large fluctuations in the same direction), temperature range is well correlated with cloud cover variation. This may be explained by changes of cloud types. The impacts of variations in deep convective clouds have been shown in a previous study to exhibit consistent negative correlations with the downward shortwave irradiance over CMA sites in the Tibetan Plateau [*Yang et al.*, 2012]. Conversely, the covariability between the downward shortwave irradiance and temperature range implies the close connection between these factors by the solar (daytime) heating that affects the maximum temperature [*Bristow and Campbell*, 1984]. Unlike cloud cover, which is directly related to the interannual variability of downward shortwave irradiance, temperature range is considered to be an indirect confirmatory indicator of downward shortwave irradiance and cloud cover variation [*Liu et al.*, 2004; *Ye et al.*, 2010; *Wild*, 2012]; this supports the importance of downward shortwave irradiance variation in association with regional temperature changes over the Tibetan Plateau.

The spatial distribution of albedo over the Tibetan Plateau reflects the land surface conditions over the Tibetan Plateau. Annually, the albedo is high and low in the northwestern and eastern Tibetan Plateau, respectively (Figure 2-9). The annual STD of albedo peaks in the Karakorum range, the west part of the Himalaya range, and the southeastern ranges and valleys. Overall, albedo distribution is related to land surface heterogeneity and land cover, especially snow cover, which also influences the spatial distribution of the STD of albedo in highly complex terrain. The uncertainty of albedo is below 0.01, which displays hotspots in the western ranges of the Tibetan Plateau (Figure 2-10). Correlation between the albedo and snow cover is positive and statistically

significant in autumn and winter, while NDVI is negatively correlated with the albedo in summer and autumn. The weaker correlation of albedo variation with snow cover and NDVI in summer is possibly related to factors such as land cover change and the impact of cloud on the accuracy of albedo measurement. The annual variation in albedo is also significantly correlated with both snow cover and NDVI by 0.51 and -0.48, respectively.

The surface albedo, as the ratio between downward shortwave irradiance and upward shortwave radiation, is an integration of reflectivity over the shortwave spectrum [*Liang et al.*, 2010], acting as an optical signature of the land surface. In general, snow has a high albedo and vegetation a relatively low albedo, but the albedo of vegetation is also impacted by highly reflective backgrounds such as snow. NDVI [*Tucker*, 1979] is an indicator of the present and health of living green vegetation and is based on the biophysical characteristics of vegetation that has low reflectivity in the red spectrum and high reflectivity in the near-infrared spectrum. The weak correlation between albedo and snow cover in spring may be related to the mosaic surface created by snow, vegetation, and the freezing thaw cycle of soil in spring. Changes in snow cover can alter the albedo directly, but can also affect albedo indirectly by altering moisture conditions to support plant growth. Interestingly, the major peaks and drops of albedo anomalies at both the seasonal and annual scales are consistent with those for snow cover or NDVI. This indicates that albedo may be sensitive to extreme surface atmospheric conditions such as those are detected from snow cover and NDVI extremes over the Tibetan Plateau, a theory that has been suggested previously based on a case study of 2003 European heat waves at the regional scale [*Teuling and Seneviratne*, 2008]. In addition, vegetation growth as indicated from NDVI might be linked to changes of the diffuse radiation

components of downward shortwave irradiance [*Wild*, 2012], which can alter the surface albedo substantially as reflectivity changes. In order to elucidate the effects of non-vegetated land cover, similar analyses were conducted over vegetated areas with the maximum annual NDVI > 0.1 [*Piao et al.*, 2003]; the result obtained indicate a pattern of seasonal and annual covariability (not shown) that is similar to that of averaging over the entire Tibetan Plateau.

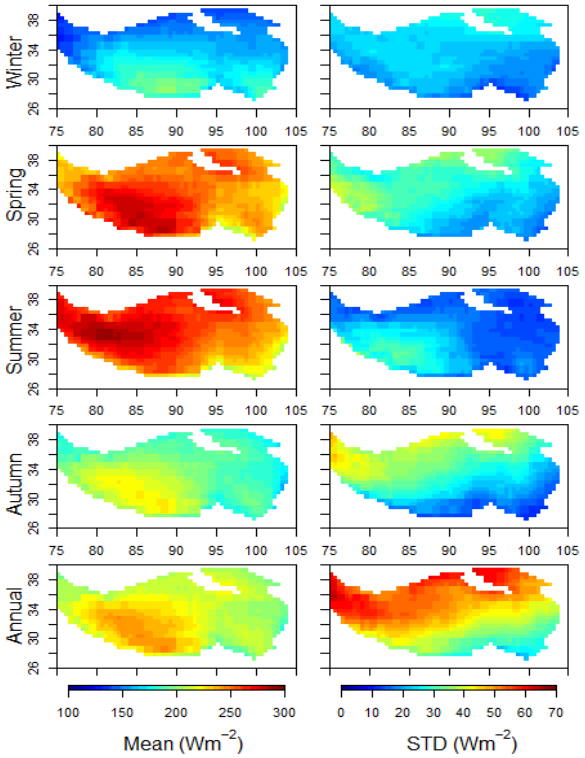

Figure 2-7 Spatial distribution of mean and STD of the fused downward shortwave irradiance over the Tibetan Plateau (1984-2007).

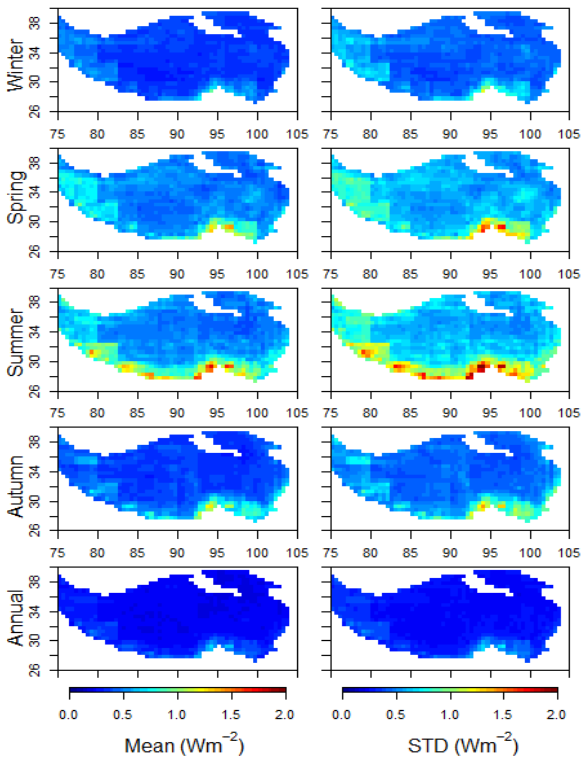

Figure 2-8 Spatial distribution of the uncertainty (2σ) of mean and STD of the fused downward shortwave irradiance over the Tibetan Plateau (1984-2007).

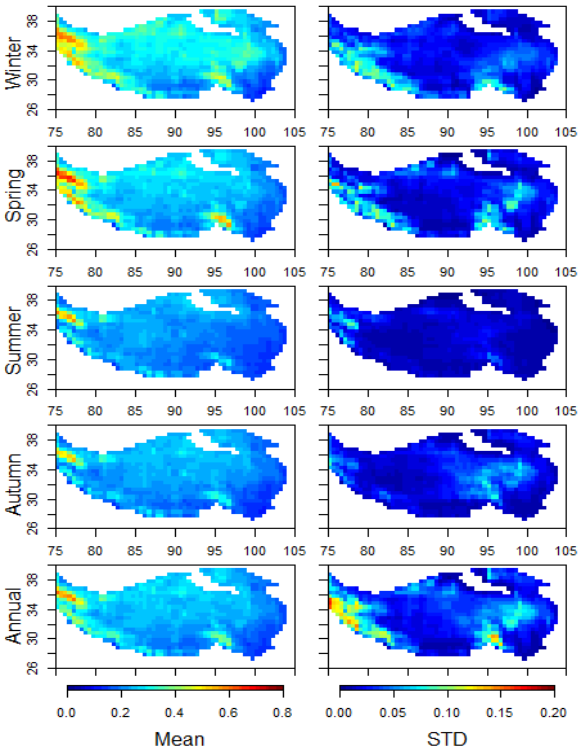

Figure 2-9 Spatial distribution of mean and STD of the fused albedo over the Tibetan Plateau (1984-2007).

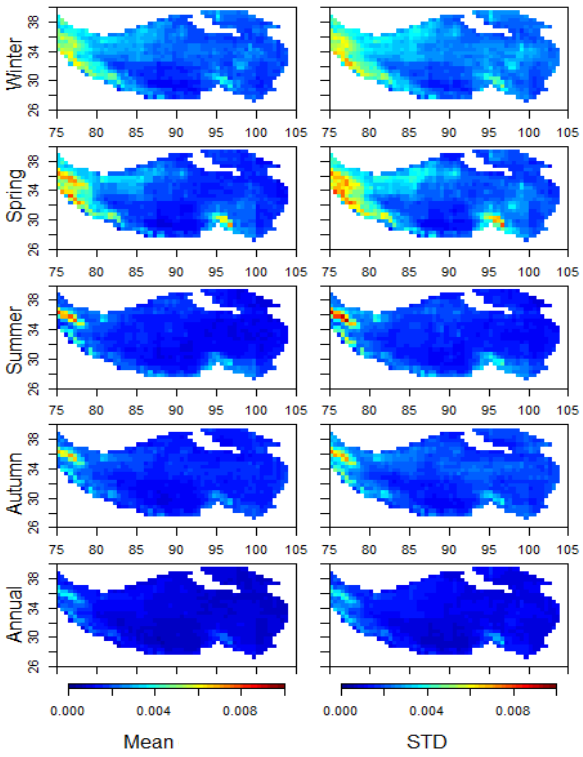

Figure 2-10 Spatial distribution of the uncertainty (2σ) of mean and STD of the fused albedo over the Tibetan Plateau (1984-2007).

Table 2-9 Correlation coefficients (p-value <0.1 are in bold) between the surface radiation budget and surface and atmospheric anomalies

Correlation coefficient	Annual	Spring	Summer	Autumn	Winter
Downward shortwave radiation, cloud cover	**-0.38**	-0.13	**-0.66**	**-0.49**	**-0.36**
Downward shortwave radiation, temperature range	**0.57**	**0.48**	**0.92**	**0.81**	**0.67**
Albedo, snow cover	**0.51**	0.11	0.12	**0.81**	**0.38**
Albedo, NDVI	**-0.48**	-0.09	-0.28	**-0.70**	**-0.73**
Downward longwave radiation, water vapor	**0.92**	**0.62**	**0.98**	**0.89**	**0.89**
Downward longwave radiation, cloud cover	0.32	0.23	**0.57**	**0.44**	**0.38**
Upward longwave radiation, temperature	**0.86**	**0.90**	**0.82**	**0.82**	**0.85**
Upward longwave radiation, NDVI	**0.39**	0.27	**0.44**	**0.37**	**0.40**
Net radiation, cloud cover	-0.05	-0.10	-0.27	-0.09	-0.29
Net radiation, temperature range	0.02	0.19	**0.58**	**0.45**	0.08
Net radiation, water vapor	-0.01	**0.49**	**-0.37**	0.31	-0.14
Net radiation, mean temperature	-0.16	**0.34**	-0.29	0.05	-0.10
Net radiation, NDVI	0.27	-0.04	0.15	**0.69**	**0.58**
Net radiation, snow cover	0.03	0.30	0.08	-0.25	**-0.41**

2.3.5 Spatial and seasonal variability of the longwave radiation fluxes

The downward longwave radiation displays a similar pattern for both seasonal and annual mean values as shown in Figure 2-11: low in the central western Tibetan Plateau and high in the outer Tibetan Plateau, with maximum values at the southeast boundary of the Tibetan Plateau. The downward longwave radiation exhibits high variation in autumn and low values in winter and summer. The uncertainty of downward longwave radiation is below 1.5 Wm^{-2}, and the high value is located along the southern ranges of the Tibetan Plateau (Figure 2-12). The temporal variation in the seasonal downward longwave radiation averaged over the Tibetan Plateau is associated with water vapor and cloud cover anomalies. Since water vapor is the most abundant greenhouse gas that emits the longwave radiation and cloud is an important radiator of the longwave radiation, the downward longwave radiation is positively related to water vapor and cloud cover, particularly in summer, with correlation by 0.98 and 0.57, respectively.

In principle, the downward longwave radiation is determined by the atmospheric temperature and emissivity, which varies according to cloud and greenhouse gases that can absorb and emit radiation in the thermal infrared spectrum. In most cases, water vapor has more power to explain the interannual variability of downward longwave radiation, which is supported by the fact that water vapor is the dominant emitter of longwave radiation [*Wang and Liang*, 2009]. The results presented here indicate that cloud might be another important factor influencing the downward longwave radiation interannual variability over the Tibetan Plateau. This relationship between the downward longwave radiation and cloud cover is more obvious when a divergence or significant drops and peaks occur in the interannual variation in downward longwave radiation and

water vapor. Similar to the method by which the all-sky downward longwave radiation can be estimated based on the clear-sky emissivity from water vapor pressure and the adjustment of cloud effects using the cloud fraction, the correlation between cloud cover and the downward longwave radiation elucidated in this study may be explained by the positive relationship between the longwave radiation emitted from cloud, which contributes to the cloudy-sky downward longwave radiation; conversely, the clear-sky downward longwave radiation is determined primarily by water vapor. Over the Tibetan Plateau, the cloud cover varied primarily in the same direction as the water vapor, acting to amplify the interannual variability of downward longwave radiation in a consistent manner.

The spatial characteristics of seasonal upward longwave radiation are impacted by surface temperature, land cover, and elevation. In four seasons, high values of the upward longwave radiation are displayed in the mid–west plateau and at the low elevation boundaries (Figure 2-13). STD of the upward longwave radiation is extremely low in winter and summer, and the annual distribution of STD exhibits a decreasing pattern along the elevation gradient, with peaks in the western plateau and in the northeast basin and ranges. The uncertainty of upward longwave radiation reaches its largest value over the western boundary in summer (<1 Wm^{-2}) as shown in Figure 2-14. The upward longwave radiation covaries with temperature and NDVI over the Tibetan Plateau at both the seasonal and annual scale. In winter and spring, the upward longwave radiation increases with increasing temperature with positive correlation as high as 0.90 and 0.85, respectively.

The upward longwave radiation is governed by the Stefan–Boltzmann law, which states that the upward longwave radiation is determined by the surface emissivity and surface skin temperature. A recent study has shown that the skin temperature over the Tibetan Plateau exhibits very similar annual and monthly variations to those of the 2m air temperature measured in the morning [*Salama et al.*, 2012]. There is no observation system in existence that collects frequent and continuous observations of high-quality skin temperature that cover the study period; therefore, the 2m air temperature is used as a proxy for the skin temperature. In addition, the presence and density of vegetation cover can alter the surface emissivity; moreover, warmer temperature favors vegetation growth, especially promoting the growth of vegetation under cold stress conditions [*Bounoua et al.*, 2000]. Those processes are supported by patterns for which major peaks and drops in the upward longwave radiation correlate well with changes in NDVI.

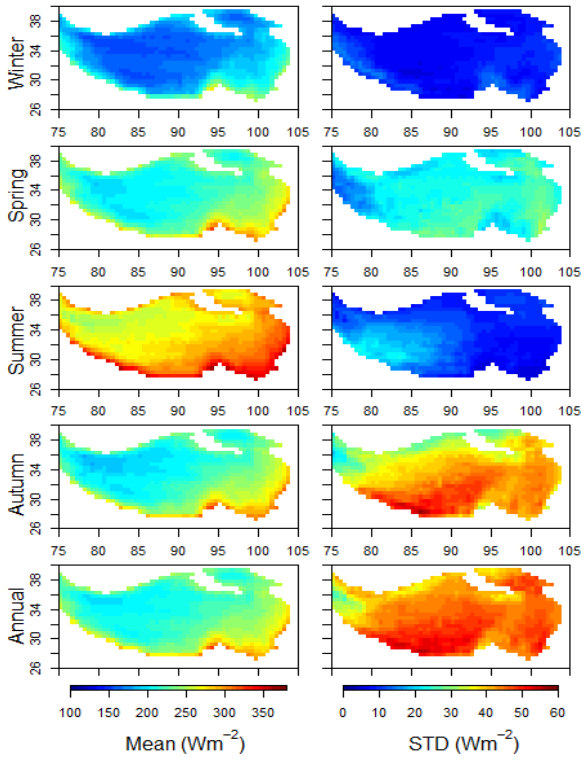

Figure 2-11 Spatial distribution of mean and STD of the fused downward longwave radiation over the Tibetan Plateau (1984-2007).

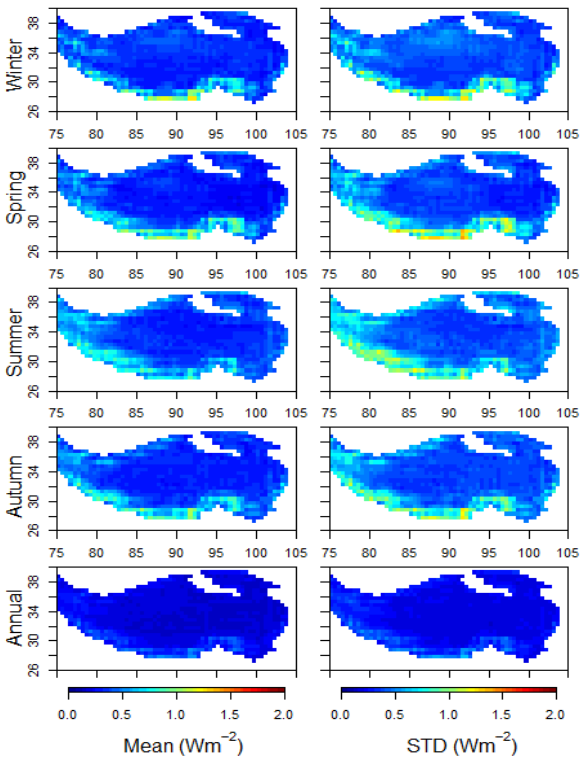

Figure 2-12 Spatial distribution of the uncertainty (2σ) of mean and STD of the fused downward longwave radiation over the Tibetan Plateau (1984-2007).

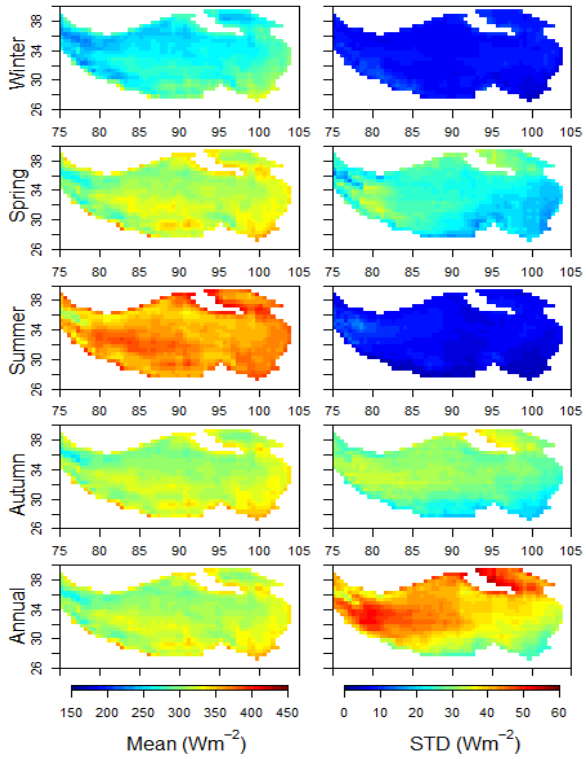

Figure 2-13 Spatial distribution of mean and STD of the fused upward longwave radiation over the Tibetan Plateau (1984-2007).

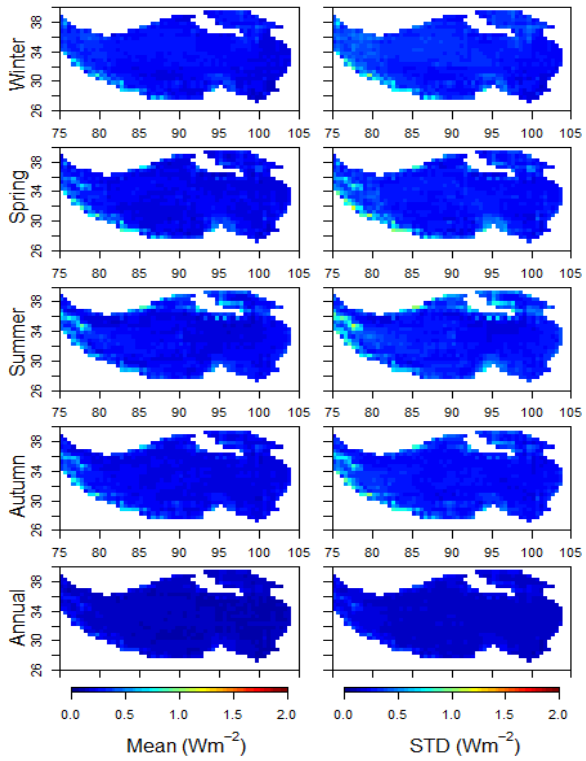

Figure 2-14 Spatial distribution of the uncertainty (2σ) of mean and STD of the fused upward longwave radiation over the Tibetan Plateau (1984-2007).

2.3.6 Spatial and seasonal variability of the net radiation

The net radiation displays seasonal cycles over the Tibetan Plateau, with the lowest and highest values in winter and summer, respectively, and the second lowest values in autumn (Figure 2-15). In each season, the northern Tibetan Plateau exhibits the lowest net radiation, while the eastern Himalaya range, southeastern ranges and valleys exhibit the highest net radiation. Annually, the net radiation decreases from southeast to northwest in the eastern Tibetan Plateau, while an anomaly exists between the south and north in the western Tibetan Plateau. The southern and eastern outer Tibetan Plateau tends to display higher net radiation than the inner plateau. The STD of net radiation is low in winter and summer and displays a similar pattern to spring in autumn, with high value in the inner Tibetan Plateau and lower value at the boundaries. Annually, the STD

is low in the southwest and high in the middle and northern parts of the eastern Tibetan Plateau. The uncertainty of the seasonal mean and STD of net radiation is high in spring and summer (<3 W m^{-2}) with the hotspots over the western ranges and the southeastern valleys over the Tibetan Plateau (Figure 2-16). In contrast to each of the surface radiation budget components (i.e., shortwave and longwave fluxes), the net radiation is regulated by multiple factors in association with both surface and atmospheric conditions. In spring, a significant positive correlation between water vapor and the net radiation based on the emitted infrared radiation from water vapor; changes in temperature are also associated with net radiation. In summer, the covariation of net radiation and temperature range is strong, and net radiation is also negatively correlated with water vapor through absorption of downward shortwave irradiance. In autumn, NDVI is closely related to the net radiation, and water vapor is positively related to the net radiation through regulation of the downward longwave radiation. In winter, net radiation is related primarily to snow cover.

What are the implications of the relationships between the net radiation and surface or atmospheric conditions in each season? In contrast to the positive correlation between the net radiation and water vapor in spring and autumn, the negative correlation between the net radiation and water vapor in summer indicates the shift of the relative relationship between water vapor and the net radiation from the downward longwave radiation to the downward shortwave radiation. This suggests that the water vapor absorption of solar radiation and its association with cloud formations regulates the summer variability of net radiation over the Tibetan Plateau substantially. The correlation between water vapor and the net radiation is not significant in winter, possibly owing to

the dry climate that prevails over the Tibetan Plateau, when water vapor has less power to explain the variation in the net radiation than other related conditions. Winter snow cover is inversely related to the net radiation by the dominant impact from positive relationship of snow cover to albedo and negative relationship of albedo to the net radiation, while the downward longwave radiation counteracts the upward longwave radiation with a much smaller impact on the interannual variability of net radiation. Interestingly, NDVI has a larger positive correlation with the net radiation in autumn, which is supported primarily by the inverse relationship between the surface albedo and NDVI. This process would generate positive feedback in a warming situation, where more vegetation results in lower albedo and more net radiation, accelerating warming. Alternatively, the increased vegetation cover can also change upward longwave radiation and could result in a negative correlation with net radiation. Such feedback is less pronounced than the albedo effect in autumn, but it can offer a possible explanation for the lack of significant correlation in summer and spring. Furthermore, it is worth to noting that other links exist between the net radiation and NDVI, such as the photosynthetic active radiation that is an important factor in the photosynthetic activity of vegetation, and the capability of vegetation to regulate the partition of net radiation into sensible heat flux and latent heat flux that is related to vegetation growth. Therefore, the correlation between NDVI and the net radiation indeed reflects the fact that vegetation interacts with the energy cycles [*Wang et al.*, 2007].

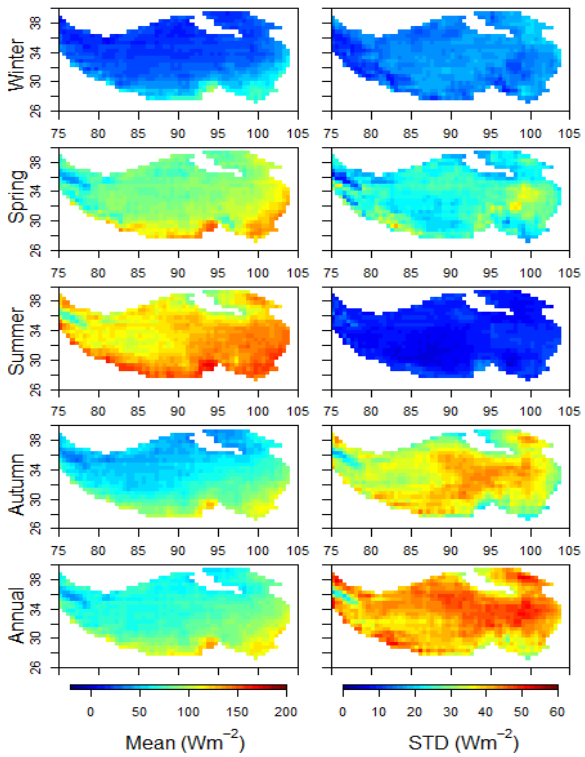

Figure 2-15 Spatial distribution of mean and STD of the fused net radiation over the Tibetan Plateau (1984-2007).

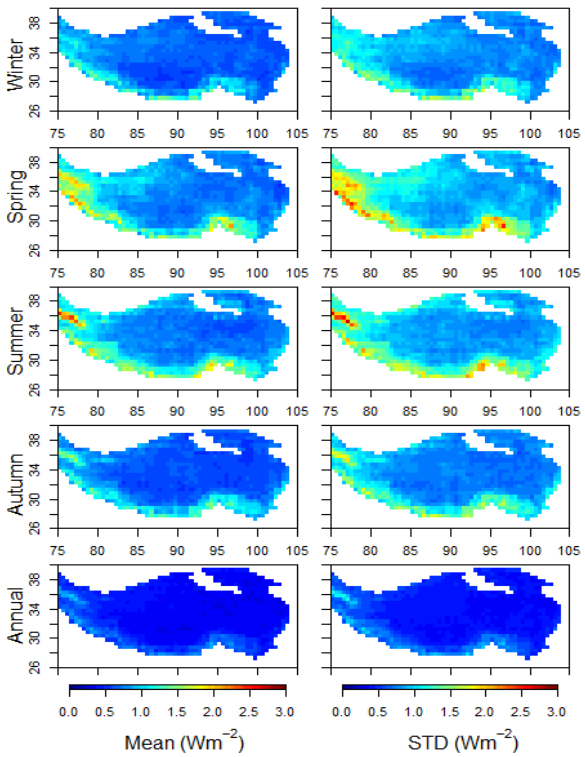

Figure 2-16 Spatial distribution of the uncertainty (2σ) of mean and STD of the fused net radiation over the Tibetan Plateau (1984-2007).

2.4 Conclusions

The spatial distribution and seasonal variability of the 0.5° monthly surface radiation budget from 1984 to 2007 over the Tibetan Plateau have been characterized using a multiple linear regression data fusion scheme with various reanalysis products (CFSR, MERRA, ERA-Interim, JRA-25), remote sensing datasets (GEWEX-SRB, ISCCP-FD), and in situ observations from ground observation networks (AsiaFlux, ChinaFLUX, GAME/Tibet, CAMP/Tibet). The surface radiation budget from the original reanalysis and remote sensing datasets were validated against eleven-year ground measurements (1997–2007). Then, the coefficients and intercepts to calculate the fused downward and upward shortwave and longwave fluxes from six input datasets were generated by using the multiple linear regression model, and the RMSE_CVs of the fused dataset and reanalysis and remote sensing datasets were compared.

The validation results indicate that the RMSE_CVs of the monthly fused downward shortwave irradiance and albedo are 15.1 Wm^{-2} and 0.05, respectively; the RMSE_CVs of the downward and upward longwave fluxes are 13.3 Wm^{-2} and 8.4 Wm^{-2}, respectively; and the RMSE_CV of the all-wave net radiation is as low as 18.9 Wm^{-2}. The low D_R^2 of albedo from reanalysis and remote sensing datasets indicates the need to improve the accuracy of monthly surface albedo over the Tibetan Plateau. Compared to nine sites with long-term observation of downward shortwave irradiance, the fused data represent the decadal variations with higher correlation than using individual products. The uncertainty of the fused surface radiation budget is also discussed, including the error from the input reanalysis and remote sensing datasets, the selection of the data fusion approaches, the effect of elevation adjustment, and the choice of the scale

of the fused data. The advantages of the fused surface radiation budget includes the complete spatial coverage over the Tibetan Plateau over a period of two decades, and the state-of-the-art accuracy (<20 Wm^{-2}) of monthly surface radiation budget components over the Tibetan Plateau, which overcome the overestimation of downward and upward shortwave radiation and albedo in reanalysis datasets, the underestimation of downward shortwave irradiance in remote sensing datasets, and the variations in monthly surface radiation budget biases of existing reanalysis and remote sensing datasets.

The climatology and interannual variability of the five surface radiation budget components—the downward shortwave irradiance, the albedo, the downward longwave flux, the upward longwave flux, and the net radiation— from the fused data are presented and analyzed in conjunction with atmospheric (cloud cover, water vapor) and surface (temperature, snow cover, NDVI) conditions over the Tibetan Plateau. The spatial distributions of the five surface radiation budget components are related to latitude, elevation, land cover, and the monsoon climate over the Tibetan Plateau. In general, the surface radiation budget components exhibit high seasonal mean values in summer and low values in winter, with high STD in spring and autumn, except for the following: 1) the albedo peaks in winter over the Tibetan Plateau, and 2) the downward shortwave irradiance peaks in spring in the southern Tibetan Plateau. The uncertainty of the seasonal and annual mean and STD of the downward/upward shortwave and longwave radiation (net radiation) from the fused data is below 2 Wm^{-2} (3 Wm^{-2}), and the uncertainty of albedo is below 0.001. Over the Tibetan Plateau, cloud cover is negatively (positively) related to the downward shortwave irradiance (the downward longwave radiation), snow cover (NDVI) is positively (negatively) related to albedo, water vapor is positively

related to the downward longwave radiation, and temperature is positively related to the upward longwave radiation. Furthermore, results indicate that the weakening and strengthening of the relationship between the surface radiation budget and the correlated variables of atmospheric or surface conditions exhibit a seasonal dependency over the Tibetan Plateau.

Chapter 3 Characterizing the Surface Energy Budget over the Tibetan Plateau

The surface energy balance over the Tibetan Plateau is essential for the study of land–biosphere–atmosphere interactions, analysis of the changes in terrestrial ecosystems and hydrological systems, and assessment of the impacts of and feedbacks to the climate changes [*Yang et al.*, 2014]. The uncertainty of existing approaches, based on meteorological and satellite observations and models, in characterizing the surface energy balance over the Tibetan Plateau, however, remains large. In particular, projections from the global climate models of the fifth phase of the Coupled Model Intercomparison Project (CMIP5) have been heavily used to assess future climate change, suggesting an urgent need to evaluate the past climate in these CMIP5 models [*Endo and Kitoh*, 2014]. In addition to a cold but wet bias from 1961 to 2005 over the Tibetan Plateau from the CMIP5 models, previous studies have also found an overestimation of the evapotranspiration from 1989 to 1995 over most of the global land surface [*Su et al.*, 2013; *Mueller and Seneviratne*, 2014]. However, the spatial and temporal variations in the surface sensible and latent heat fluxes over the entire Tibetan Plateau as well as its accuracies from the CMIP5 models remain largely unknown.

This chapter first characterizes the spatial and seasonal variability of the surface sensible and latent heat fluxes at 0.5° over the Tibetan Plateau from 1984 to 2007 by synthesizing ground measurements, reanalysis products, and remote sensing products. The surface energy budget from CMIP5 models is then assessed by using the fused data as a reference. Here, I introduce various data sources and methodologies in sections 3.1 and 3.2. Section 3.3 describes the validation results, discusses the uncertainties of the

fused data, investigates the spatial and seasonal variability, and assesses the biases in the surface energy budget from the CMIP5 models. Section 3.4 concludes with major findings and implications derived from the results. Two manuscripts have been prepared based on this chapter; one was published [*Shi and Liang*, 2014] and another one is under review [*Shi and Liang*, 2015a].

3.1 Datasets

To integrate observational and modeling results of the surface energy budget over the Tibetan Plateau, the following three sources data were included (Table 2-1): (1) ground measurement data from AsiaFlux, ChinaFLUX, GAME/Tibet, and CAMP/Tibet; (2) state-of-the-art reanalysis products from the CFSR, MERRA, ERA-Interim, and JRA-25; and (3) two remote sensing-based products: a global evapotranspiration model developed by Zhang et al., [2010], hereafter referred to as Zhang10, and a global evapotranspiration model based on the Global Land Evaporation: the Amsterdam Methodology (GLEAM) [*Miralles et al.*, 2014], hereafter referred to as GLEAM-LE. In addition, outputs from 44 models from CMIP5 [*Taylor et al.*, 2012] were assessed in this study (Table 3-1).

3.1.1 Ground-measured datasets

Between 1997 and 2007, ground surface energy budget measurements from 13 stations were used, and those stations were not used in the development of remote sensing and reanalysis products. The critical information used in station selection for extracting high-quality surface energy budget measurements includes location, measured

variables, measured height, instruments, data period, and number of days (Table 3-2). The ground heat flux is recorded by a soil heat flux plate at a depth below the surface ranging from 0.01 m to 0.1 m with expected accuracy by ±5% of reading for Campbell HFT-3 and EKO MF-81, and -15%~+5% of the 12-hour total for Hukseflux HFP01. The eddy-covariance method measures sensible and latent heat fluxes from high-frequency flux covariance (by 10 Hz) of the wind vector from a three-dimensional sonic anemometer (Campbell CSAT-3, GILL SAT-R3A, and Kaijo DA-600) and the humidity fluctuation from an open-path infrared gas analyzer (LI-COR LI-7500 and Kaijo AH-300), a krypton hygrometer (Campbell KH20), or a thermohygrometer (Vaisala 50Y Bandpass TRH). Based on the manufactory specifications, the estimated accuracy of GILL SAT-R3A is <1% root–mean–square (RMS) of the reading; LI-COR LI-7500, ±2% of the reading; Campbell KH20, ±5% of the reading; and Campbell CSAT-3, ±6% of the horizontal as gain error and ±8.0 cm s^{-1} (±4.0 cm s^{-1}) of horizontal (vertical) offset error. The typical estimated error of the eddy-covariance measurements is 5–20% including 20–50 Wm^{-2} and 10–30 Wm^{-2} for latent heat and sensible heat fluxes, respectively [*Foken*, 2008]. Since the enclosure ratio of the eddy-covariance measurements is approximately 20% [*Foken et al.*, 2006], later a correction is applied to the eddy-covariance measurements in this study (section 3.2.1).

The AsiaFlux site, an alpine meadow grassland in Haibei (HBM), China, offers 15-min averaged surface energy budget measurements, which removes unreliable data by using absolute threshold quality control [*Vickers and Mahrt*, 1997]. The longest measurements of the surface energy budget over the Tibetan Plateau are acquired from two ChinaFLUX sites where surface energy budget is averaged at 30-min intervals after

applying the correction for the density effect to latent heat flux from 2003 to 2007 at the Damxung site (DX) and from November 2002 to 2007 at the Haibei Shrubland site (HBS) [*Webb et al.*, 1980]. 30-min surface energy budget averages were extracted from GAME/Tibet during the intensive observation period in 1998, which included portable automated mesonets at MS3478, planetary boundary layer tower measurements of radiation fluxes and turbulent flux measurements at Amdo and BJ stations, respectively. Six stations (Amdo, ANNI, D105, MS3478, BJ, and Gaize) from CAMP/Tibet measured soil heat flux from 0.2 Hz samples and averages at 10-min intervals. Comprehensive measurements have been taken at the BJ site, including 3-m latent and sensible heat fluxes averaged over 30-min intervals. Heat fluxes from CAMP/Tibet were visually examined for low and high extreme or constant values by using the CAMP Quality Control Web Interface; data with quality flags of good or interpolated were used in this study. Because most sites share the same locations with GAME/Tibet but use different instruments, observations from multiple datasets of the same sites were combined before analysis.

Two datasets based on meteorological station data over the Tibetan Plateau reported by [*Yang et al.*, 2009] and [*Yang et al.*, 2011b], hereafter referred to as Yang09 and Yang11, respectively, were chosen for comparison purposes. Yang09 estimates the daily sensible heat flux of 85 CMA stations over the Tibetan Plateau by using a micro-meteorological method, a physical scheme similar to the eddy-covariance method but which includes statistical downscaled wind speed and ground-air temperature from the CMA stations. The advantage the Yang09 scheme has over conventional methods is that it produces a realistic estimation of the sensible heat flux by accounting for the diurnal

variation of the heat transfer process [*Yang et al.*, 2011a]. Based on the 250-m NDVI from the MODIS vegetation indices product (MOD13Q1), data of 59 CMA stations with elevations >3000 m under the NDVI <0.2 and snow-free conditions were selected by considering the quality flag of MOD13Q1 because of the suitability of the Yang09 scheme for bare soil or spares vegetation land cover. Yang11 provides the simulation results of the surface energy budget of the CMA stations over the Tibetan Plateau by using the SiB2 adjusted land surface model [*Sellers et al.*, 1996] according to the Tibetan Plateau surface characteristics reported from previous experiments [*Yang et al.*, 2008a]. In recent studies, the climatology and trend of sensible heat flux over the Tibetan Plateau extracted from Yang11 have been compared to that from reanalysis datasets, suggesting a general weakened trend of the sensible heat source over the Tibetan Plateau in recent decades, with large uncertainties among different datasets [*Liu et al.*, 2012a; *Zhu et al.*, 2012].

Table 3-1 Summary of the 44 CMIP5 models used in this study.

Institution	Model name	Spatial resolution
Commonwealth Scientific and Industrial Research Organization (CSIRO) and Bureau of Meteorology (BOM), Australia	ACCESS1.0	1.88°×1.25°
	ACCESS1.3	1.88°×1.25°
Beijing Climate Center, China Meteorological Administration, China	BCC-CSM1.1	2.81°×2.81°
	BCC-CSM1.1(m)	1.13°×1.13°
College of Global Change and Earth System Science, Beijing Normal University	BNU-ESM	2.81°×2.81°
Canadian Centre for Climate Modelling and Analysis	CanCM4	2.81°×2.81°
	CanESM2	2.81°×2.81°
National Center for Atmospheric Research	CCSM4	1.25°×0.94°
Community Earth System Model Contributors	CESM1(BGC)	1.25°×0.94°
	CESM1(CAM5)	1.25°×0.94°
	CESM1(FASTCHEM)	1.25°×0.94°
	CESM1(WACCM)	2.50°×1.88°
Centro Euro-Mediterraneo per I Cambiamenti Climatici	CMCC-CESM	3.75°×3.75°
	CMCC-CM	0.75°×0.75°
	CMCC-CMS	1.88°×1.88°
Centre National de Recherches Météorologiques / Centre Européen de Recherche et Formation Avancée en Calcul Scientifique	CNRM-CM5	1.41°×1.41°
	CNRM-CM5-2	1.41°×1.41°
Commonwealth Scientific and Industrial Research Organization in collaboration with Queensland Climate Change Centre of Excellence	CSIRO-Mk3.6.0	1.88°×1.88°
LASG, Institute of Atmospheric Physics, Chinese Academy of Sciences and CESS, Tsinghua University	FGOALS-g2	2.81°×2.81°
NOAA Geophysical Fluid Dynamics Laboratory	GFDL-CM3	2.50°×2.00°
	GFDL-ESM2G	2.50°×2.00°
	GFDL-ESM2M	2.50°×2.00°
NASA Goddard Institute for Space Studies	GISS-E2-H	2.50°×2.00°
	GISS-E2-H-CC	2.50°×2.00°
	GISS-E2-R	2.50°×2.00°
	GISS-E2-R-CC	2.50°×2.00°
Met Office Hadley Centre (additional HadGEM2-ES realizations contributed by Instituto Nacional de Pesquisas Espaciais)	HadCM3	3.75°×2.50°
	HadGEM2-CC	1.88°×1.25°
	HadGEM2-ES	1.88°×1.25°
Institute for Numerical Mathematics	INM-CM4	2.00°×1.50°
Institut Pierre-Simon Laplace	IPSL-CM5A-LR	3.75°×1.88°
	IPSL-CM5A-MR	2.50°×1.25°
	IPSL-CM5B-LR	3.75°×1.88°
Atmosphere and Ocean Research Institute (The University of Tokyo), National Institute for Environmental Studies, and Japan Agency for Marine-Earth Science and Technology	MIROC4h	0.56°×0.56°
	MIROC5	1.41°×1.41°
Japan Agency for Marine-Earth Science and Technology, Atmosphere and Ocean Research Institute (The University of Tokyo), and National Institute for Environmental Studies	MIROC-ESM	2.81°×2.81°
	MIROC-ESM-CHEM	2.81°×2.81°
Max-Planck-Institut für Meteorologie (Max Planck Institute for Meteorology)	MPI-ESM-LR	1.88°×1.88°
	MPI-ESM-MR	1.88°×1.88°
	MPI-ESM-P	1.88°×1.88°
Meteorological Research Institute	MRI-CGCM3	1.13°×1.13°
	MRI-ESM1	1.13°×1.13°
Norwegian Climate Centre	NorESM1-M	2.50°×1.88°
	NorESM1-ME	2.50°×1.88°

Table 3-2 Information of the ground observation sites over the Tibetan Plateau with measurement of latent heat flux (LE), sensible heat flux (H), and ground heat flux (G).

Name	Lat (°N)	Lon (°S)	Ele (m)	Measured variable	Height	Instruments	Data period	Date length
					AsiaFlux			
HBM	37.61	101.31	3250	LE, H	2.2 m	Campbell CSAT-3, LI-COR LI-7500	Jul 2002–Dec 2004	519
				G	-0.01 m	Campbell HFT-3		942
					CAMP/Tibet			
Amdo	32.24	91.62	4695	G	-0.10 m	EKO MF-81	Oct 2002–Dec 2004	520
ANNI	31.25	92.17	4480	G	-0.10 m	EKO MF-81	Oct 2002–Dec 2004	328
D105	33.06	91.94	5038	G	-0.10 m	EKO MF-81	Oct 2002–Dec 2004	765
MS3478	31.92	91.71	4619	G	-0.10 m	EKO MF-81	Oct 2002–Dec 2004	820
BJ	31.37	91.90	4509	LE, H	3.00 m	Kaijo DA-600, LI-COR LI-7500	Oct 2002–Dec 2004	51
				G	-0.10 m	EKO MF-81		654
Gaize	32.30	84.05	4416	G	-0.03 m	EKO MS-802, EKO MS-202	Oct 2002–Dec 2004	582
						EKO MF-81		698
					ChinaFLUX			
DX	30.50	91.07	4751	LE, H	2.2 m	Campbell CSAT-3, LI-COR LI-7500	Jun 2003–Dec 2007	1097
				G	-0.05 m	Hukseflux HFP01		597
HBS	37.67	101.33	3400	LE, H	2.2 m	Campbell CSAT-3, LI-COR LI-7500	Dec 2002–Dec 2007	1107
				G	-0.05 m	Hukseflux HFP01		1726
					GAME/Tibet			
Amdo	32.24	91.63	4700	LE, H	2.85m	Kaijo DA-300, Kaijo AH-300	Jan 1998–May 2003	47
				G	-0.10 m	EKO MF-81		1612
MS3478	31.93	91.72	5063	LE, H	2.85m	GILL SAT-R3A , Vaisala 50Y Bandpass TRH	May 1998–Sep 1998	40
				G	-0.01 m	Campbell HFT-3		118
Gaize	32.30	84.05	4420	G	-0.25 m	EKO MF-81	May 1998–Sep 1998	117
BJ	31.37	91.90	4580	LE, H	2.85 m	Campbell CSAT-3, Campbell KH20	May 1998–Sep 1998	30
				G	-0.05 m	Campbell HFT-3		89

3.1.2 Remote sensing datasets

Remote sensing-based estimations of evapotranspiration have been developed to assessed decadal changes of evapotranspiration over the pan-Arctic basin and Alaska [*Zhang et al.*, 2009], which were then applied to the global land surface [*Zhang et al.*, 2010]. Zhang10 estimates evapotranspiration over vegetated areas by a modified Penman–Monteith approach with a biome-specific canopy conductance model parameterized from 34 FLUXNET sites. The major inputs are AVHRR GIMMS NDVI [*Tucker et al.*, 2005], air temperature and water vapor pressure from NRA-1[*Kalnay et al.*, 1996], and shortwave radiation from GEWEX-SRB [*Pinker and Ewing*, 1985; *Pinker and Laszlo*, 1992]. The independent validation over 48 FLUXNET sites including HBM satisfied accuracy at $R^2 = 0.80–0.84$. A recent evaluation of Zhang10 suggests that it outperforms other reanalysis and remote sensing datasets over the upper Yellow River and Yangtze River basins in the Tibetan Plateau [*Xue et al.*, 2013].

Recently, a global land evapotranspiration dataset has been developed by using GLEAM [*Miralles et al.*, 2011a; *Miralles et al.*, 2011b; *Miralles et al.*, 2014]. GLEAM applied a Priestley–Taylor approach to estimate the potential evaporation from observed surface net radiation and air temperature. The actual evapotranspiration is estimated from potential evaporation multiplied by the evaporative stress factor, which is derived from the observed vegetation optical depths (to approximate vegetation water content) and the estimated root zone soil moisture. The difference between the GLEAM evapotranspiration and the FLUXNET observations is within ±20% at most sites. Considering the temporal coverage and the improved accuracy of the daily

evapotranspiration, the dataset from the third experiment (e3) from the Miralles et al. (2014) is used in this study, which uses net radiation from GEWEX-SRB, air temperature from ISCCP [*Rossow and Dueñas*, 2004] merged with ERA-Interim and the Atmospheric Infrared Sounder (AIRS) [*Ferguson and Wood*, 2010], and precipitation from the Climate Prediction Center unified gauge-based analysis [*Chen et al.*, 2008] as major inputs.

3.1.3 Reanalysis datasets

CFSR is the first global reanalysis product to apply a coupled land–atmosphere–ocean–sea ice system [*Saha et al.*, 2010]. The land surface analysis is produced from the NOAH land surface model, which is forced by the output from the atmospheric assimilation in addition to observed precipitation and snow depth [*Ek et al.*, 2003]. This model outperforms the previous NCEP reanalysis datasets with higher spatial resolution (T382, approximately 0.31°) and improved land surface energy and water closures at the monthly scale [*Meng et al.*, 2012]. MERRA incorporates a catchment hydrological model [*Koster and Suarez*, 1996; *Koster et al.*, 2000] and a multi-layer snow model [*Stieglitz et al.*, 2001] that are coupled to the GOES-5 atmospheric GCM. Global assessments suggest an improvement in the hydrological cycles with MERRA [*Rienecker et al.*, 2011]. ERA-Interim is the first reanalysis product to apply the four-dimensional variational data assimilation scheme provided by ECMWF [*Dee et al.*, 2011], which assimilates 2-m air temperature and humidity to correct soil moisture and temperature analyses [*Douville et al.*, 2000]. The Tiled ECMWF Scheme for Surface Exchanges over Land [*Viterbo and Beljaars*, 1995; *Viterbo and Betts*, 1999] and the snow scheme [*Douville et al.*, 1995] are used in the ERA-Interim for modeling land surface processes. A simple biosphere

scheme is used in JRA-25 with observed snow data [*Sellers et al.*, 1986; *Sato et al.*, 1989]. A recent comparison has revealed consistency in the interannual variability and a weakened tendency of surface wind speed and sensible heat flux over the Tibetan Plateau among JRA-25, Yang11, and NRA-1, whereas large interannual variation and inconsistency have been identified for CFSR [*Zhu et al.*, 2012].

3.2 Methodologies

Figure 3-1 illustrates the framework of this chapter. The monthly mean values were first extracted from each input datasets. The fused latent heat and ground heat fluxes are then generated, and the fused sensible heat flux is estimated based on the surface energy balance approach. Next, the accuracy of the fused data is accessed and compared with the calibrated input products. Finally, the fused data were used to quantify the relationship to the selected surface or atmospheric variables as well as the accuracy of the outputs from CMIP5 models. The methodology used in data preprocessing, data fusion, spatiotemporal characterization, and assessment of CMIP5 models is explained in sections 3.2.1–3.2.4.

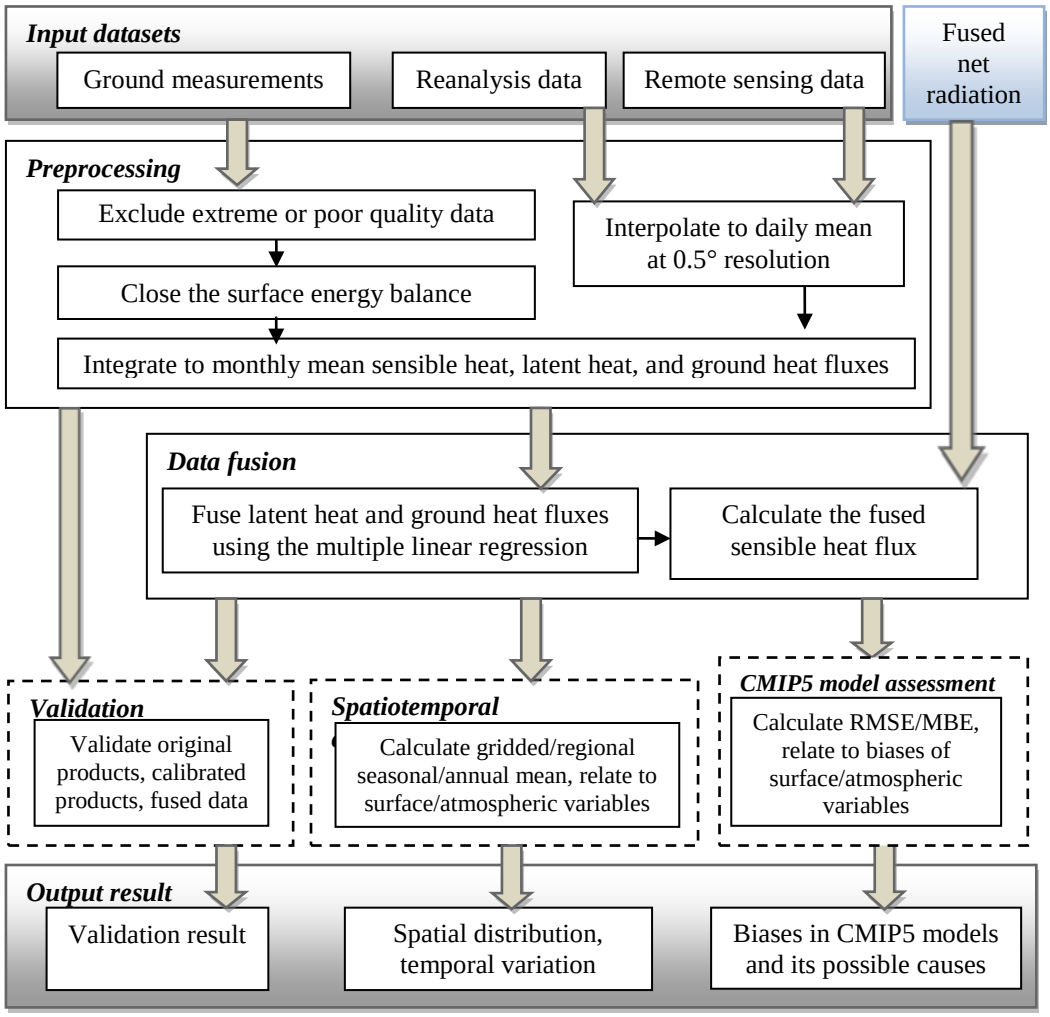

Figure 3-1 Flowchart of the methods for characterizing the surface energy budget over the Tibetan Plateau.

3.2.1 Preprocessing

The monthly surface radiation budget components over the Tibetan Plateau were extracted from ground measurements, remote sensing, and reanalysis datasets by using a method similar to that in section 2.2.1. Original ground-measured values of surface sensible heat flux, latent heat flux, and ground heat flux were integrated to daily hourly mean by using quality control flags to exclude poor-quality and missing data and by corresponding thresholds of -200–400 Wm^{-2}, -200–500 Wm^{-2}, and -200–300 Wm^{-2}, respectively. Then, daily mean value was calculated from daily hourly mean values with

less than half missing. The surface energy balance was closed on the daily scale by using a fixed Bowen ratio, which was calculated from daily hourly value with less than half missing data [*Wohlfahrt et al.*, 2009]. Daily average of the surface energy budget components was also extracted from the original reanalysis datasets and interpolated to 0.5° resolution, and the monthly mean value was calculated from the daily mean covering more than 15 days in a month. The interpolation was also applied to Zhang10 monthly data, which converted to latent heat flux by multiplying the latent heat of vaporization (2.451 MJ kg^{-1}). The sensible heat flux of Zhang10 and GLEAM-LE is estimated by calculating the difference between the net radiation from GEWEX surface radiation budget 3.0 and the latent heat flux from those two products, assuming ground heat flux is relative small and negligible [*Jiménez et al.*, 2011].

3.2.2 Data fusion

The multiple linear regression expressed in Equation 2-1 was applied to the latent heat flux and ground heat flux, and the sensible heat flux was computed using Equation 1-2 with the fused net radiation (from Chapter 2), the fused latent heat flux, and the fused ground heat flux. Similar to the significant large interannual variation of the sensible heat flux from CFSR over the Tibetan Plateau [*Zhu et al.*, 2012], the latent heat flux from CFSR was excluded in the data fusion of the latent heat flux because it exhibits significant large interannual variation. In addition to the ground observations, MERRA, ERA-Interim, JRA-25, Zhang10, and GLEAM-LE were the input datasets for the data fusion of the latent heat flux. This method was also applied to fuse the latent heat flux with those inputs except Zhang10 in the case of missing data from Zhang10. For the

ground heat flux, three reanalysis datasets (i.e., CFSR, MERRA, JRA-25) and the ground observations were the inputs for the data fusion. To ensure energy closure, only the stations with all surface energy budget component measurements were used in the data fusion of the latent heat flux. Additional experiments were performed by applying the multiple linear regression to fuse the sensible heat flux directly from multiple datasets (ground observations, reanalysis and remote sensing datasets) for comparison with the proposed surface energy balance approach. Similar to that of surface radiation budget, each input products were validated by using RMSE, MBE, and R^2, and the fused surface energy budget by RMSE_CV.

3.2.3 Spatiotemporal characterizations

The spatial pattern of the seasonal and annual average and STD of the latent and sensible heat fluxes over the Tibetan Plateau were analyzed, and the uncertainties of the mean and STD were assessed by using the Monte Carlo simulation method as described in section 2.2.3. The seasonal and annual variability from the average latent and sensible heat flux anomalies over the Tibetan Plateau was compared to the selected indicators of atmospheric and surface conditions as well as the fused surface radiation budget anomalies from Chapter 2, the relationships of which were quantified by using the Pearson correlation coefficient. The selected variables included CRU TS3.1 cloud cover and temperature [*Harris et al.*, 2014], Rutgers snow cover [*Robinson et al.*, 1993], AVHRR GIMMS NDVI [*Tucker et al.*, 2005], and MERRA water vapor.

3.2.4 Assessment of CMIP5 models

To assess the net radiation, sensible heat flux, and latent heat flux from the CMIP5 models at the monthly scale, the fused data were selected as a reference dataset. The study period chosen was from 1984 to 2005, based on the overlapping time between the fused data and the CMIP5's historical experiments. To facilitate the comparison, the monthly data from the CMIP5 models were interpolated to a 0.5° resolution using the nearest grid data, and the seasonal cycle were computed as the monthly area-weighted average over the Tibetan Plateau. The absolute and relative RMSE and MBE were used to assess the accuracy of the monthly CMIP5 model outputs based on the fused data. The relative RMSE (or MBE) was calculated as the ratio of RMSE (or MBE) to the average of the fused data. To explore the potential causes of the biases in the surface energy budget components, biases in temperature, water vapor, and cloud cover were also computed based on CRU TS3.1 [*Harris et al.*, 2014], and MERRA water vapor [*Rienecker et al.*, 2011].

3.3 Results and discussions

3.3.1 Validation results

The number of the monthly ground-measured sensible heat, latent heat, and ground heat fluxes for validation is summarized in Table 3-3. The validation results of CFSR, MERRA, ERA-Interim, JRA-25, and Zhang10 are shown in Table 3-4. The latent heat flux from all four reanalysis products had significantly higher R^2 (>0.8) than those of sensible heat flux. CFSR underestimated sensible and latent heat fluxes by -4.9 Wm^{-2} and

-13.1Wm^{-2}, respectively, and overestimated ground heat flux by 6.6 Wm^{-2}. The RMSE of the latent heat flux from CFSR was the largest among all datasets. MERRA and JRA-25 overestimated the latent heat flux with RMSE by 15 Wm^{-2}. MERRA (JRA-25) exhibited the lowest R^2 (largest RMSE) in the sensible heat flux of all reanalysis datasets. Latent and sensible heat fluxes from the ERA-Interim at 11.5 Wm^{-2} and 20.5 Wm^{-2}, respectively were the most accurate among other products with the lowest RMSE. Zhang10 (GLEAM-LE) had a high R^2 by 0.89 (0.90) but showed underestimation of -12.0 Wm^{-2} (-4.1 Wm^{-2}) of the latent heat flux.

Table 3-3 Number of available ground measurement of surface energy budget in each month.

	Jan	Feb	Mar	Apr	May	Jun	Jul	Aug	Sep	Oct	Nov	Dec
Sensible heat flux	5	8	6	5	6	6	6	5	7	5	10	12
Latent heat flux	5	8	6	5	6	6	6	5	7	5	10	12
Ground heat flux	25	22	22	23	26	28	29	29	26	29	31	30

Table 3-4 Validation results of the surface energy budget components of reanalysis and remote sensing datasets by comparing with in situ observation.

		CFSR	MERRA	ERA-Interim	JRA-25	Zhang10	GLEAM-LE
Sensible heat flux	RMSE (Wm^{-2})	22.0	28.7	20.5	29.9	-	-
	MBE (Wm^{-2})	-4.9	4.4	-11.8	-14.5	-	-
	R^2	0.32	0.12	0.28	0.23	-	-
Latent heat flux	RMSE (Wm^{-2})	23.8	15.4	11.5	15.0	22.1	12.6
	MBE (Wm^{-2})	-13.1	8.5	-1.7	3.9	-12.0	-4.1
	R^2	0.82	0.87	0.90	0.86	0.89	0.90
Ground heat flux	RMSE (Wm^{-2})	11.9	6.3	10.4	8.5	-	
	MBE (Wm^{-2})	6.6	-1.8	0.1	-0.5	-	
	R^2	0.73	0.78	0.73	0.82	-	

The coefficients and intercepts used to calculate the ground heat flux and the fused latent heat flux with and without Zhang10 were derived by using the MLR method (Table 3-5). GLEAM-LE and JRA-25 had the largest coefficient in the latent heat and

ground heat fluxes, respectively. Under the condition such that Zhang10 was missing, ERA-Interim and GLEAM-LE mainly dominated the fused latent heat flux. The fused sensible heat, latent heat, and ground heat fluxes exhibited the lowest RMSE_CVs over those by using individual datasets by 14.3 Wm^{-2}, 10.3 Wm^{-2}, and 2.6 Wm^{-2}, respectively (Table 3-6). The cross-validation results support that no individual reanalysis dataset is supreme in all surface energy budget components and that a synthesized approach that uses the multiple linear regression could be a feasible way for improving accuracy. After using data from all available stations, the plots in Figure 3-2 compared the fused results with the ground measurements, which indicated that the latent heat flux was closer to the 1:1 line than the other two components. The R^2 of the fused sensible heat flux was significantly improved (0.67), which was higher than that of the applying the multiple linear regression to multiple sensible heat flux products directly. The accuracy of the data fusion method is sensitive to the training data, which explains the decreased value of RMSE from RMSE_CV.

An independent validation of the sensible heat flux by using Yang09 also indicated that the fused sensible heat flux had the lowest RMSE, by 15.6 Wm^{-2}, than that by using individual reanalysis or remote sensing dataset, which ranged from 22.1 Wm^{-2} to 26.0 Wm^{-2}. A comparison was performed with other global datasets that were available during the validation period (Table 3-6). The selected datasets include GLDAS-1-CLM, GLDAS-1-MOS, GLDAS-1-NOAH, GLDAS-2-NOAH, NRA-1, NRA-2, and a global land evapotranspiration dataset reported by a Princeton University study by using a revised Penman–Monteith model (PU-LE) [*Mu et al.*, 2007; *Vinukollu et al.*, 2011b]. Overall, the fused sensible and latent heat fluxes outperformed those by using global

datasets in terms of lower RMSE_CVs. Therefore, the fused sensible and latent heat fluxes could be used as a reference data to assess the climatological biases of the surface energy budget from the climate models over the Tibetan Plateau.

Table 3-5 Coefficients and intercept to calculate the fused latent heat flux and ground heat flux (coefficients and intercepts with *p* value<0.05 are in bold).

	Intercept (Wm^{-2})	Coefficients					
		CFSR	MERRA	ERA-Interim	JRA-25	Zhang10	GLEAM-LE
Latent heat flux	**-8.7994**	-	**0.4191**	**0.5345**	0.1961	-	-
	-5.6313	-	**0.2349**	**0.4810**	0.0153	-	**0.4418**
	-6.8247	-	**0.2002**	**0.3627**	0.0599	**0.2762**	**0.3923**
Ground heat flux	**1.4429**	**-0.0732**	**0.1422**	-	**0.3531**	-	

Table 3-6 Comparison of the cross validation results of the surface energy budget from the fused data, other data fusion approaches (MLR: multiple linear regression; stepwise: stepwise regression; lasso: adapted lasso regression; PCA_2: principle analysis regression using first two principle components; PCA_3: principle analysis regression using first three principle components; BMA: Bayesian model averaging; RF: random forest; SVM: supported vector regression), reanalysis, and remote sensing datasets (* denotes results from fusing or calibrating the sensible heat flux from multiple datasets or single dataset).

Products	Sensible heat flux (Wm^{-2})	Sensible heat flux * (Wm^{-2})	Latent heat flux (Wm^{-2})	Ground heat flux (Wm^{-2})
Fusion, MLR	14.3	21.2	10.3	2.6
Fusion, stepwise	15.1	20.5	11.1	2.6
Fusion, lasso	14.3	20.6	11.2	2.6
Fusion, PCA_2	14.8	24.5	8.7	2.6
Fusion, PCA_3	14.4	24.6	9.5	2.6
Fusion, BMA	14.3	21.7	10.0	2.6
Fusion, RF	16.4	22.8	9.0	2.8
Fusion, SVM	15.9	22.5	9.1	2.7
CFSR	22.9	22.7	17.0	11.9
MERRA	25.6	26.6	14.1	6.3
ERA-Interim	30.4	22.9	11.5	10.4
JRA-25	24.8	24.3	14.7	8.5
Zhang10	18.7	20.8	14.7	-
GLEAM-LE	21.3	18.7	13.2	-
GLDAS-1_CLM	27.5	25.8	16.9	8.6
GLDAS-1_MOS	22.4	20.8	13.8	9.4
GLDAS-1_NOAH	34.7	17.3	30.4	5.3
GLDAS-2_NOAH	21.8	16.1	17.0	13.5
NRA-1	74.1	21.0	59.0	21.0
NRA-2	74.0	21.0	48.2	18.9
PU-LE	15.2	16.1	20.1	-

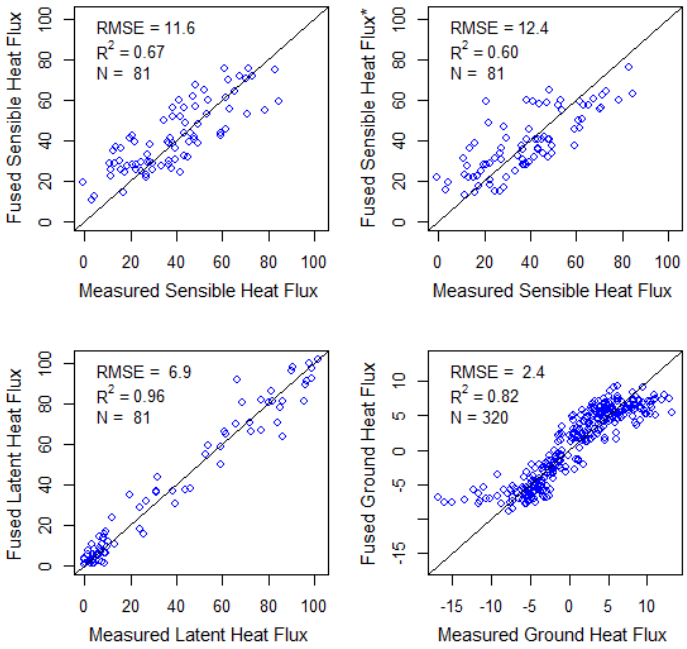

Figure 3-2 Comparisons of the measured and the predicted (fused) sensible heat flux, latent heat flux, and ground heat flux. Result of the estimation of the sensible heat flux form the surface energy balance (upper left) is compared with that of applying multiple linear regression method to fuse multiple sensible heat datasets (upper right, marked with *).

3.3.2 Comparisons of seasonal and interannual variability

The comparison with the ground observations of the monthly cycle averaged over all available stations showed more consistent seasonal cycles of latent heat and the ground heat fluxes than that of the sensible heat flux from reanalysis and remote sensing datasets (Figure 3-3). The ground heat flux from the reanalysis datasets had a positive (negative) bias in spring and summer (winter). MERRA, JRA-25, and Zhang10 overestimated the latent heat flux in winter, which was significantly underestimated by CFSR, Zhang10, and GLEAM-LE by >20 Wm^{-2} from May to September. Although the number of stations is small, the consistent seasonal cycles from remote sensing and reanalysis datasets enhance the confidence for the climatology and monthly accuracy of latent heat flux over the central and eastern Tibetan Plateau. MERRA exhibited large

fluctuation for sensible heat flux in summer and autumn; CFSR and JRA-25 showed a similar pattern but with less value and variability; and Zhang10 and GLEAM-LE (ERA-Interim) had a smooth variation with a peak in May (March). A comparison with the monthly cycles of CMA stations from Yang09 over bare land and sparsely vegetated areas indicates that the fused sensible heat flux was closer to that from Yang09, particularly from January to August. The differences in seasonal variability of the sensible heat flux in autumn and in early winter (when fused sensible heat flux is closer to the value from Zhang10, MERRA, and CFSR) may be related to the changes in samples of CMA stations in autumn to satisfy the bare land or sparsely vegetated conditions in addition to the scale discrepancy between the points and grids which varies as the sample changes.

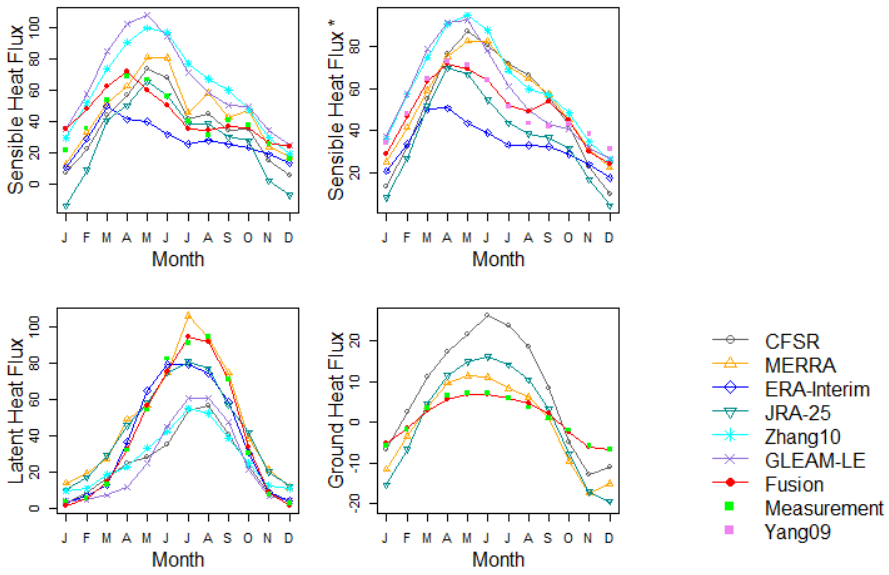

Figure 3-3 Monthly cycles of sensible heat flux, latent heat flux, and ground heat flux from multiple datasets and fused data with ground measurement averaged for all available sites. * denotes the comparison of the monthly cycle of the sensible heat flux at CMA sites with the estimation from Yang09. Units are Wm^{-2}.

The seasonal and annual anomalies of sensible and latent heat fluxes averaged over CMA stations from the fused data were compared with those from reanalysis, remote sensing, and Yang11 datasets (Figures 3-4 and 3-5). Because no direct measurement of the sensible and latent heat fluxes was possible over the CMA stations, the accuracy of the variation and trend from Yang11 could not be validated directly as was only compared with other datasets. Although the interannual variability of the latent heat flux in spring and winter and the sensible heat flux in all seasons except summer from CFSR were larger than those of other datasets, all datasets showed consistent variation of latent heat flux in autumn and sensible heat flux in summer. The season with the weakest Pearson correlation of the sensible and latent heat fluxes between the fused data and Yang11 was spring, when divergences of anomalies among reanalysis, remote sensing, and Yang11 were present. The potential causes of this phenomenon may include the weak correlation of albedo (-0.15) and net radiation (-0.02) between the fused net radiation and Yang11 (result not shown); the large uncertainty in modeling the surface energy budget in spring, as indicated from the wide variety of multiple datasets; and the heterogeneity and physical effects such as soil moisture and albedo from snow cover changes. The annual latent heat flux anomalies from the fused data were also compared with the inferred value by using the water balance method over two river basins over the Tibetan Plateau. The water balance method estimated the annual latent heat flux over the upper Yellow River and the upper Yangtze River basins by subtracting the observed runoff at the Tangnanhai and Zhimenda hydrological stations from the total precipitation sourced from the gauge-based precipitation dataset over East Asia [*Xie et al.*, 2007] , assuming that the change in the terrestrial water storage at the annual scale was negligible

[*Xue et al.*, 2013]. The fused latent heat anomalies agreed with the water balance referred value over the upper Yangtze River basin with the Pearson correlation coefficient by 0.49 (p-value<0.1), while neither the fused data nor the reanalysis or remote sensing datasets was significantly correlated with the latent heat anomalies estimated from the water balance method over the upper Yellow River basin (Figure 3-6). Overall, the fused sensible and latent heat flux anomalies (averaged over CMA stations) were consistent with that from Yang11 and the annual latent heat flux anomalies displayed similar variation with that from the inferred value at the Yangtze River basin in addition to the highest accuracy according to the RMSE_CV (section 4.1), which were used in the spatiotemporal analysis of the sensible and latent heat fluxes (sections 3.3.4 and 3.3.5).

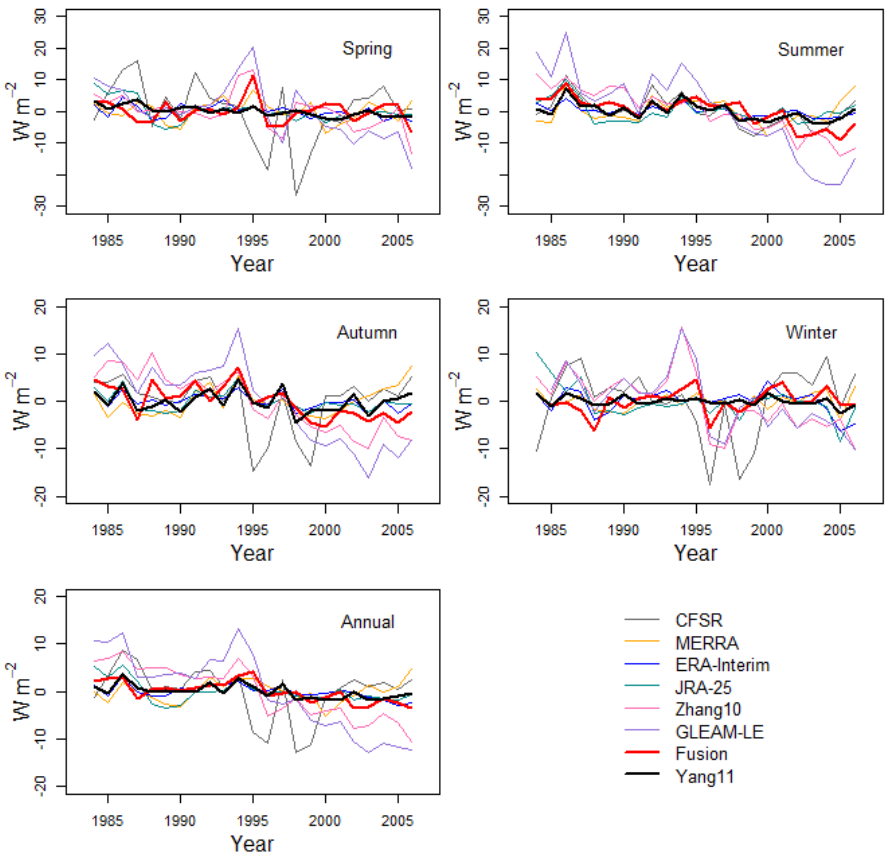

Figure 3-4 Anomalies of sensible heat flux from multiple datasets and fused data with ground measurement averaged for all available CMA stations.

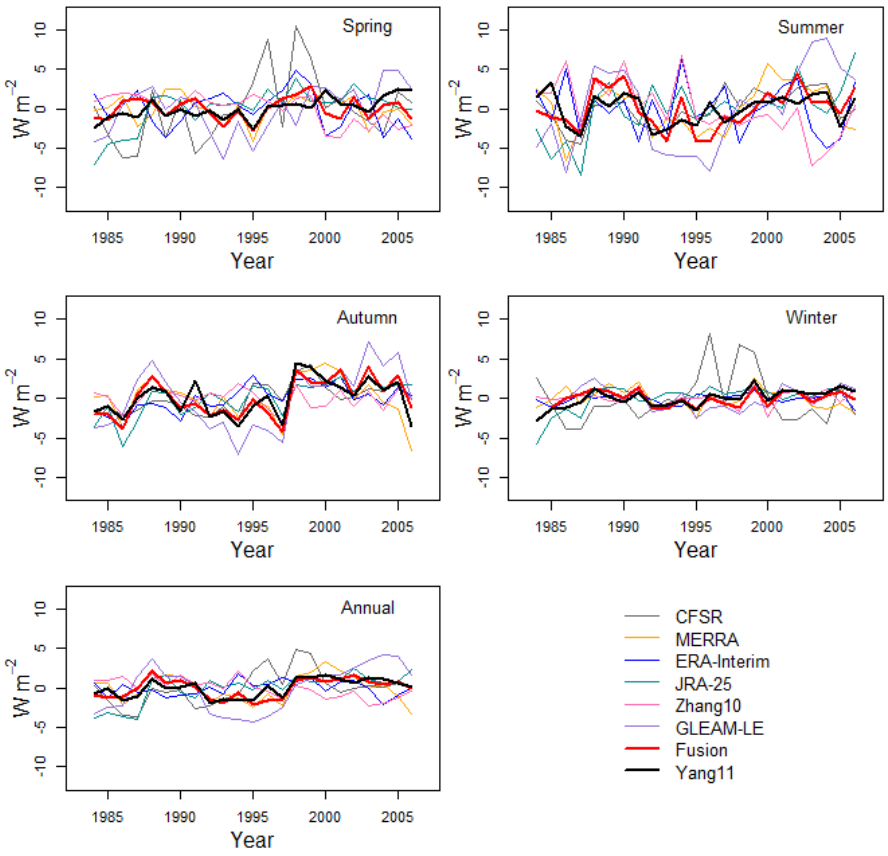

Figure 3-5 Anomalies of latent heat flux from multiple datasets and fused data with ground measurement averaged for all available CMA stations.

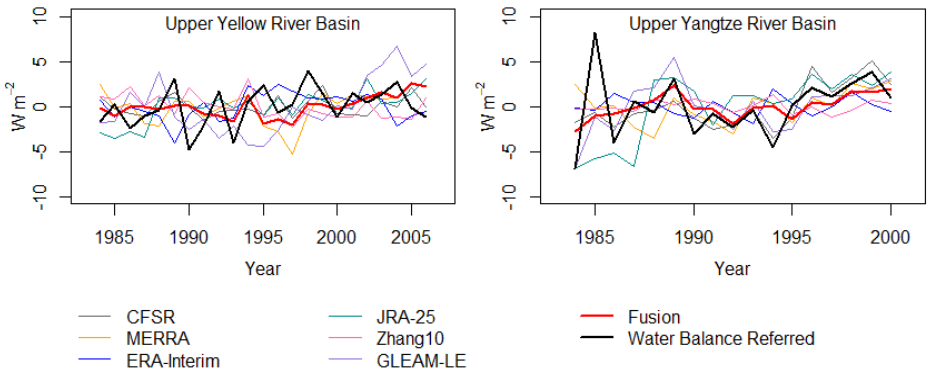

Figure 3-6 Anomalies of the annual basin average latent heat flux from multiple datasets and fused data with the water balance referred value over the upper Yellow River and upper Yangtze River basins.

3.3.3 Uncertainties of the fused surface energy budget

The varied uncertainties from inputs and methods by which the latent and sensible heat fluxes are estimated complicate the quality assessment of the surface energy budget from stations, reanalysis, and remote sensing datasets. Specifically, the input error of the fused surface energy budget is referred to as errors from the monthly value for ground-measured, reanalysis, or remote sensing datasets. The performance of the data fusion is largely affected by the limitations of the ground measurements. First, the uncertainty of the ground-measured sensible and latent heat fluxes can be as large as 20% [*Foken et al.*, 2006]. Second, the Tibetan Plateau is covered by a limited number of sites, especially in the western plateau and the southeastern valley. Third, few stations have continuous observation for multiple years. Previous studies suggest that no single reanalysis dataset is superior to others in terms of routinely measured surface variables such as temperature, precipitation, humidity, pressure, and wind speed and the surface radiation budget, which suggests divergent representation and parameterization of the diurnal cycles of surface variables such as ground–air temperature, wind speed, and aerodynamic roughness in the land surface models used to estimate the surface energy budget [*Wang and Zeng*, 2012; *Zhu et al.*, 2012]. The uncertainty from Zhang10 could be inherited through errors from the AVHRR GIMMS NDVI as inputs and the energy imbalance of eddy covariance measurements as training samples [*Zhang et al.*, 2010]. Additional dominant input error is sourced from net radiation, downward shortwave irradiance, and albedo, which largely determine the available energy to be partitioned into heat fluxes [*Liang et al.*, 2013a]. The validation result also proves that accuracy of the latent heat flux is significantly higher than the sensible heat flux from reanalysis or remote sensing, which is possibly

attributed to the estimation of the latent heat flux is constrained from not only the energy but also water balance over the Tibetan Plateau [*Mueller et al.*, 2013].

The uncertainty of the fused surface energy budget is also affected by error propagation through calculations, including eddy-covariance retrieval, threshold filtering, averaging, interpolation, and data fusion. It is worth noting that eddy-covariance retrieval and the multiple linear regression data fusion employ both multiplication and addition/subtraction, suggesting that uncertainty of the fused surface energy budget could be amplified from those calculations. In addition, the error of the fused data introduced by the resample scale is an emergent issue in the case of integrating synthesis that uses multiple datasets at various spatial resolutions. The impact of the resample scale has been assessed by applying the proposed data fusion method to seven grid sizes including 0.1°, 0.3°, 0.5°, 1.0°, 1.5°, 2.0°, and 2.5° to compare the sensitivity to the resample scale among the fused, reanalysis, and remote sensing datasets (Figure 3-7). The RMSE_CV of the ground heat flux and the sensible heat flux is less variable than that of the latent heat flux among the various scales. In addition, the robustness of fused latent and sensible heat fluxes is supported by lower variation in RMSE_CV with the decreased resample scale than by reanalysis and remote sensing datasets. The magnitude of the changes in RMSE_CV ($\pm$ 2.5 Wm^{-2}) resulting from the various resample scales below 1.5° was less than that from the instrumental errors introduced in section 2.1.

The largest absolute differences in RMSE_CV of latent and sensible heat fluxes between the multiple linear regression and other linear regression models are also relatively low, by 1.6 Wm^{-2} and 2.1 Wm^{-2}, respectively (Table 3-6), comparing with that from the instrumental errors and input errors. The sensible heat flux from the multiple

linear regression also outperformed those from SVM, RF, and BMA. Moreover, the limited accuracy improved by the three advanced models could be attributed to the extreme limited capability of the training stations to approximate true-state statistics. An alternative approach to estimate the sensible heat flux by fusing in situ, reanalysis, and remote sensing datasets directly has a higher RMSE_CV (by 21.2 W m^{-2}) than that by computing it from the surface energy balance.

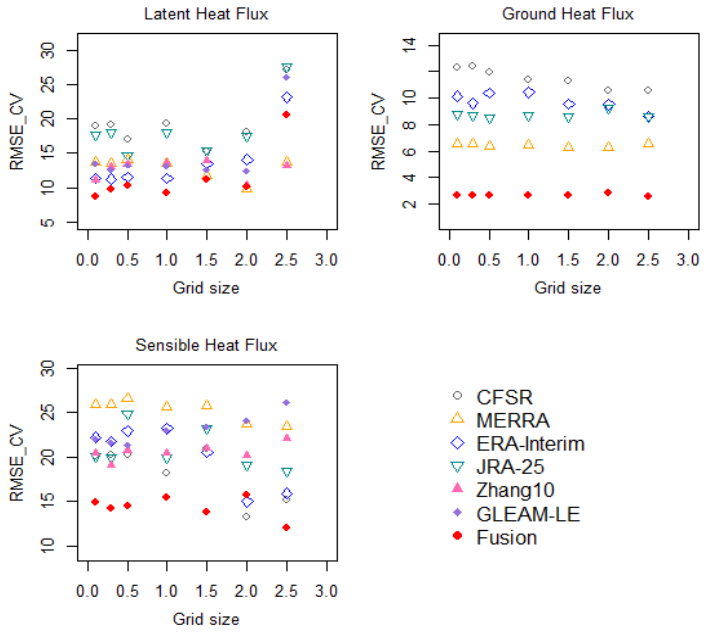

Figure 3-7 Comparisons of the RMSE_CV (Wm^{-2}) of latent heat flux, ground heat flux, and sensible heat flux (H) at multiple grid sizes (°) from original datasets and fused data.

3.3.4 Spatial and seasonal variability of the sensible heat flux

The sensible heat flux was lower in summer than that in spring in the eastern Tibetan Plateau, corresponding to the onset of the summer monsoon, as illustrated in Figure 3-8. The sensible heat flux reached the lowest value in winter and decreased with latitude. In spring, summer, and autumn, the high values were located in the western plateau, the mountain ranges and basins of the western plateau, and the Himalaya ranges

in the south Tibetan Plateau, respectively. The annual STD was high in most dry area, including the northern ranges and basin and in the center of the western plateau. The high STD area formed in the center of the western plateau in summer and moved to the northern ranges in autumn. The southeastern Tibetan Plateau had a low STD in all seasons. The uncertainty of the mean and STD of the sensible heat flux exhibits higher value in spring and summer than other seasons, especially over the west and southern ranges (<3 Wm^{-2}), as shown in Figure 3-9.

The temporal variations of sensible heat flux averaged over the Tibetan Plateau correlated to cloud cover, water vapor, temperature anomalies, snow cover, and net radiative fluxes (Table 3-7). The sensible heat flux anomalies correlated to the variations in the net shortwave or all-wave net radiation in all seasons, with the correlation coefficient reaching the maximum in spring. The negative correlation between cloud cover and sensible heat flux was stronger in summer and winter than that from other seasons, which corresponding to the dominant role of cloud cover in regulating downward shortwave irradiance and net radiation. Positive correlation between the sensible heat flux and water vapor/temperature existed only in spring. In summer, the variability of the sensible heat flux anomalies is negatively correlated to that from water vapor and cloud cover by -0.60 and -0.41, respectively. The correlation between the sensible heat flux and temperature over the Tibetan Plateau suggests two possible physical links: the sensible heat flux mainly warms the surface air in spring as indicated from the positive correlation with mean temperature, and it is suppressed from the weakened temperature gradient in summer and autumn, as suggested from the negative (positive) correlation to mean temperature (temperature range).

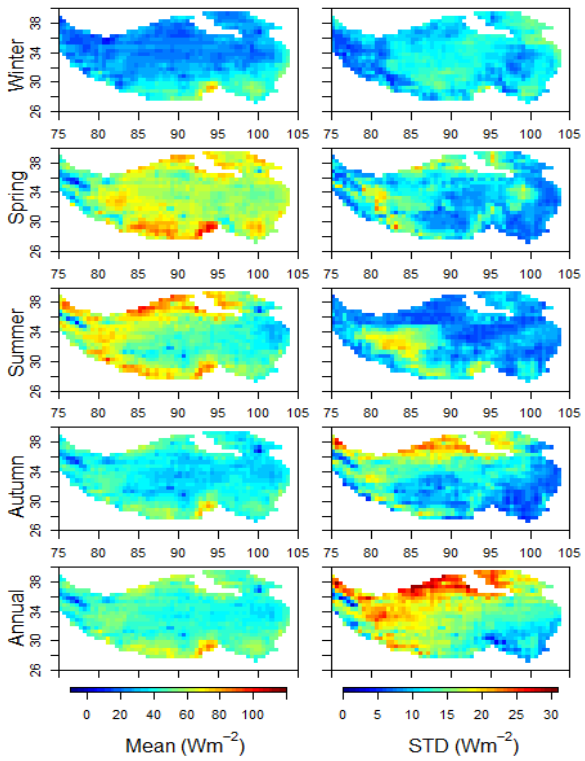

Figure 3-8 Spatial distribution of mean and STD of the fused sensible heat flux over the Tibetan Plateau (1984-2007).

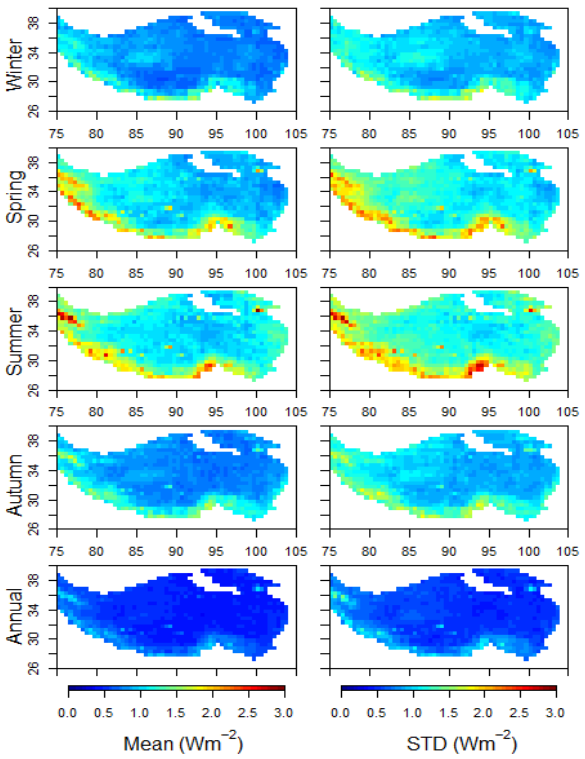

Figure 3-9 Spatial distribution of the uncertainty (2σ) of mean and STD of the fused sensible heat flux over the Tibetan Plateau (1984-2007).

Table 3-7 Correlation coefficients between the annual and seasonal sensible and latent heat flux anomalies from the fused data and surface and atmospheric anomalies over the Tibetan Plateau (p-value <0.1 are in bold).

Correlation coefficient	Annual	Spring	Summer	Autumn	Winter
Sensible heat flux, cloud cover	-0.33	-0.21	**-0.41**	-0.31	**-0.39**
Sensible heat flux, water vapor	**-0.42**	**0.40**	**-0.60**	-0.28	-0.23
Sensible heat flux, GIMMS NDVI	-0.05	-0.19	-0.25	0.33	**0.45**
Sensible heat flux, temperature range	0.29	0.18	**0.68**	**0.59**	0.05
Sensible heat flux, mean temperature	**-0.48**	0.33	**-0.53**	**-0.55**	-0.25
Sensible heat flux, snow cover	-0.16	0.30	0.08	-0.11	0.03
Sensible heat flux, net shortwave radiation	**0.66**	**0.80**	**0.81**	**0.49**	**0.54**
Sensible heat flux, net longwave radiation	-0.04	-0.03	**-0.57**	-0.07	-0.18
Sensible heat flux, net radiation	**0.83**	**0.96**	**0.81**	**0.72**	**0.90**
Latent heat flux, cloud cover	**0.50**	0.33	0.33	**0.34**	**0.39**
Latent heat flux, water vapor	**0.73**	0.16	**0.51**	**0.77**	**0.57**
Latent heat flux, GIMMS NDVI	**0.48**	**0.46**	**0.60**	0.29	0.29
Latent heat flux, temperature range	**-0.52**	-0.21	**-0.38**	**-0.38**	-0.25
Latent heat flux, mean temperature	**0.59**	-0.15	**0.49**	**0.85**	**0.40**
Latent heat flux, maximum temperature	**0.44**	-0.18	0.25	**0.75**	0.27
Latent heat flux, snow cover	**0.36**	0.12	-0.07	-0.06	-0.08
Latent heat flux, net shortwave radiation	-0.28	-0.18	-0.33	-0.07	-0.06
Latent heat flux, net longwave radiation	**0.38**	0.32	**0.45**	0.15	0.06
Latent heat flux, net radiation	0.02	0.00	-0.05	0.09	-0.03

3.3.5 Spatial and seasonal variability of the latent heat flux

The seasonal and annual mean and STD of the fused latent heat flux over the Tibetan Plateau from 1984 to 2007 are shown in Figure 3-10. The latent heat flux increased from northwest to southeast over the Tibetan Plateau in all seasons. In summer, the high mean value area was located in the eastern Tibetan Plateau and in the southwest boundaries. STD was high (low) in the center of the western plateau in summer (spring). The annual STD is similar to that in autumn with high and low values in the center eastern and northern ranges of Tibetan Plateau, respectively. The climatology of mean and STD of latent heat flux corresponded to the elevation from the northwestern to

southeastern Tibetan Plateau and to the dry and wet climate in the western and eastern Tibetan Plateau. The uncertainty of the mean and STD is generally below 1.5 W m^{-2} (Figure 3-11).

The interannual variation of the latent heat flux over the Tibetan Plateau has been compared with atmospheric and surface conditions and surface net radiative fluxes that may regulate the latent heat flux [*Wang and Liang*, 2008; *Wang and Dickinson*, 2012]. In summer, autumn and winter, interannual variation of the latent heat flux correlated strongly to that from water vapor, with correlation coefficients of 0.51, 0.77 and 0.57, respectively (Table 3-7). The seasonal variation of latent heat flux was inherited from the NDVI anomalies as input to the Zhang10 with highest R^2 in summer of 0.60, suggesting the importance of vegetation for regulating regional latent heat flux during the growing seasons. The weak correlation between the cloud cover/water vapor and latent heat flux in spring indicates a potential change in the dominant physical mechanism that determines the variation of latent heat flux from other seasons according to such factors as cloud depth or duration, wind speed, solar irradiance, and vegetation conditions. In general, the latent heat flux anomalies are likely most associated with interannual variation of water vapor (except in spring), which is related to the surface water vapor pressure and moisture feedbacks to the atmosphere, whereas the maximum temperature act only as significant factors for latent heat flux anomalies in autumn and at the annual scale, respectively.

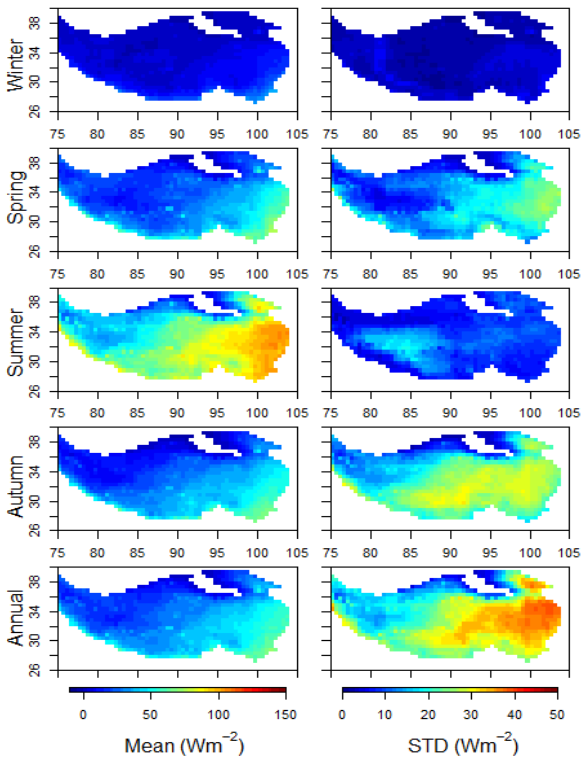

Figure 3-10 Spatial distribution of mean and STD of the fused latent heat flux over the Tibetan Plateau (1984-2007).

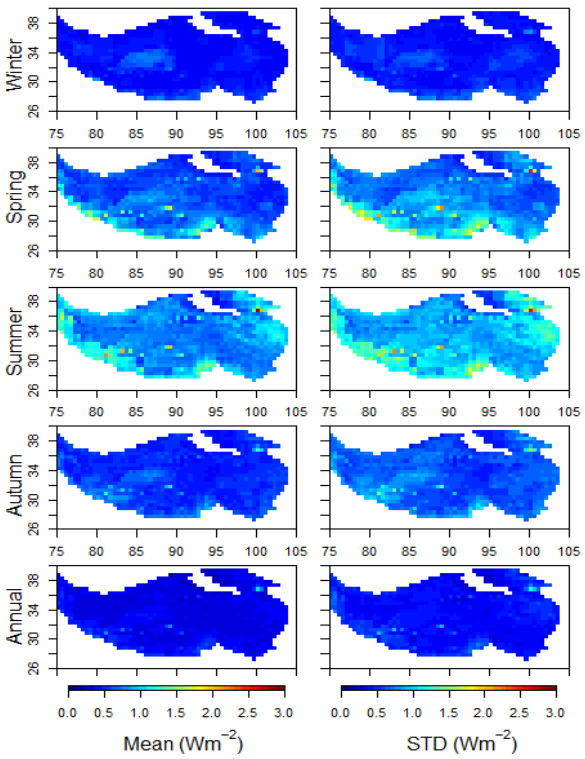

Figure 3-11 Spatial distribution of the uncertainty (2σ) of mean and STD of the fused latent heat flux over the Tibetan Plateau (1984-2007).

3.3.6 Biases of the surface energy budget in CMIP5 models

The net radiation and sensible heat flux displayed negative biases, while the latent heat flux showed a positive bias for most of the CMIP5 models (Figure 3-12). The RMSEs (relative) of the monthly net radiation, sensible heat flux, and latent heat flux from the CMIP5 models were large, with median values of 28.1 Wm^{-2} (35%), 30.8 Wm^{-2} (66%), and 22.4 Wm^{-2} (71%), respectively. All these RMSEs of the three surface energy budget components from most of the CMIP5 models exceeded the RMSEs of the fused data from the leave-one-site-out cross validation. The median MBEs (relative) suggested an underestimation of the net radiation and sensible heat flux by -5.9 Wm^{-2} (-7%) and -14.3 Wm^{-2} (-30%), respectively, but overestimation of latent heat flux with a median MBE of 6.5 Wm^{-2} (35%). Significant positive correlations were found between the sensible and latent heat flux biases and the net radiation biases, supporting the view that the biases in the two heat fluxes could have resulted from the biases in the available energy at the regional scale that is largely determined by the net radiation [*Wild et al.*, 2013; *Mueller and Seneviratne*, 2014]. In addition, the improved RMSEs of the sensible and latent heat fluxes were associated with a higher spatial resolution, with a correlation of 0.38 and 0.35 (p-value <0.1), respectively, between the model grid size and the RMSEs of the sensible and latent heat fluxes.

Consistent annual and seasonal biases in the net radiation, sensible heat flux, and latent heat flux existed in the CMIP5 models for most areas over the Tibetan Plateau, as shown in Figures 3-13 and 3-14. The negative biases in the net radiation were mainly located in the southeastern Tibetan Plateau during all seasons and in the northwestern Tibetan Plateau in winter and spring. The sensible heat flux was underestimated, except

in the central Tibetan Plateau. The positive biases in the latent heat flux dominated the Tibetan Plateau except in summer, and the negative bias existed in the southeastern Tibetan Plateau during all seasons except winter. The magnitude of the relative biases, for most regions, peaked in winter, corresponding to the low value of the three surface energy budget components in winter when the Tibetan Plateau is extremely dry and cold. Compared with the spring and summer climatology from the fused data, the CMIP5 models better represented the spatial pattern of the autumn and winter climatology in terms of the standard deviation and correlation (Figure 3-15). In addition, the inter-annual variability of the three fluxes from the CMIP5 models was compared with that of the fused data in terms of the Pearson correlation and standard deviation of the regional average over the Tibetan Plateau (Figure 3-16). Because the CMIP5 models failed to represent the seasonal anomalies of the three fluxes with low Pearson correlation with the fused data, the following analysis will focus on the seasonal biases and their possible causes.

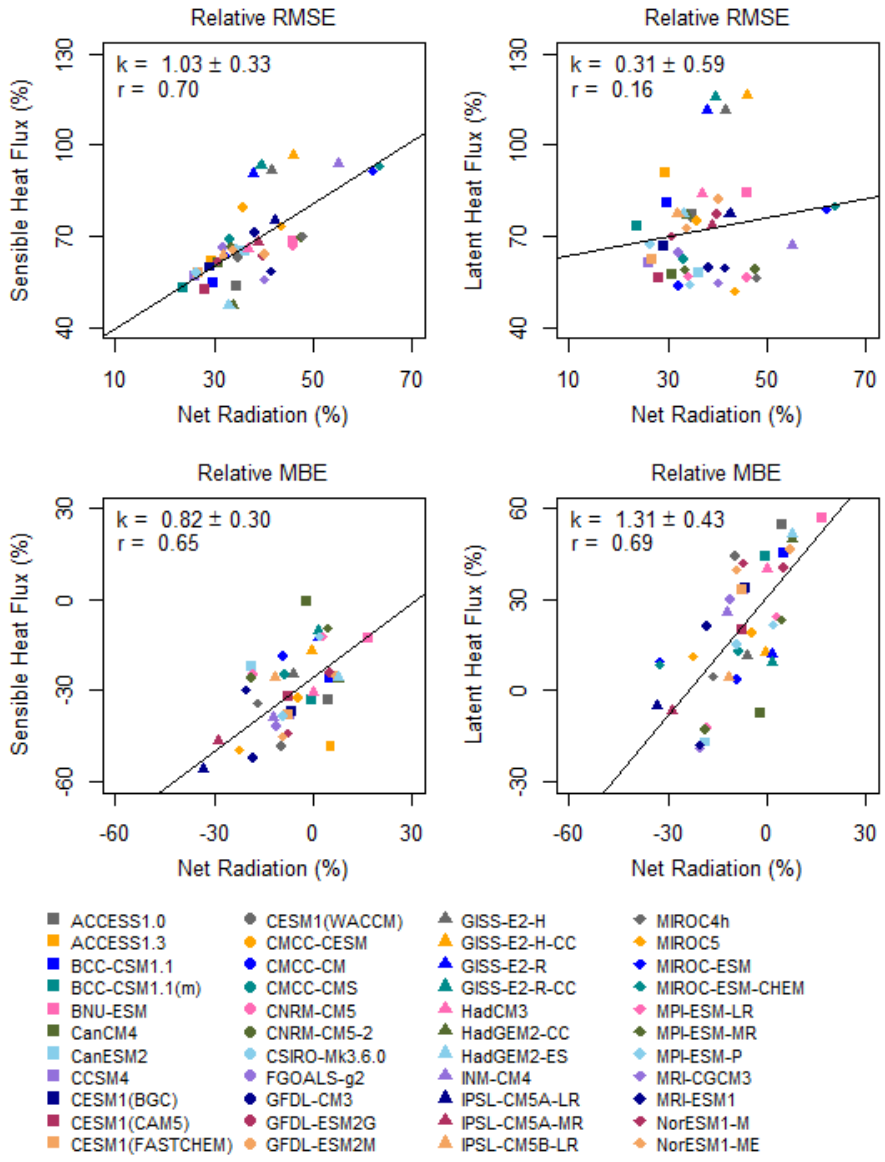

Figure 3-12 Scatterplots of the relative RMSE (or MBE) of the sensible and latent heat fluxes as a function of relative RMSE (or MBE) of the net radiation from the 44 CMIP5 models (k denotes the slope at the 95% confidence interval; r is the Pearson correlation).

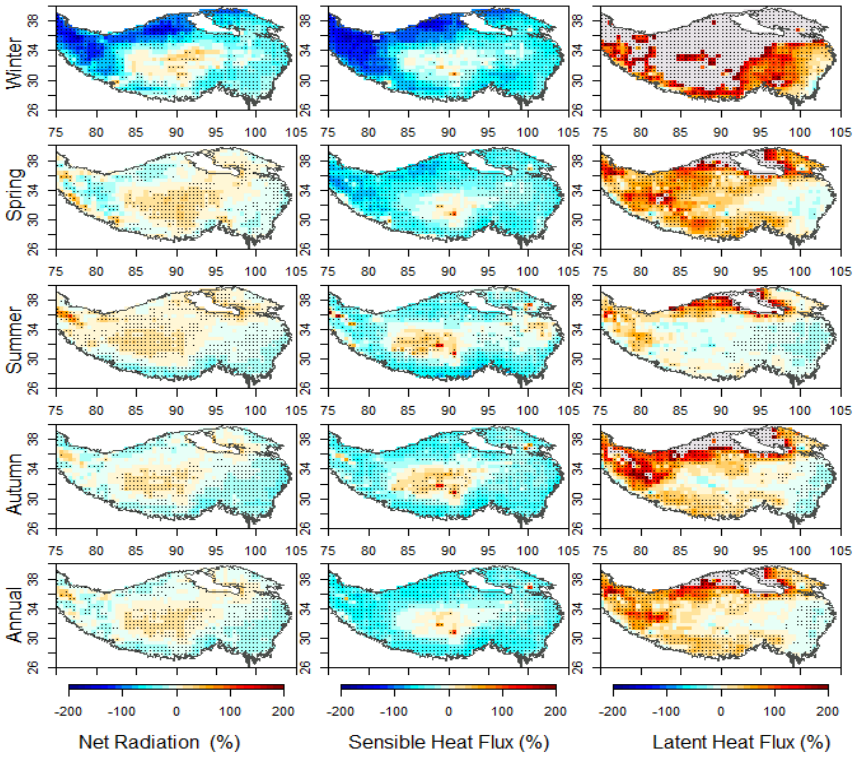

Figure 3-13 Median value of the relative annual and seasonal biases in the net radiation, sensible heat flux, and latent heat flux from the CMIP5 models (dots show that more than 66% of the models (29 out of 44 for CMIP5) agree on the sign of the biases; pixels with relative bias >200% are not shown).

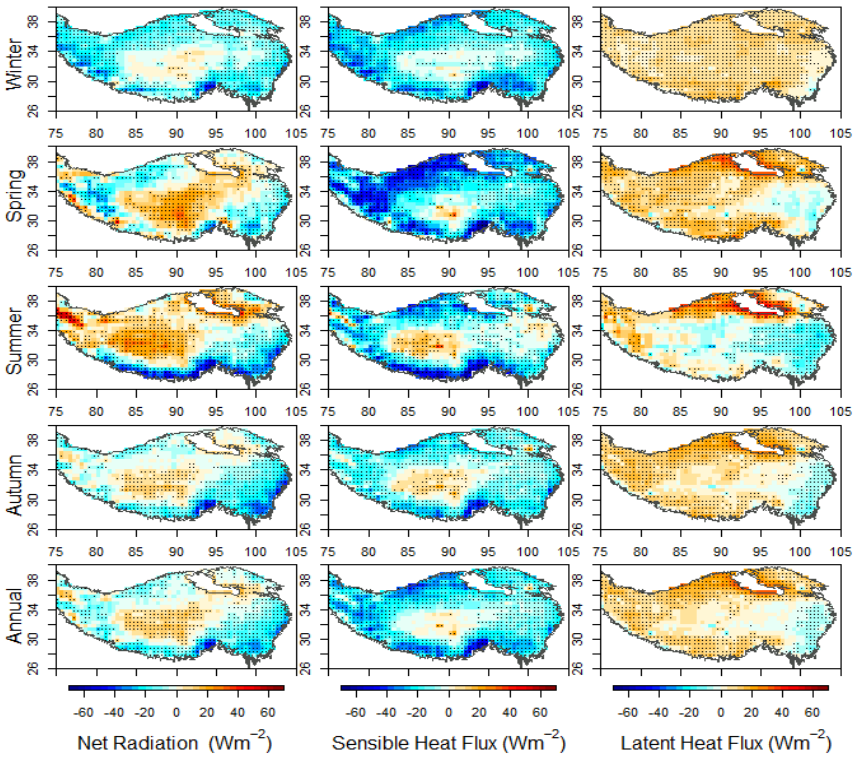

Figure 3-14 Same as figure 3-12, but for the absolute annual and seasonal biases.

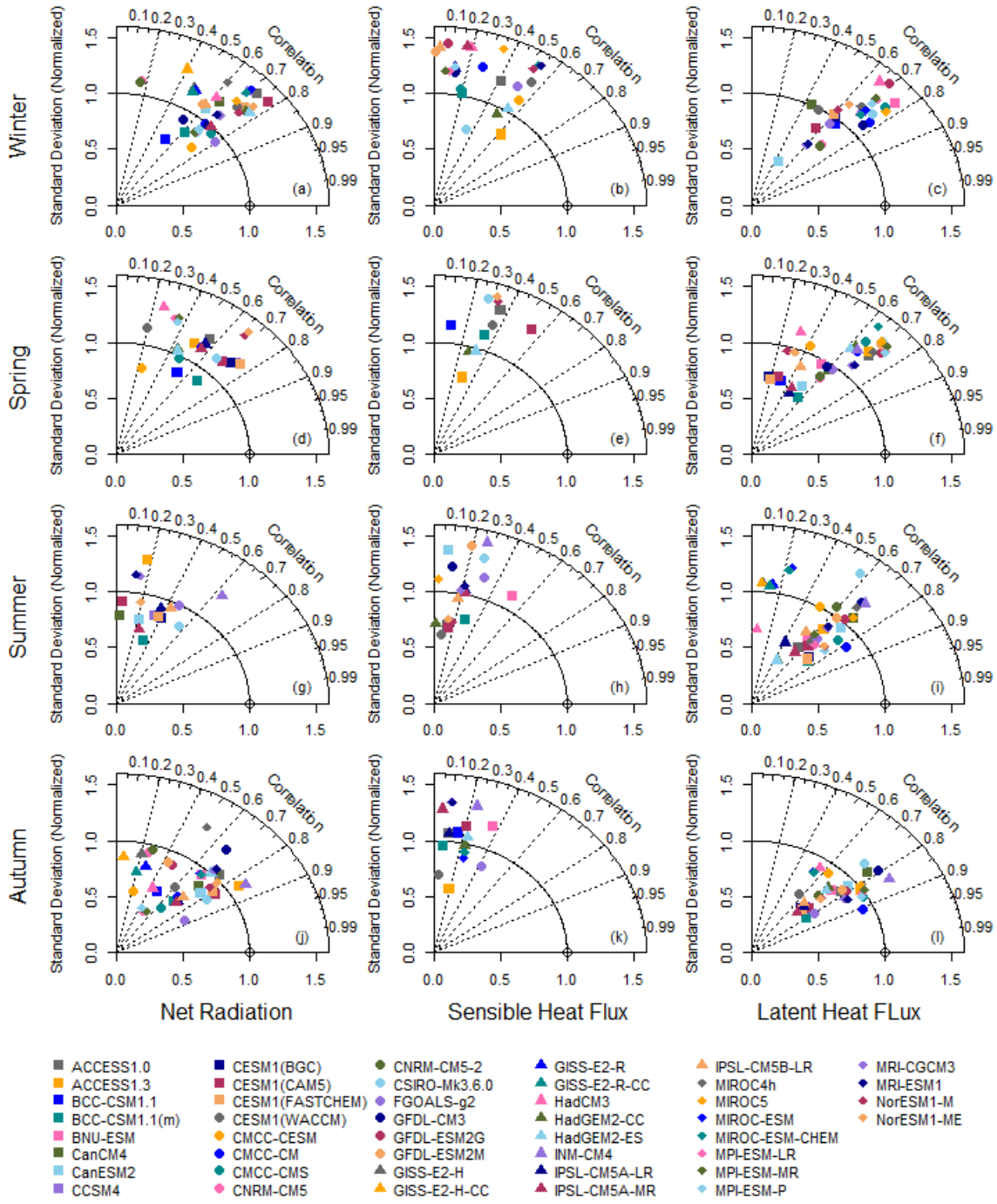

Figure 3-15 Taylor diagram of the seasonal climatology of the net radiation, sensible heat flux, and latent heat flux between the 44 CMIP5 models and the fused data (only models that have positive correlation and standard deviations less than 1.5 are shown).

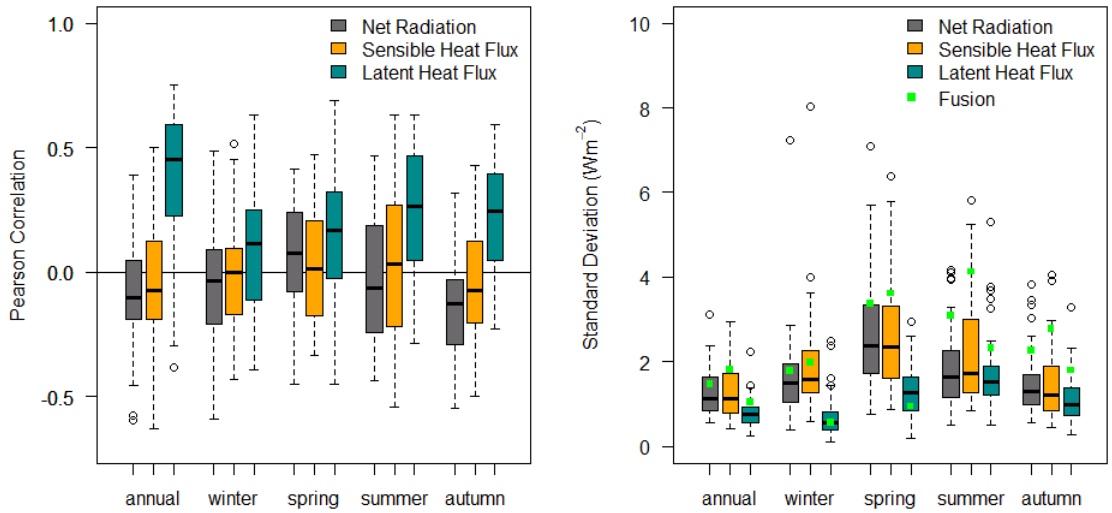

Figure 3-16 Boxplots of the Pearson correlation of the annual and seasonal net radiation, sensible heat flux, and latent heat flux anomalies between the CMIP5 models and the fused data (left) and the comparisons of the standard deviation of the anomalies between the CMIP5 models and the fused data (right).

The seasonal cycle of the net radiation from the CMIP5 models was more consistent with the fused data than the sensible and latent heat fluxes averaged over the Tibetan Plateau (Figure 3-17). The monthly variation of the sensible and latent heat fluxes from the multi-model mean of the CMIP5 models correlated with that from the fused data, but large negative biases existed for the sensible heat flux. In particular, the underestimation of the sensible heat flux exceeded -20 Wm^{-2} for most models for spring. Previous studies suggested that the preceding spring sensible heat flux over the Tibetan Plateau was one of the dominant drivers of the Asian summer monsoon [*Duan et al.*, 2013; *Rajagopalan and Molnar*, 2013]. Therefore, the negative biases of the spring sensible heat flux for most CMIP5 models could cause underestimation of the summer precipitation over East Asia but overestimation of the summer monsoon duration over India [*Sperber et al.*, 2013]. For winter and early spring, biases existed for all three

fluxes, possibly related to the weak representations of surface albedo and land-atmosphere interactions when snow is present in the CMIP5 models [*Qu and Hall*, 2014].

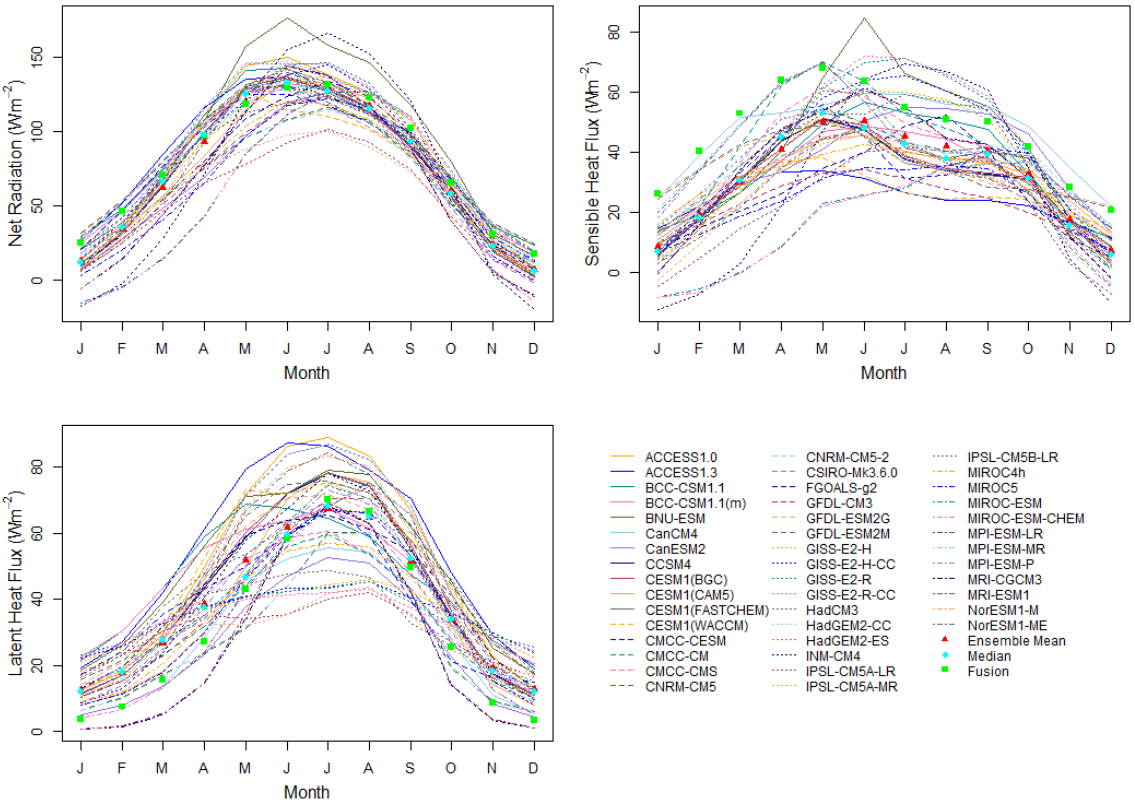

Figure 3-17 Seasonal cycle of the net radiation, sensible heat flux, and latent heat flux from the 44 CMIP5 models and the multi-model mean and median values compared with the fused data.

Over the Tibetan Plateau, significant correlations were identified between the biases in the net radiation, sensible heat flux, and latent heat flux and the biases in cloud cover, water vapor, mean temperature, and temperature range in the four seasons (Table 3-8). The biases in net radiation were positively related to the biases in mean temperature and cloud cover in spring, autumn, and winter, suggesting the dominant role of the longwave effect of clouds (i.e., increasing downward longwave radiation) over the

shortwave effect (i.e., decreasing downward shortwave radiation). Although no significant relationship was found between the biases in the maximum and minimum temperatures and the biases in the three fluxes, the temperature range did relate to them at the seasonal scale. The temperature range was widely used as a proxy with negative relationships with clouds (i.e., cloud cover and cloud duration) and humidity conditions (i.e., soil moisture), which explained its negative correlation to the net radiation in spring and autumn through the dominant role of the cloud longwave effect and the latent heat flux through the profound impact of the soil moisture in all seasons except winter, when the climate over the Tibetan Plateau is extremely dry [*Wang et al.*, 2006; *Wang and Liang*, 2008]. In the summer, the bias in water vapor was another important factor that affected the partition of the available energy into sensible and latent heat fluxes and it was positively (negatively) related to the latent heat flux (sensible heat flux).

Table 3-8 Pearson correlation coefficient between the annual (or seasonal) biases in the net radiation, sensible heat flux, and latent heat flux, and the biases in selected surface and atmospheric variables from the CMIP5 models (p-value <0.05 are in bold).

Variables	Annual	Spring	Summer	Autumn	Winter
Net radiation, cloud cover	**0.52**	**0.55**	0.15	**0.44**	**0.49**
Net radiation, water vapor	0.20	0.26	-0.05	0.24	0.14
Net radiation, mean temperature	**0.54**	**0.73**	0.06	**0.39**	**0.55**
Net radiation, temperature range	**-0.44**	**-0.40**	-0.29	**-0.46**	-0.14
Sensible heat flux, cloud cover	**0.32**	**0.39**	-0.26	0.11	0.28
Sensible heat flux, water vapor	0.00	0.15	**-0.31**	-0.13	0.01
Sensible heat flux, mean temperature	**0.31**	**0.57**	-0.18	0.09	**0.37**
Sensible heat flux, temperature range	-0.01	-0.10	**0.39**	0.10	-0.25
Latent heat flux, cloud cover	**0.33**	**0.37**	**0.39**	**0.41**	**0.67**
Latent heat flux, water vapor	0.28	0.24	**0.45**	0.29	0.18
Latent heat flux, mean temperature	**0.40**	**0.43**	**0.43**	**0.37**	**0.69**
Latent heat flux, temperature range	**-0.51**	**-0.36**	**-0.65**	**-0.55**	-0.08

3.4 Conclusions

The spatial and seasonal variability of the surface sensible and latent heat fluxes over the Tibetan Plateau from 1984 to 2007 were presented by using the fused monthly latent and sensible heat fluxes at 0.5° from ground-measured datasets including AsiaFlux, ChinaFLUX, GAME/Tibet, and CAMP/Tibet; remote sensing datasets from Zhang10 and GLEAM-LE; and reanalysis datasets including CFSR, MERRA, ERA-Interim, and JRA-25. In additions, the monthly net radiation, sensible heat flux, and latent heat flux from 44 CMIP5 models was assessed based the fused surface energy budget.

The surface sensible and latent heat fluxes from reanalysis and remote sensing datasets were first validated against those from ground measurement at the monthly scale and were then synthesized by using the multiple linear regression approach. The uncertainties of the fused surface sensible and latent heat fluxes were discussed from various aspects in which uncertainties propagating from input errors and instrumental errors were likely the dominant factors when comparing with that from the interpolation scale and the selection of the fusion method. Results from the leave-one-site-out cross-validation suggested that the fused monthly latent and sensible heat fluxes had the lowest RMSE_CVs, at 10.3 Wm^{-2} and 14.3 Wm^{-2}, respectively, against those using each calibrated dataset. The fused sensible heat flux also consistently captured the monthly cycle to the datasets by using only meteorological observations (Yang09).

At the regional scale, the high value of the latent and sensible heat flux was located in the wet area (the eastern Tibetan Plateau and the south face of the southwest ranges) and dry area (the western Tibetan Plateau), respectively. The uncertainty of the

mean and STD of the sensible heat flux (<3 Wm^{-2}) is higher than that of latent heat flux (<1.5 Wm^{-2}). The associations among the fused sensible and latent heat fluxes and the related surface anomalies such as mean temperature, temperature range, snow cover, and NDVI in addition to atmospheric anomalies such as cloud cover and water vapor show seasonal dependence, suggest that the land–biosphere–atmosphere interactions over the Tibetan Plateau could display nonuniform feedbacks to the climate changes.

There is an urgent need to address the existing systematic biases in the surface energy budget components in CMIP5 models over the Tibetan Plateau because of the large RMSEs with the median value exceeding 20 Wm^{-2} and the existence of underestimations (overestimations) of net radiation and sensible heat flux (latent heat flux) with median MBEs at -7% and -30% (35%). Significant negative biases in the sensible heat flux were found for every month, as well as an overestimation (underestimation) of the latent heat flux (net radiation) in the winter and early spring. Furthermore, the biases of the downward longwave radiation and soil moisture are postulated to be the dominant factors causing the seasonal biases of the surface energy budget components over the Tibetan Plateau.

Chapter 4 Impact of the Spring Sensible Heat Flux over the Tibetan Plateau on the Asian Summer Monsoon Rainfall

Changes in the sensible heat flux over the Tibetan Plateau have a substantial relationship with the formation and strength of the Asian monsoon [*Wang et al.*, 2008c; *Turner and Annamalai*, 2012; *Wu et al.*, 2012a]. To explain the effect of the elevated heating over the Tibetan Plateau, the concept of a "sensible-heat driven air-pump" has been proposed [*Wu et al.*, 2007]. This concept has been supported by modeling studies wherein surface heating over the Tibetan Plateau causes an air column to center and ascend, regulating the Asian summer monsoon rainfall [*Wang et al.*, 2008c; *Duan et al.*, 2013]. However, the relationship between the spring sensible heat anomalies over the entire Tibetan Plateau and the Asian summer monsoon rainfall over the past two decades remains largely unknown.

Using observational and reanalysis data set, the impact of the spring sensible heat anomalies over the Tibetan Plateau on the Asian summer monsoon rainfall is assessed in this chapter. Specifically, this study aims address the following issues: first, it aims identify the variability in the spring sensible heat flux anomalies over the Tibetan Plateau, and how this variability is associated with the surface and atmospheric conditions over the Tibetan Plateau. Secondly, the study aims to ascertain whether the preceding spring sensible heat anomalies and the atmospheric heat source over the Tibetan Plateau persist throughout the following summer; and thirdly, whether the spring sensible heat anomalies over the Tibetan Plateau are significantly related with the Asian summer monsoon rainfall, and how this relationship varies in the early, peak, and late monsoon seasons. Finally, the study also aims to discuss the possible physical mechanisms of the

association between the spring sensible heat anomalies over the Tibetan Plateau and the Asian summer monsoon rainfall.

Here, I will describe the data sources, circulation and precipitation indices, and statistical methods in section 4.1, present the results and discussions in section 4.2, and summarize conclusions in section 4.3. A manuscript about the work in this chapter have been submitted [*Shi and Liang*, 2015b].

4.1 Data and methods

4.1.1 Data and study region

The surface sensible heat flux over the Tibetan Plateau is sourced from the fused surface energy budget data as described in Chapter 3. Four global precipitation datasets were analyzed (Table 4-1): the satellite-gauge precipitation rate from the Global Precipitation Climatology Project (GPCP) version 2.2 combined precipitation data set [*Adler et al.*, 2003; *Huffman et al.*, 2009]; the standard averaged precipitation rate from the Climate Prediction Center Merged Analysis of Precipitation (CMAP) [*Xie and Arkin*, 1997]; the gridded-gauge land-surface precipitation from the Global Precipitation Climatology Centre (GPCC) version 6 full data reanalysis [*Schneider et al.*, 2011]; and the interpolated-gauge precipitation analysis from the National Oceanic and Atmospheric Administration (NOAA) Precipitation Reconstruction over Land (PREC/L) [*Chen et al.*, 2002]. Daily gridded precipitation datasets over the Asian Monsoon region were also used, as derived from the Asian Precipitation—Highly Resolved Observational Data Integration Towards Evaluation of Water Resources project (APHRODITE) [*Yatagai et al.*, 2012], and the all-India gridded daily rainfall data from the India Meteorological

Department (IMD) [*Rajeevan et al.*, 2006]. The use of multiple precipitation datasets over the Asian monsoon regions ensured that analyzed precipitation patterns over the Asian monsoon area were data independent. The average rainfall in the early, peak, and late monsoon seasons was investigated by using the daily rainfall from APHRODITE and pentad (5-day period) rainfall from GPCP and CMAP. Three sub-seasons were defined for three regions, including the Indian summer monsoon region, the area south of 32.5 °N, and the area north of 32.5 °N (Table 4-2). These periods cover most of the observed onset (starting from June) and the withdrawal pentads over the Asian summer monsoon region [*Wang and LinHo*, 2002; *Kajikawa et al.*, 2012; *Rajagopalan and Molnar*, 2014].

Table 4-1 Summary of datasets used for characterize the Asian summer monsoon.

Name	Variable	Spatial resolution	Temporal resolution	Temporal coverage
GPCP	Precipitation	2.5° × 2.5°	Monthly, pentad	01/1979–12/2013
CMAP	Precipitation	2.5° × 2.5°	Monthly, pentad	01/1979–11/2011
GPCC	Precipitation	0.5° × 0.5°	Monthly	01/1901–12/2010
PREC/L	Precipitation	0.5° × 0.5°	Monthly	01/1948–04/2014
APHRODITE	Precipitation	0.5° × 0.5°	Daily	01/1951–12/2007
IMD	Precipitation	1.0° × 1.0°	Daily	01/1951–12/2010
ERA-Interim	Wind, water vapor transport, temperature, specific humidity	T255(80 km)	3 hourly	01/1979–01/2014
GEWEX-SRB	Top of atmosphere net radiation	1.0° × 1.0°	3 hourly	07/1983–12/2007
ISCCP-FD	Top of atmosphere net radiation	2.5° × 2.5°	3 hourly	07/1983–12/2009
NOAA OLR	Outgoing longwave radiation	2.5° × 2.5°	Monthly	06/1974–12/2013
ERSST	Sea surface temperature	2.0° × 2.0°	Monthly	01/1854–03/2014

Table 4-2 Definition of the three sub-seasons in this study.

Region	Early monsoon season	Peak monsoon season	Late monsoon season
The Indian summer monsoon region	Pentads 31–34	Pentads 35–49	Pentads 50–59
The area south of 32.5 °N	Pentads 31–34	Pentads 35–36	Pentads 37–43
The area north of 32.5 °N	Pentads 35–39	Pentads 40–42	Pentads 43–49

To explain the variability in the spring sensible heat flux over the Tibetan Plateau, the following variables were also analyzed: the surface radiation budget, the surface (snow cover, temperature, NDVI, moist static energy) and atmospheric conditions (water vapor, cloud cover, atmospheric heat source), the moist static energy, and the atmospheric heat source. The surface radiation budget was sourced from the fused data in Chapter 2, the observed monthly mean cloud cover, daily temperature, and daily temperature range from the CRU TS3.1 [*Harris et al.*, 2014], the observed monthly snow cover from the Rutgers snow cover datasets [*Robinson et al.*, 1993], water vapor from MERRA [*Rienecker et al.*, 2011], and the observed monthly NDVI from AVHRR GIMMS NDVI [*Tucker et al.*, 2005]. The moist static energy (*MSE*) at the surface was calculated as in Equation 4-1 using the air temperature (*T*) and specific humidity (*q*) from ERA-Interim, which was chosen because of its proficient performance in representing air temperature and specific humidity in comparison with other reanalysis data sets over the Tibetan Plateau [*Dee et al.*, 2011; *Wang and Zeng*, 2012].

$$MSE = C_p T + L_v q + gZ \qquad \textbf{Equation 4-1}$$

where C_p is the specific heat at constant pressure of water (J kg^{-1} $^oC^{-1}$), L_v the latent heat of vaporization (J kg^{-1}), g is gravity, and Z is height. To demonstrate the contribution of spring sensible heating to the observed atmospheric heat source over the Tibetan Plateau, the atmospheric heat source (Q) was estimated in Equation 4-2 based on the following: the surface sensible heat flux (H) and the surface net radiation (NR_{srf}) from Chapter 3 and Chapter 2, respectively; the net radiation at the top of atmosphere (NR_{toa}) as the averaged value from GEWEX-SRB and ISCCP-FD; and the precipitation rate (P, m s^{-1}) from GPCP.

$$Q = H + L_v \rho_w P + NR_{toa} - NR_{srf} \quad \textbf{Equation 4-2}$$

where ρ_w is the density of water (kg m^{-3}).

The following datasets were used to analyze the variability of the Asian summer monsoon: 1) the monthly SST from the NOAA Extended Reconstructed SST version 3 (ERSST) [*Smith et al.*, 2008], 2) the monthly winds and integrated water vapor transport from ERA-Interim reanalysis [*Dee et al.*, 2011], and 3) the monthly outgoing longwave radiation (OLR) from NOAA interpolated outgoing longwave radiation datasets [*Liebmann and Smith*, 1996]. The ERSST and OLR were not used in any input reanalysis datasets or in the computation of the fused sensible heat flux over the Tibetan Plateau, and the choice of ERA-Interim ensured consistency with the fused sensible heat flux. The study period was confined to the period 1984 to 2007, during which all these datasets were available, and anomalies were calculated as the deviation from the 24-year average.

As shown in Figure 4-1, the Asian monsoon region was defined as areas over land with an annual precipitation range (May to September minus November to March) larger than 2.5 mm day^{-1} by using GPCP precipitation data from 1984 to 2007 [*Wang et al.*, 2011a]. Two sub-systems of the Asian summer monsoon were analyzed in this study: the East Asian summer monsoon and the Indian summer monsoon. The summer was defined as June–July–August in the East Asian summer monsoon, and as June–July–August–September for the Indian summer monsoon [*Wang et al.*, 2008a; *Yim et al.*, 2013].

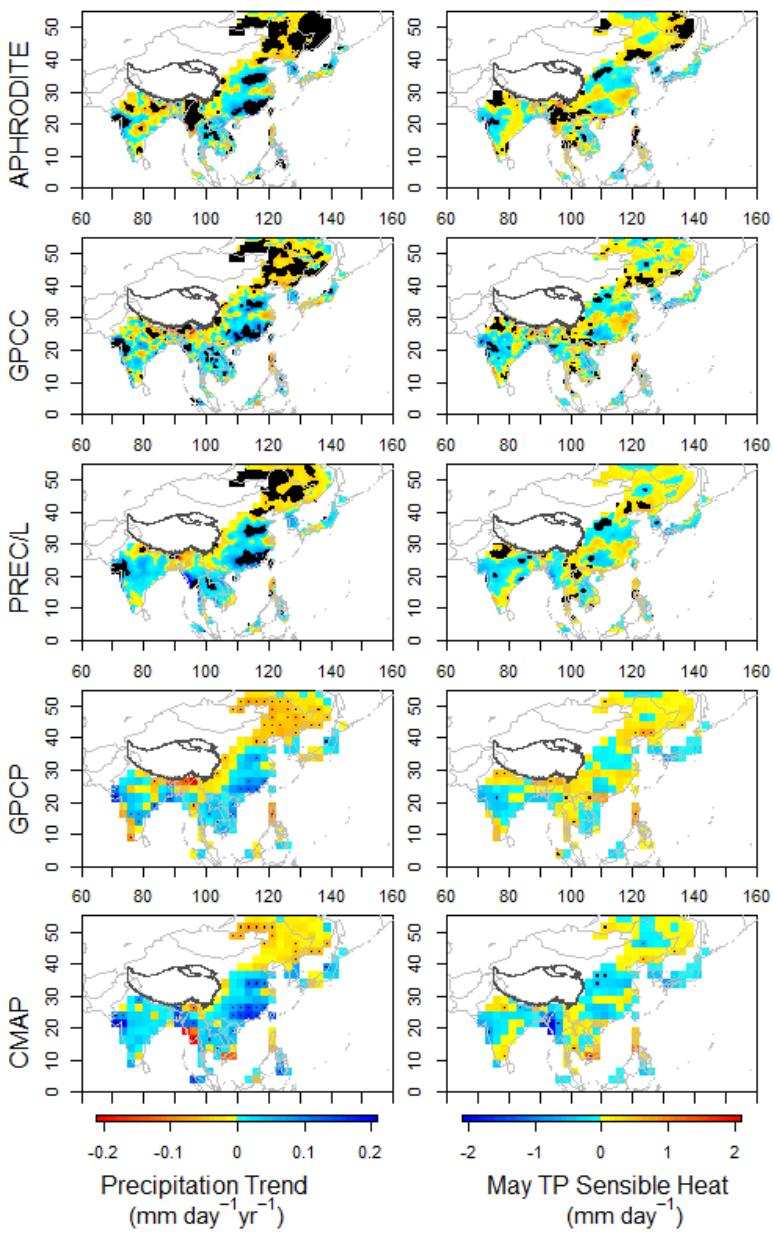

Figure 4-1 Linear trends of the summer rainfall, and partial regression coefficients of the summer rainfall on the sensible heat flux over the Tibetan Plateau in May. Results are shown over the Asian monsoon domains, which are defined by regions over land where the annual range of precipitation rates exceeds 2.5 mm day^{-1}. The black line represents the boundary of the Tibetan Plateau. Dots indicate trends and partial regression coefficients that are significant at the 90% confidence interval. Units of partial regression coefficients in all figures are per standard deviation of the variable being regressed.

4.1.2 Circulation and precipitation indices

To quantify the strength of the East Asian summer monsoon, circulation indices based on zonal wind difference, the OLR index, and precipitation indices were used in

this study (Table 4-3). The reversed East Asian summer monsoon index by Wang and Fan [*Wang and Fan*, 1999] (hereafter EASM-CI) was proven to be the best index for use (out of 25 existing indices) in terms of a correlation with the leading mode of interannual variability of the East Asian summer monsoon [*Wang et al.*, 2008a]. A strong East Asian summer monsoon, as indicated by the EASM-CI, was found to correspond with an enhanced Meiyu. Furthermore, the OLR index for the Southeast Asian summer monsoon (hereafter SEASM-OLR) was also used to illustrate the strength of the East Asian summer monsoon, since its variability has been found to indicate change in the East Asian summer monsoon [*Wang and Fan*, 1999; *Wang et al.*, 2008a]. In addition to the average precipitation from GPCP over monsoon area in China (EASM-PR), the average precipitation over three sub-regions in China was considered in this study: South China (hereafter EASM-PR-SC) defined as a monsoon region within [21°N–28 °N, 109°E–120°E] [*Luo et al.*, 2012]; the Yangtze River basin (hereafter EASM-PR-YZ) located within [27°N–33°N, 107.5°E–122.5°E] [*Yu et al.*, 2010]; and North China (hereafter EASM-PR-NC), located north of 37.5°N.

For the Indian summer monsoon, the circulation index (hereafter ISM-CI) and the OLR index (hereafter ISM-OLR) were applied as measures of its strength, in addition to the commonly used IMD all-India precipitation (ISM-PR) [*Wang and Fan*, 1999; *Yim et al.*, 2013]. Values obtained from EASM-CI and ISM-CI were found to be consistent with those derived from NRA-1 [*Kalnay et al.*, 1996], with a Pearson correlation of >0.93, suggesting that the derived monsoon circulation indices are data independent, and that they largely represent true variation in the dominant circulation associated with the two Asian monsoon systems. The monthly Niño 3 and Niño 3.4 indices were also used in this

study to represent the impact of ENSO on the Indian summer monsoon and the East Asian summer monsoon, respectively. The monthly NAO indices were calculated by applying rotated principal component analysis to the monthly standardized 500 hPa height anomalies at 20°N–90°N [*Barnston and Livezey*, 1987]. The Niño 3, Niño 3.4, and NAO indices were provided by the NOAA climate prediction center. All indices were normalized for the period from 1984 to 2007.

Table 4-3 Definition of the monsoon indices. CI denotes circulation index, OLR outgoing longwave radiation index, PR precipitation index, NC North China, SC South China, YZ Yangtze River basin, U_{850} zonal wind at 850 hPa, PR precipitation, OLR outgoing longwave radiation at top of atmosphere. All indices were computed using the summer anomalies except EASM-CI, ISM-OLR, and SEASM-OLR by using negative anomalies.

Index	Defining variable and region(s)	Reference
EASM-CI	U_{850} (5°N–15°N, 90° E–130°E) – U_{850} (22.5°N–32.5°N,110° E–140°E)	[*Wang and Fan*, 1999]
ISM-CI	U_{850} (5°N–15°N, 40°E–80°E) – U_{850} (25°N–35°N, 70°E–90°E)	[*Yim et al.*, 2013]
EASM-PR	China PR	This study
EASM-PR-NC	China PR (north of 37.5 °N)	This study
EASM-PR-SC	China PR (21°N–28 °N, 109°E–120°E)	[*Luo et al.*, 2012]
EASM-PR-YZ	China PR (27°N–33°N, 107.5°E–122.5°E)	[*Yu et al.*, 2010]
ISM-PR	All-India PR	[*Rajeevan et al.*, 2006]
ISM-OLR	OLR (10°N–25°N, 70°E–100°E)	[*Wang and Fan*, 1999]
SEASM-OLR	OLR (10°N–20°N, 115°E–140°E)	[*Wang and Fan*, 1999]

4.1.3 Methodologies

A flowchart of the methodologies is shown in Figure 4-2. The spring sensible heat anomalies over the Tibetan Plateau were first correlated with the surface and atmospheric conditions over the Tibetan Plateau to explain their variability, and to the SST and monsoon indices to test if they significantly impact the Asian summer monsoon. Multiple linear regression and the Granger causality test were then used to test whether there exist associations among the sensible heat anomalies and the summer monsoon rainfall.

Finally, composite analysis was applied to infer possible physical mechanisms of the impact of the spring sensible heat anomalies over the Tibetan Plateau on the Asian summer monsoon.

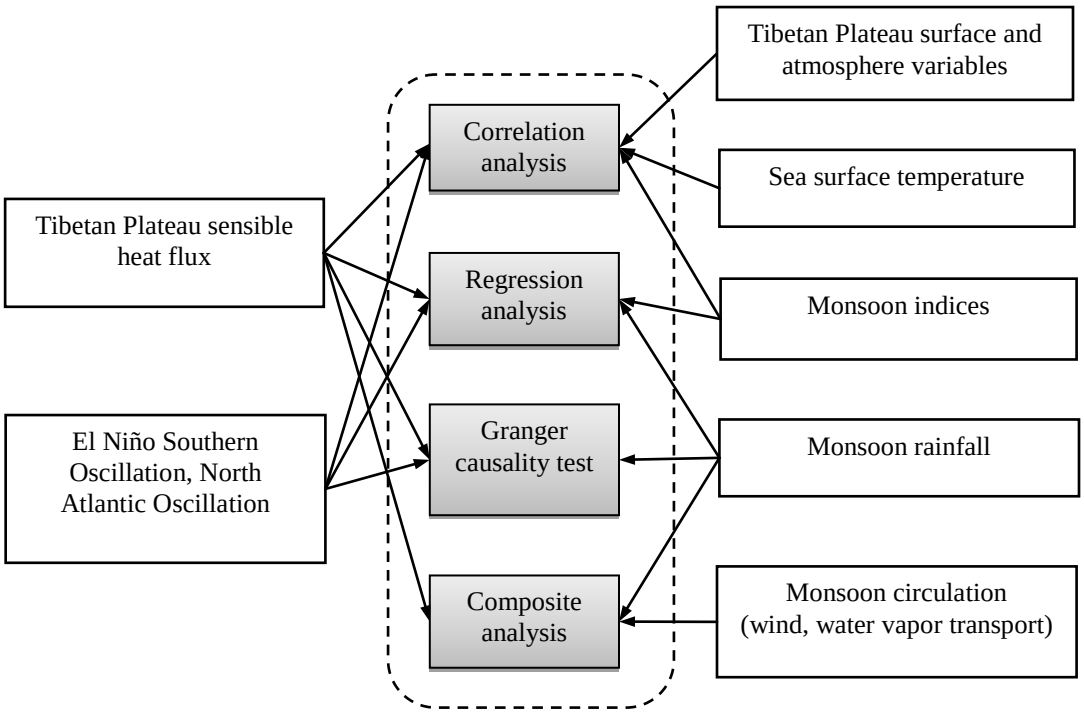

Figure 4-2 Flowchart of methods used to assess the impact of the spring sensible heat flux over the Tibetan Plateau on the Asian summer monsoon rainfall.

Correlation analysis is an effective approach used to identify any potential physical links between various data, and to infer any underlying cause-and-effect relationships. The dominant variability of the detrended spring sensible heat flux over the Tibetan Plateau was assessed by use of empirical orthogonal function analysis, and the Pearson correlation was computed to quantify the correlations between the spring sensible heat flux over the Tibetan Plateau and the related surface and atmospheric variables, in addition to the Asian summer monsoon indices. The two-tail student t-test was then applied to evaluate the statistical significance. In this study, a Pearson

correlation higher than 0.34 (0.40) was considered significant, with a p-value <0.1 (0.05), and a degree of freedom of 22. To analyze whether the relationship between the spring Tibetan Plateau sensible heat anomalies and the Asian summer monsoon are dependent on ENSO and NAO, the Pearson correlation between the spring sensible heat flux over the Tibetan Plateau, the Asian summer monsoon indices, and the SST anomalies were calculated at pixels over the ocean.

Multiple linear regression was used in this study because of its concise structure and coherent model parameters that have the potential to be related to physical mechanisms [*Duan et al.*, 2013; *Jiang and Liang*, 2013; *Rajagopalan and Molnar*, 2013]. In addition to the Tibetan Plateau sensible heat flux (*TP_H*), the April-May NAO (*NAO_AM*), and the May minus March Niño 3.4 (*NINO34_MMM*) were included in multiple linear regression for the East Asian summer monsoon (*EASM* in Equation 4-3) to represent the impact of the spring NAO and ENSO development [*Wu et al.*, 2009; *Wang et al.*, 2013a]. In addition, June–July–August Niño 3 (*NINO3_JJA*) from the preceding year was included in the multiple linear regression for the Indian summer monsoon (*ISM* in Equation 4-4) to represent the impact of ENSO [*Wu et al.*, 2009; *Shukla et al.*, 2011; *Wang et al.*, 2013a]. In Equations 4-3 and 4-4, β_i is the coefficient, and ε is the residual that is assumed to be normally distributed ($N(0, \sigma^2)$). To identify the spatial pattern of the relationship between the spring sensible heat anomalies over the Tibetan Plateau and the strength of the Asian summer monsoon, the partial regression coefficients of the Asian summer monsoon indices on the gridded sensible heat anomalies over the Tibetan Plateau were also computed:

$$EASM = \beta_1 NAO\_AM + \beta_2 NINO34\_MMM + \beta_3 TP\_H + \varepsilon, \varepsilon \sim N(0, \sigma^2)$$ **Equation 4-3**

$$ISM = \beta_1 NINO3\_JJA + \beta_2 TP\_H + \varepsilon, \varepsilon \sim N(0, \sigma^2)$$ **Equation 4-4**

The Granger causality test is an inferential method based on whether the time series of one variable (*x*) significantly contributes to the predictions of another variable (*y*), and it has been widely applied in the analysis of land-atmosphere-ocean interactions [*Granger*, 1969; *Kaufmann and Stern*, 1997; *Mosedale et al.*, 2006; *Mokhov et al.*, 2011; *Jiang et al.*, 2015]. Specifically, it tests the null hypothesis that *x* does not Granger-cause *y* if the auto regression of *y* with a lagged value of *y* and *k* controlled variables (with lag by *p*, Equation. 4-5) is not significantly improved by incorporating the lagged value of *x* (with lag by *q*, Equation 4-6) by using the F-test. The Granger causality test was applied to the precipitation anomalies (as Granger-effect (*y*)) and sensible heat anomalies (as Granger-cause (*x*)), with NAO and Niño 3.4 as controlled variables (*z*) for pixels within the Asian summer monsoon regions, except the Indian monsoon region with Niño 3 in the preceding years as the controlled variable. The Indian monsoon region is defined as a land area within [10°N–30°N, 70°E–105°E], as in Yim et al. [2013], and the choice of the controlled variable (preceding year Niño 3) accounts for the time lag when the Indian summer monsoon rainfall is most correlated with the ENSO [*Shukla et al.*, 2011]. The stationarity assumption was checked by the Augmented Dickey-Fuller (ADF) test (with constant and linear trends), and the maximum lag value for the Granger causality test was six months. The optimized lag value of the Granger effect and the controlled variables (P) were determined to minimize the final prediction error (FPE) of Equation 4-5, and the optimized lag value of the Granger-cause (Q) was then determined to minimize the FPE

of Equation 4-6, with a fixed lag of the Granger effect and controlled variables as its optimized lag value (P):

$$y_l = a_1 y_{l-1} + \ldots + a_p y_{l-p} + b_{1,1} z_{1,l-1} + \ldots + b_{1,p} z_{1,l-p} + \ldots + b_{k,1} z_{k,l-1} + \ldots + b_{k,p} z_{k,l-p} + \varepsilon$$

Equation 4-5

$$y_l = a_1 y_{l-1} + \ldots + a_p y_{l-p} + b_{1,1} z_{1,l-1} + \ldots + b_{1,p} z_{1,l-p} + \ldots + b_{k,1} z_{k,l-1} + \ldots + b_{k,p} z_{k,l-p} + c_1 x_{l-1} + \ldots + c_q x_{l-q} + \varepsilon$$

Equation 4-6

Composite analysis is used to elucidate the possible physical mechanisms involved in the linkage between the spring sensible heat flux over the Tibetan Plateau and the Asian summer monsoon. This method is widely used in the attribution of factors influencing the Asian summer monsoon [*Liu and Yanai*, 2002; *Lau and Kim*, 2006]. In this study, the composite of summer precipitation, 200-hPa wind, 800-hPa wind, vertically integrated water vapor transport, and water vapor transport convergence anomalies was calculated for years of anomalous high and low sensible heat flux over the Tibetan Plateau. The statistical significance of the composite anomaly was evaluated based on the student t-test.

4.2 Results and discussions

4.2.1 Variability of the spring sensible heat flux over the Tibetan Plateau and its correlation with the local surface and atmospheric conditions

The spatiotemporal variability of the spring sensible heat flux over the Tibetan Plateau is shown as the first two leading modes, according to EOF analysis of the detrended sensible heat flux over the Tibetan Plateau (Figure 4-3). The first leading mode (EOF1) of the spring sensible heat flux explains 37% of the total variance, with a coherent change over most regions of the Tibetan Plateau, and the second leading mode (EOF2) contributes to 13% of the total variance, with an opposite signal in the center of the Tibetan Plateau compared to that in the boundary ranges of the Tibetan Plateau. The temporal variability, as shown by the first principal component (PC1), suggests large interannual variability with a decelerated decline in the early 1990s and late 1990s, and an accelerated decline after 2000. However, the second component (PC2) resembles a decadal oscillation pattern. Neither PC1 nor PC2 exhibits any significant (p-value <0.1) correlation to the Asian summer monsoon indices.

The Pearson correlation analysis suggests that the sensible heat flux over the Tibetan Plateau is related to differing surface and atmospheric conditions in March, April, and May, but it displays a similar variability to that of net radiation at correlations larger than 0.9 (Table 4-4). The cloud conditions (indicated by cloud cover or temperature range) are significantly (p-value <0.1) related to the March and May sensible heat flux mainly through the cloud shortwave effect (reduction of surface downward shortwave irradiance). The mean temperature favors the partition of net radiation into sensible heat flux in May. Accordingly, the moist static energy at the surface is found to

be significantly (p-value <0.05) correlated with the sensible heat flux in May. The correlation between NDVI and the sensible heat flux is low in spring, which is possibly associated with reduced surface albedo but enhanced evapotranspiration from vegetation over the Tibetan Plateau in spring. A close positive correlation (p-value <0.05) with the atmospheric heat source is identified for the April and May sensible heat flux, which provides evidence that the middle and late spring sensible heat flux controls the variability of the atmospheric heat source over the Tibetan Plateau. The March sensible heat flux over the Tibetan Plateau is seen to increase by 0.7 W m^{-2} $decade^{-1}$ (p-value <0.1), and the May sensible heat flux is seen to decrease by -0.6 W m^{-2} $decade^{-1}$ (p-value <0.1) over the period 1984–2007, while the April sensible heat flux shows no significant trend.

To demonstrate whether the preceding spring sensible heat anomalies over the Tibetan Plateau can persist throughout the following summer, lag correlations were computed for the March, April, and May sensible heat anomalies and atmospheric heat source, with a lagged month range from one to six (Figure 4-4). March, April, and May sensible heat anomalies (de-trended) were significantly (p-value <0.05) correlated with the April, May, and June sensible heat anomalies, by 0.41 (0.41), 0.40 (0.47), and 0.55 (0.44), respectively. The results show that both the May sensible heat anomalies and the May atmospheric heat source anomalies sustain positive correlations with the June to September sensible heat anomalies and atmospheric heat source anomalies, respectively. Considering that only the May sensible heat anomalies could last throughout the following summer, the following analysis uses various statistical methods to test the

hypothesis of whether the Asian summer monsoon rainfall is under the impact of the late spring sensible heat flux over the Tibetan Plateau.

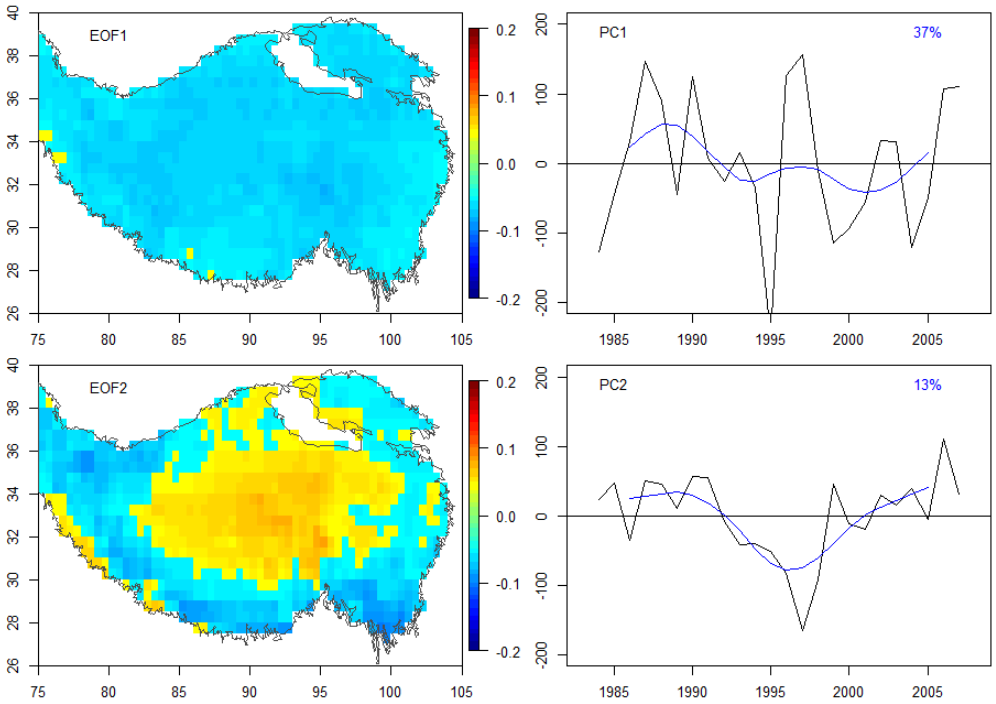

Figure 4-3 The first two leading modes (EOF1 and EOF2) of empirical orthogonal function analysis of the detrended spring sensible heat flux (Wm^{-2}) over the Tibetan Plateau, showing the spatial patterns (left) and the corresponding principal components (right, black lines). The 5-yr running mean of the principal components are shown as blue lines, and the variance explained by the first two principal components are shown as blue numbers.

Table 4-4 Pearson correlation between the March, April, and May sensible heat over the Tibetan Plateau and the surface and atmospheric anomalies over the Tibetan Plateau (p-value <0.1 are in bold).

	March	April	May
Sensible heat flux, cloud cover	**-0.36**	-0.28	0.07
Sensible heat flux, water vapor	-0.33	0.25	-0.03
Sensible heat flux, GIMMS NDVI	0.18	-0.12	0.09
Sensible heat flux, temperature range	**0.36**	0.16	**0.56**
Sensible heat flux, mean temperature	0.25	0.31	**0.37**
Sensible heat flux, snow cover	0.32	**0.46**	-0.10
Sensible heat flux, moist static energy	-0.13	0.28	**0.49**
Sensible heat flux, downward shortwave irradiance	**0.91**	**0.68**	**0.84**
Sensible heat flux, surface albedo	**-0.64**	**-0.42**	**-0.68**
Sensible heat flux, net shortwave radiation	**0.84**	**0.63**	**0.84**
Sensible heat flux, downward longwave radiation	**-0.44**	0.26	-0.05
Sensible heat flux, upward longwave radiation	0.02	0.09	**0.35**
Sensible heat flux, net longwave radiation	**-0.41**	0.07	**-0.41**
Sensible heat flux, net radiation	**0.97**	**0.93**	**0.92**
Sensible heat flux, atmospheric heat source	0.09	**0.47**	**0.41**

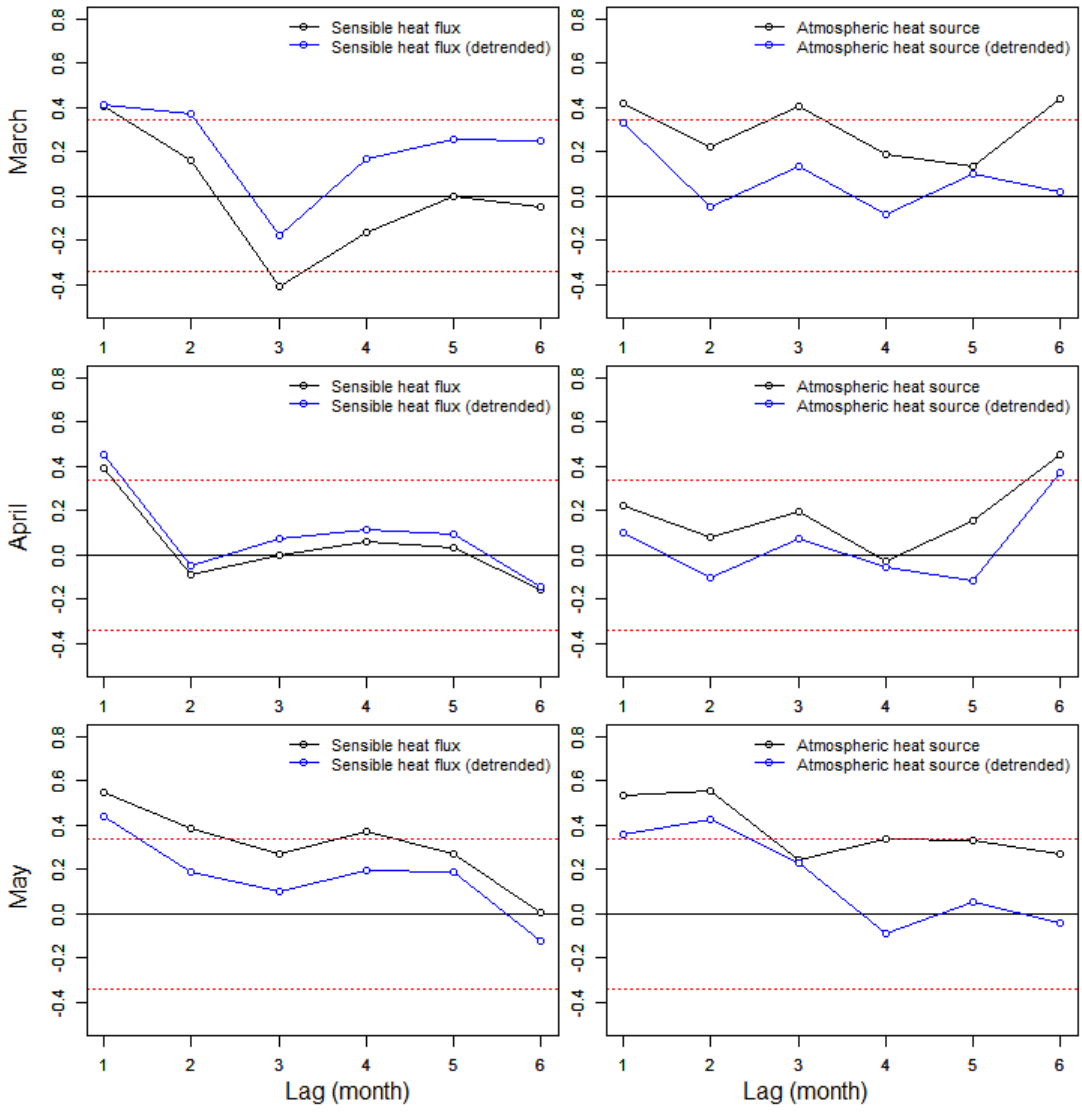

Figure 4-4 Lag correlations of the March, April, and May sensible heat flux (left) and atmospheric heat source (right) over the Tibetan Plateau, with lagged interval ranges from one month to six months. The correlations for the de-trended sensible heat flux and atmospheric heat source are shown in blue. Red dashed-lines indicate the critical value of the Pearson correlation for the 90% confidence interval.

4.2.2 Relationships between the late spring sensible heat flux over the Tibetan Plateau and the Asian summer monsoon rainfall

The correlation analysis suggests that the May sensible heat flux averaged over the Tibetan Plateau is positively correlated with the East Asian summer monsoon rainfall.

The May sensible heat flux over the Tibetan Plateau exhibits a significant (p-value <0.1) positive correlation with EASM-PR in the peak monsoon season by 0.37 (Figure 4-5). In addition, the May Tibetan Plateau sensible heat flux is found to be correlated with EASM-PR-YZ in the early monsoon season and EASM-PR-NC (by 0.46 and 0.33, respectively). These results is consistent with previous studies where a positive sensible heat anomalies over the Tibetan Plateau could enhance the East Asian summer monsoon through a stronger atmospheric heat source [*Wang et al.*, 2008c; *Duan et al.*, 2013]. The May sensible heat flux is not significantly correlated with ENSO indices and NAO in preceding seasons and summer, which suggest that the late spring sensible heat anomalies are independent from those widely used predictors of the Asian summer monsoon. In addition, the Pearson correlation between ISM-PR and the three ENSO indices exceeds 0.4 in the preceding summer. This stronger correlation to the previous summer ENSO indices than to that of any other seasons is consistent with the results of a previous study, where the positive correlation of the Indian summer precipitation to Niño 3 maximized with four to five season leads [*Shukla et al.*, 2011].

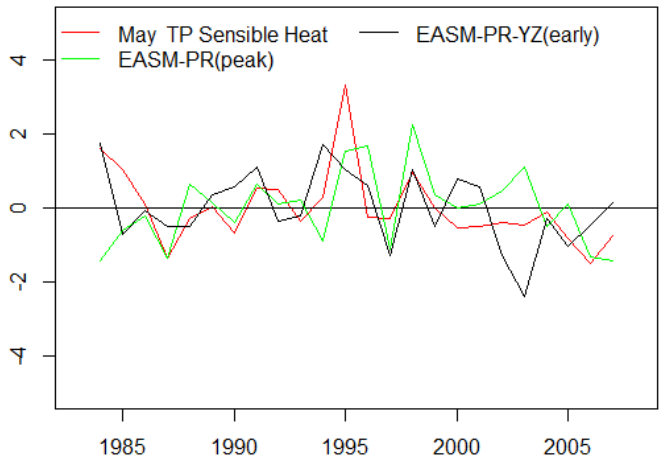

Figure 4-5 Comparison of EASM-PR in the peak monsoon season, EASM-PR-YZ in the early monsoon season with the May sensible heat flux over the Tibetan Plateau (TP). Value was normalized over the period 1984–2007.

The correlation and lag-correlation between the SST anomalies and the sensible heat anomalies suggest that the May sensible heat anomalies over the Tibetan Plateau are largely independent from ENSO and NAO. Figure 4-6 shows that EASM-CI is positively correlated with summer SST in the West Pacific and North Indian Oceans, and displays tripolar relationships in the North Atlantic [*Wu et al.*, 2009]. ISM-PR is associated with the SST of the equatorial Pacific through the Walker circulation [*Kumar et al.*, 2006], and significant correlations of ISM-PR with SSTs also exist over regions in the North Pacific and the North Atlantic through teleconnections [*Ding and Wang*, 2005; *Goswami et al.*, 2006]. Areas with significant correlation between the summer SST and the May sensible heat anomalies are mostly located at the tropical Indian Ocean, which is different from that of EASM-CI and ISM-PR. This result further supports the independency between the May Tibetan Plateau sensible heat anomalies and ENSO/NAO. As the late spring sensible heat anomalies and the atmospheric heat source over the Tibetan Plateau are capable of persisting throughout the summer, the lack of a similar correlation pattern of the SST anomalies with the May sensible heat flux over the Tibetan Plateau and the Asian summer monsoon indices indicates that the late spring sensible heat anomalies over the Tibetan Plateau mainly impact the Asian summer monsoon directly, providing a thermal impact as an elevated heat source. In addition, the late spring sensible heat anomalies may also be associated with the Indian summer monsoon through the air-sea interaction with the SST anomalies in Indian Ocean [*Yang et al.*, 2010].

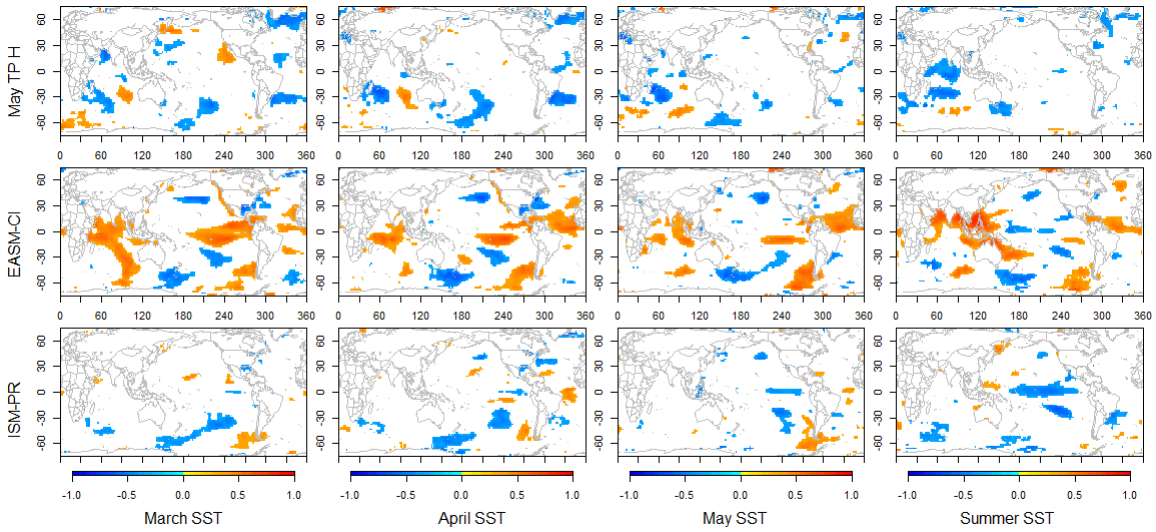

Figure 4-6 Pearson correlations between EASM-CI, ISM-PR, and the May sensible heat anomalies (H) over the Tibetan Plateau (TP), and the SST from the preceding March through the following summer. Correlations that are significant at the 90% confidence interval are shown.

The partial regression coefficients of the May sensible heat flux of pixels within the Tibetan Plateau on the Asian monsoon indices, implies that there is a close link between the late spring sensible heat flux over the Tibetan Plateau and the East Asian summer monsoon and Indian summer monsoon (Figure 4-7). The negative sensible heat anomalies over the center of the Tibetan Plateau in May suppress the summer rainfall in the north of China, but enhance the rainfall in the south of China in the peak monsoon season. In addition, a coherent positive correlation is identified between the May sensible heat flux and the summer rainfall in the Yangtze River basin in the early monsoon season. The May sensible heat flux over the northeastern and western Tibetan Plateau shows an opposite relationship to ISM-CI compared to that in the center of the Tibetan Plateau. Regions with a significant partial regression coefficient related to the all-India rainfall in the early and peak monsoon season are mostly confined to the north and south of the Tibetan Plateau. This result is different to that of a previous study, which identified

a general negative correlation between the Tibetan Plateau moist static energy at surface in early May and the all-India rainfall in the early monsoon season [*Rajagopalan and Molnar*, 2013]. This discrepancy is argued to be related to regional differences in the association between the sensible heat flux, the local surface and atmospheric conditions, and the teleconnection patterns over the Tibetan Plateau [*Cuo et al.*, 2013].

The late spring sensible heat anomalies over the Tibetan Plateau are contributed not only to the Asian summer monsoon circulation/OLR indices and the regional averaged rainfall, but also to the pattern of the summer rainfall trend. Overall, the summer rainfall is decreased over the north of China and the north of India, but is increased in the south of China and the west of India (Figure 4-1). Similar to that of rainfall changes, a decrease in the May sensible heat flux over the Tibetan Plateau can suppress rainfall over northern China and northern India, but enhance rainfall over western India. These results are consistent with those of previous studies, that attributed spring sensible heating changes over stations located at the center and east of the Tibetan Plateau to trends in summer rainfall over China [*Duan et al.*, 2013]. For the early monsoon season, the May sensible heat flux is closely related to rainfall over the lower reaches of the Yangtze and Yellow Rivers in China (Figure 4-8). The May sensible heat anomalies impact the rainfall in the peak monsoon season, which well reproduces the pattern of the rainfall trend in North and West India, and North and South China (Figure 4-9). The regions under the impact of the May sensible heat anomalies are confined to the Yellow River basin in the late monsoon season (Figure 4-10).

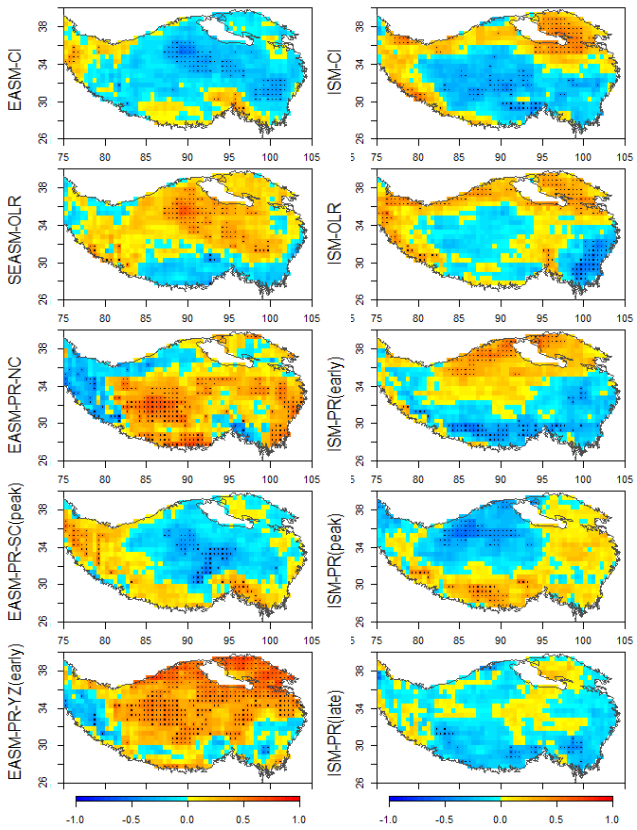

Figure 4-7 Partial regression coefficients of the East Asian monsoon indices (left) and Indian monsoon indices (right) on the May sensible heat flux anomalies over the Tibetan Plateau. Dots indicate partial regression coefficients that are significant at the 90% confidence interval.

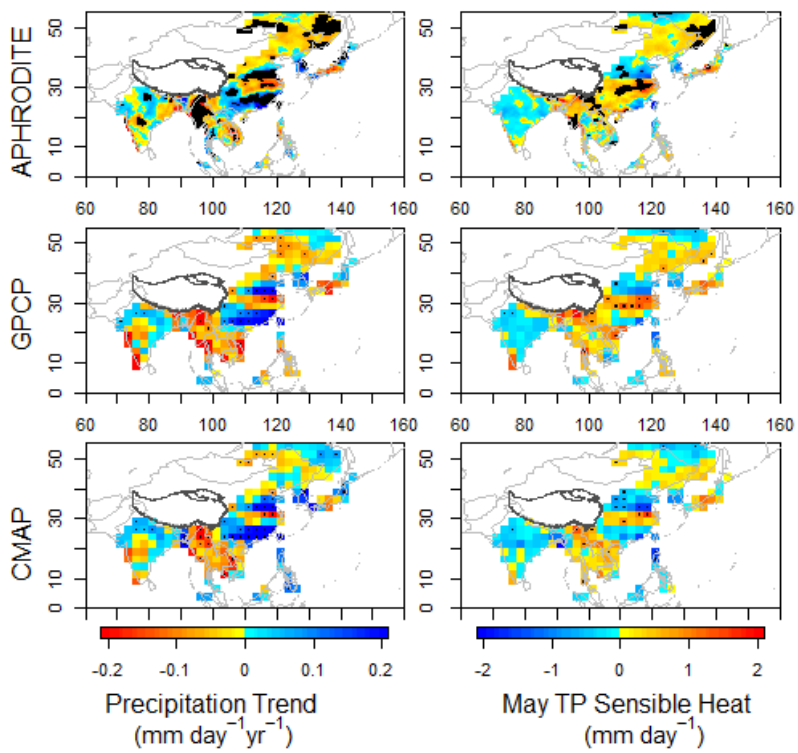

Figure 4-8 Same as Figure 4-1, but for the early monsoon season rainfall.

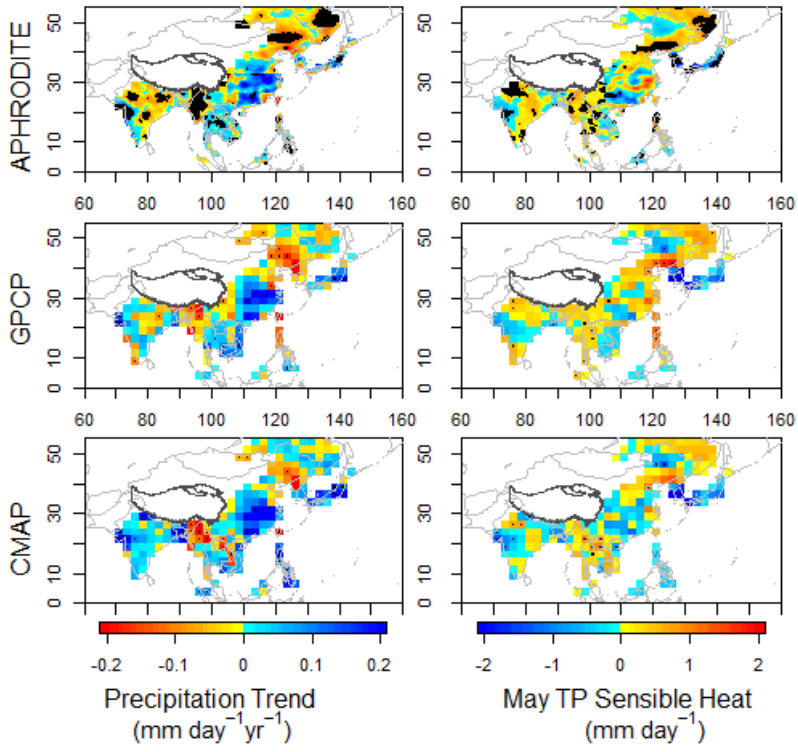

Figure 4-9 Same as Figure 4-1, but for the peak monsoon season rainfall.

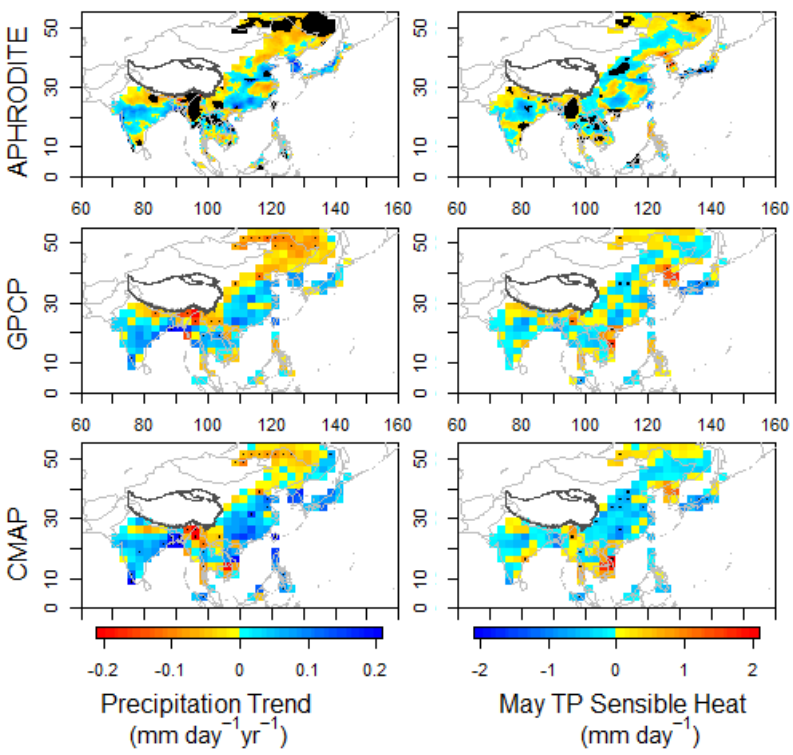

Figure 4-10 Same as Figure 4-1, but for the late monsoon season rainfall.

The Granger causality test implies that a significant cause-and-effect relationship exists between the spring sensible heat anomalies over the Tibetan Plateau and that of rainfall anomalies within the Asian summer monsoon regions. The ADF test indicates that anomalies of all analyzed variables are stationary, at a 10% level of significance. Figure 4-11 shows the optimized lags of significance in the Granger causality test, using the monthly sensible heat anomalies over the entire Tibetan Plateau as the Granger-cause, and the gridded rainfall anomalies in the summer months as the Granger-effect. The Granger causality test confirms that the spring Tibetan Plateau sensible heat anomalies Granger-cause the summer rainfall anomalies in India and northern China. The spring Tibetan Plateau sensible heat anomalies also Granger-cause rainfall anomalies in areas within southern China, especially in August. In addition, it is possible that other local and remote factors (such as changes in aerosol loading, snow cover, soil moisture, and land

cover) contribute to the spotted pattern seen in southern China and India [*Meehl*, 1994; *Liu and Yanai*, 2002; *Menon et al.*, 2002; *Fu*, 2003]. Nevertheless, the spatial extent of the area that is significant in the Granger causality test coincides with heavily populated centers and extensive agricultural land coverage in Asia, such as coastal areas, North China, and North and West India. Thus, such connections would imply an impact on the livelihood of local people, ecosystem dynamics, and on the carbon cycle within the Asian Monsoon regions [*Tian et al.*, 2003; *Piao et al.*, 2010].

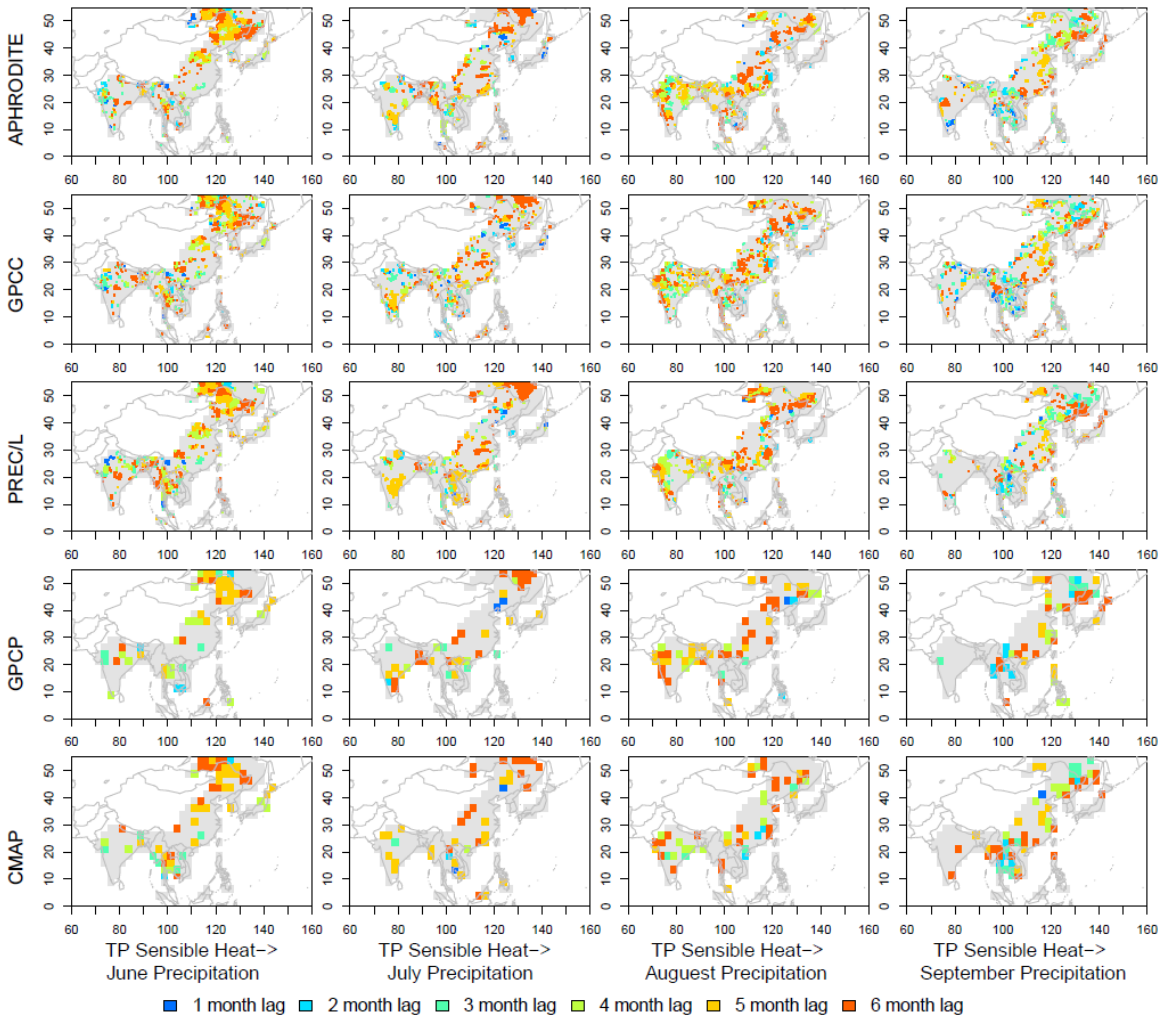

Figure 4-11 Granger causality test results of whether the sensible heat flux anomalies over the Tibetan Plateau Granger-cause precipitation intensity anomalies at pixels over the Asian monsoon region. Arrows are pointed from Granger-cause to Granger-effect. Grid points failing to pass the 10% level of significance are masked.

4.2.3 The Asian summer monsoon circulation associated with the late spring sensible heat flux over the Tibetan Plateau

The mechanisms by which the late spring sensible heat anomalies over the Tibetan Plateau affect the Asian summer monsoon rainfall were examined based on the composite analysis using years of anomalous high and low sensible heat. Four high years (1984, 1985, 1995, 1998) and four low years (1987, 2005, 2006, 2007) were selected. For the years of high sensible heat flux in late spring, the anomalous high sensible heat flux and atmospheric heat source persist throughout the summer (Figure 4-12). Consistent with a modeling study by Wang et al., [2008c], the high sensible heat flux leads to ascending motion and enhanced rainfall over the south of the Tibetan Plateau. This forms an upper level anticyclone, resulting in stronger westerlies (southerlies) to its north (south). The remote impact is found through two Rossby wave trains in the upper-level and lower-level atmosphere that moves westward along with the westerlies. A cyclone and an anticyclone are identified over Mongolia and the east of Japan as a part of the upper-level Rossby wave train. Meanwhile, an anticyclone over India and a cyclone over North Indian Ocean as a part of the lower-level Rossby wave train originated from the southwest of the Tibetan Plateau, reinforce the anticyclone over the western North Pacific. The lower-level Rossby wave train suppresses the moisture convergence over most area in India through a weakened monsoon westerly, but enhanced the moisture convergence over North China through a strengthened monsoon southerly.

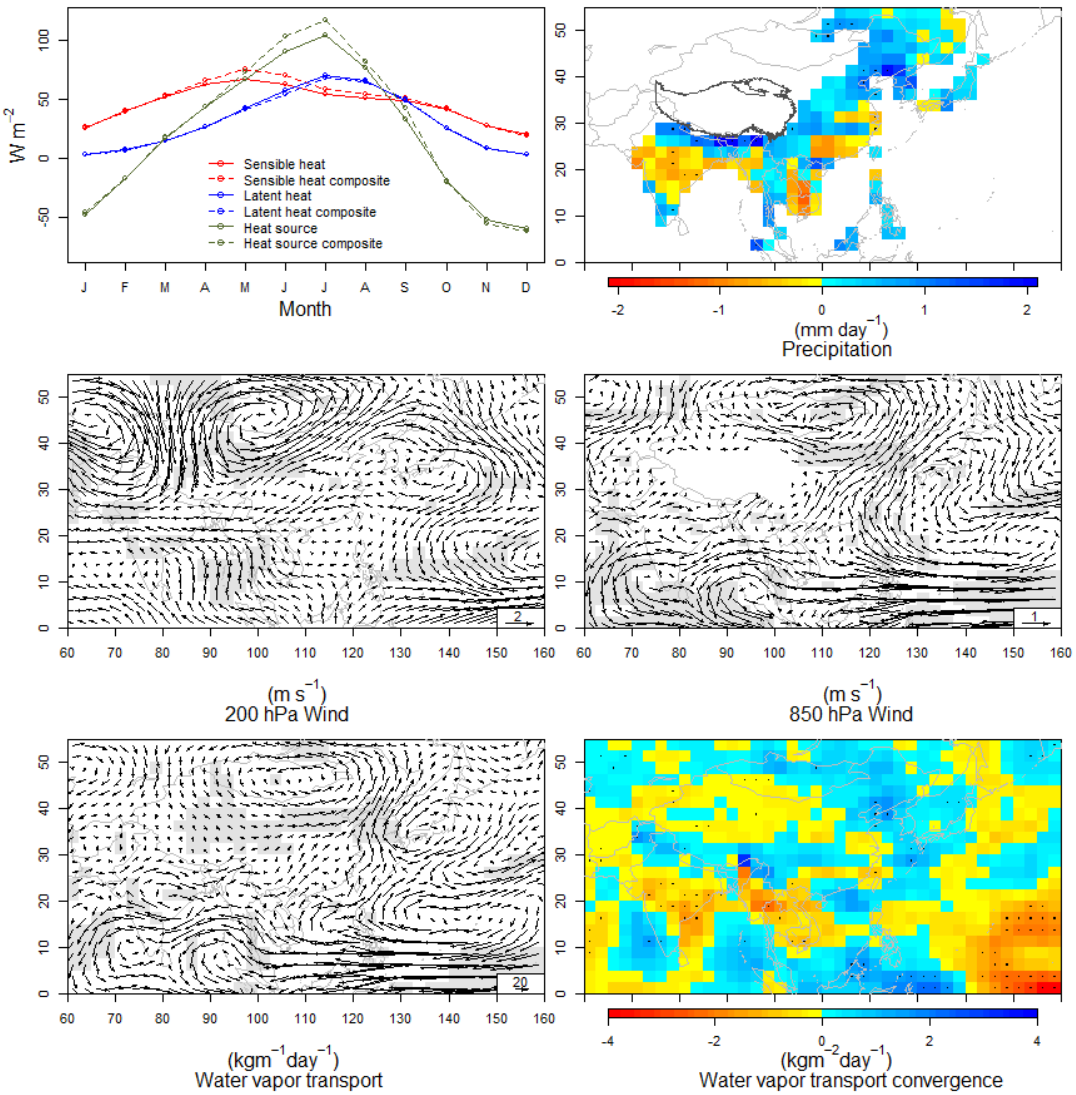

Figure 4-12 Composites of the seasonal cycles of the sensible and latent heat fluxes and heat source over the Tibetan Plateau, and the summer precipitation from GPCP, 850-hPa wind, 200-hPa wind, water vapor transport, and water vapor transport convergence anomalies during year of high late spring sensible heat flux over the Tibetan Plateau. Dots and grey shading denotes grids that are significant at the 90% confidence.

For the years of low late spring sensible heat flux over the Tibetan Plateau, the sensible heat flux in the following summer and early autumn is also low (Figure 4-13). A significant decrease of the atmospheric heat source is seen in the early summer. The low sensible heat flux in summer is associated with the reduced rainfall in the south of the Tibetan Plateau through a descending motion. This is accompanied with a descending

motion to its east [*Wang et al.*, 2008c], decreasing rainfall over the Yangtze River basin. Two Rossby wave trains also appear in the low sensible heat flux years: one in the upper atmosphere that is similar to that of high sensible heat years but with changes in their polarities, the other in the lower atmosphere with anticyclones over the northern India and South China Sea. Those changes in the lower level circulation dry the northern India but wet the western India.

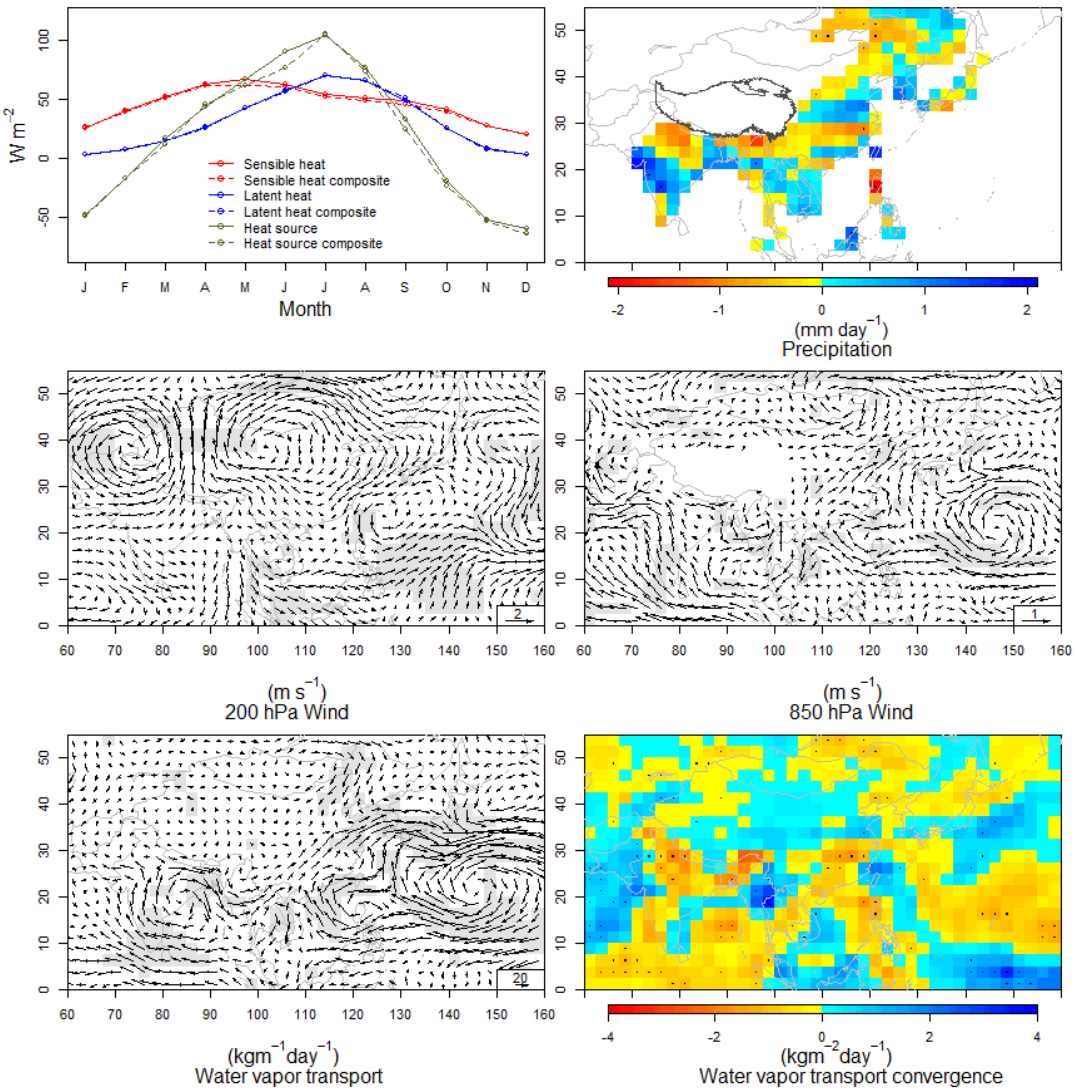

Figure 4-13 Composites of the seasonal cycles of the sensible and latent heat fluxes and heat source over the Tibetan Plateau, and the summer precipitation from GPCP, 850-hPa wind, 200-hPa wind, water vapor transport, and water vapor transport convergence anomalies during year of low late spring sensible heat flux over the Tibetan Plateau. Dots and grey shading denotes grids that are significant at the 90% confidence.

The presented link between the May sensible heat anomalies over the Tibetan Plateau and the Asian summer monsoon implies the importance of the spring surface radiation and the energy budget anomalies over the Tibetan Plateau to the waxing and waning of the Asian summer monsoon. Firstly, the sensible heat flux is considered to be highly related to the net radiation (dominated by the shortwave radiation budget), so that changes in spring cloud conditions (cloud cover, cloud duration, cloud structure) and snow conditions (snow cover, snow depth) over the Tibetan Plateau would have a profound impact on the summer precipitation over the Asian monsoon area through changes in downward shortwave radiation and surface albedo, respectively, which would result in sensible heat anomalies [*Zhang et al.*, 2004b; *Duan and Wu*, 2006]. Secondly, changes in vegetation condition (i.e., greenness, phenology) in late spring over the Tibetan Plateau could also alter the strength of the Asian summer monsoon, including the Indian summer monsoon, though the sensible heat anomalies [*Zhang et al.*, 2011a; *Zhang et al.*, 2013]. Furthermore, the projected future accelerated warming over the Tibetan Plateau could possibly be linked to an amplified change in the Asian summer monsoon through alteration of the partitioning of net radiation into sensible heat flux and latent heat flux over the Tibetan Plateau [*Collins et al.*, 2013].

4.4 Conclusions

The impact of the spring sensible heat anomalies over the Tibetan Plateau on the Asian summer monsoon rainfall was analyzed based on the fused sensible heat flux, the observed rainfall and SST, and the wind and water vapor transport from reanalysis. During the last two decades, the PC1 of the spring sensible heat flux over the Tibetan

Plateau has displayed large interannual variability, and PC2 has revealed a decadal oscillation. A partial regression of the Asian summer monsoon indices on the May sensible heat flux over the Tibetan Plateau, with both the ENSO development and spring NAO impact excluded, indicated a positive relationship with the rainfall over North China in summer and the rainfall over Yangtze River valley in the early monsoon season. A partial regression of the Asian summer monsoon indices on the May sensible heat flux over the Tibetan Plateau, with the previous summer ENSO excluded, suggested a close, but opposite, relationship with the all-India rainfall in the early and peak monsoon seasons over the north and south of the Tibetan Plateau. Summer rainfall from observations was shown to be dry in northern China, which is consistent with the impact from the decreased May sensible heat flux over the Tibetan Plateau. The rainfall changes associated with the decreased May sensible heat flux of the Tibetan Plateau also resembled patterns of rainfall changes in India and China in the peak monsoon season. The Granger causality tests provided further evidence that the Tibetan Plateau sensible heat anomalies Granger-cause the changes of summer rainfall in North China and India.

The physical mechanisms supporting the association between the late spring Tibetan Plateau sensible heat and the Asian summer monsoon rainfall were inferred from the composite analysis of 200 hPa and 850 hPa winds and water vapor transport. The sensible heat anomalies over the Tibetan Plateau in late spring persist throughout the following summer, and are believed to have influenced the East Asian and Indian summer rainfall through Rossby wave trains. It is considered that a lower-level Rossby wave train, which is associated with an enhanced sensible heat flux over the Tibetan Plateau, could promote rain in North China through strengthened southerly, but dry

weather in India through suppressed westerly. Conversely, a descending motion to the East of the Tibetan Plateau and a lower-level Rossby wave train, as a result of a weakened sensible heat flux over the Tibetan Plateau, could suppress rainfall in the Yangtze River basin and dry (wet) North (West) India, respectively. Interestingly, the results presented here indicate that variability in the surface and atmospheric conditions over the Tibetan Plateau in the preceding spring are related to sensible heat anomalies through the surface radiation and energy balance, and are therefore able to exert a notable influence on the Asian summer monsoon rainfall.

Chapter 5 Conclusions

The surface radiation and energy budgets over the Tibetan Plateau influence not only the local climate but also the East Asian summer monsoon. However, the spatial and seasonal variability of the surface radiation and energy budgets over the entire Tibetan Plateau have rarely been analyzed. Current estimates of the surface radiation and energy budgets from ground measurement are rather limited over the Tibetan Plateau, while models and satellite data are subject to large errors. Moreover, the linkage between the surface energy budget over the entire Tibetan Plateau and the Asian summer monsoon has not been evidenced in previous studies.

In this dissertation, the relationship between the surface energy budget over the Tibetan Plateau and the East Asian summer monsoon was quantified by synthesizing ground observations, remote sensing, and reanalysis datasets. The main goals were to analyze the spatial pattern and seasonal variability of the surface radiation and energy budgets over the Tibetan Plateau, how the interannual variation of the surface radiation and energy budgets relate to the surface and atmospheric conditions over the Tibetan Plateau, and whether the spring sensible heat anomalies over the Tibetan Plateau can explain the changes of the Asian summer monsoon rainfall.

To address those questions, a monthly surface radiation and energy budgets data at 0.5° over the Tibetan Plateau was first developed by applying a multiple linear regression data fusion scheme. It integrated various reanalysis products (CFSR, MERRA, ERA-Interim, JRA-25), remote sensing datasets (GEWEX-SRB, ISCCP-FD, Zhang10, GLEAM-LE), and in situ observations (AsiaFlux, ChinaFLUX, GAME/Tibet,

CAMP/Tibet), and covered a period from 1984 to 2007. Second, the annual and seasonal mean and STD of the fused surface radiation and energy budgets over the Tibetan Plateau were quantified. The correlation of the annual and seasonal anomalies of the fused surface radiation and energy budgets over the Tibetan Plateau with the observed surface and atmospheric conditions was also analyzed. Third, the sensible heat flux from the fused surface energy budget, precipitation and SST from observations, and wind and water vapor transport from reanalysis were used to analyze the impact of the spring sensible heat anomalies over the Tibetan Plateau on the Asian summer monsoon rainfall by various statistical methods. Major findings of this dissertation are summarized in section 5.1. Major contributions and future directions are described in sections 5.2 and 5.3, respectively.

5.1 Major findings

The cross-validation results suggest that the fused surface radiation and energy budgets over the Tibetan Plateau are more accurate than most calibrated reanalysis/remote sensing datasets: it exhibits the lowest RMSE_CVs at the monthly scale for downward shortwave irradiance, albedo, net shortwave radiation, net longwave radiation, net radiation, sensible heat flux, latent heat flux, and ground heat flux, by 15.1 Wm^{-2}, 0.05, 15.8 Wm^{-2}, 13.4 Wm^{-2}, 18.9 Wm^{-2}, 10.3 Wm^{-2},14.3 Wm^{-2}, and 2.6 Wm^{-2}, respectively; the RMSE_CVs of the fused upward shortwave radiation, downward longwave radiation, and upward longwave radiation (by 9.7 Wm^{-2}, 13.3 Wm^{-2}, and 8.4 Wm^{-2}, respectively) are also comparable to the most accurate products in terms of little difference of RMSE_CVs (within 0.5 Wm^{-2}). The fused downward shortwave irradiance represents the interannual variation averaged over CMA radiation sites well, and the

fused sensible heat flux captures the monthly cycle averaged over CMA stations consistently (Yang09). The uncertainty of fused surface radiation and energy budget sourced from the error of input reanalysis and remote sensing datasets and instrumental errors at stations is larger than that from the selection of the data fusion approaches and the interpolation scales.

The seasonal mean value of the fused shortwave and longwave radiation is high in summer and low in winter for most areas over the Tibetan Plateau, while the STD of the fused shortwave and longwave radiation was high in spring and autumn. Over the Tibetan Plateau, the results indicate the following relationships: 1) temperature range (as an indirect indicator of cloud conditions) is positively related to downward shortwave irradiance and net radiation; 2) cloud cover is negatively related to downward shortwave irradiance and positively related to downward longwave radiation; 3) snow cover (NDVI) is positively (negatively) related to albedo; and 4) water vapor and temperature dominate the interannual variation of downward longwave radiation and upward longwave radiation, respectively. The variations in the net radiation are likely due to the integrated effects of shortwave and longwave radiation, and the dominant surface and atmospheric variables for the net radiation anomalies varied seasonally.

The fused latent heat flux and sensible heat flux display different seasonal evolution and distribution patterns over the Tibetan Plateau. The highest value area of latent heat flux is located in the east Tibetan Plateau and the south face of the southwest ranges, which are largely affected by the summer monsoon, whereas the sensible heat flux is high in the ranges of the western Tibetan Plateau, which are dry in spring and summer. A strong correlation between latent heat flux and water vapor exists in all

seasons except spring, whereas a strong high correlation to sensible heat flux exists in spring and summer but in opposite directions. During summer, the number of significant correlated variables with the sensible and latent heat fluxes is the largest, and the magnitude of most correlations is also the largest for all seasons. Evaluations of the surface energy budget components in CMIP5 models over the Tibetan Plateau, using the fused surface energy budget as a reference, suggest that most models underestimate the sensible heat flux and net radiation by -14.3 Wm^{-2} and -5.9 Wm^{-2}, but overestimate the latent heat flux by 6.5 Wm^{-2}, which is associated with the biases in downward longwave radiation and soil moisture.

The sensible heat flux from the fused surface energy budget, precipitation and SST from observations, and wind and water vapor transport from reanalysis were used to analyze the impact of the late spring sensible heat anomalies over the Tibetan Plateau on the Asian summer monsoon rainfall over a period from 1984 to 2007. In summer, the observed dry in North China and North India and wet in West India are consistent with the impact from the decreased May sensible heat flux over the Tibetan Plateau. The Granger causality tests suggest that the sensible heat anomalies over the Tibetan Plateau Granger-cause rainfall changes in the North China and India in summer. The anomalous high sensible heat flux over the Tibetan Plateau in late spring, which can persist throughout the summer, could strength (weak) the southerly (westerly) and enhance (suppress) the moisture over North China (India) through a lower level Rossby wave train. On the other hand, the anomalous low sensible heat flux could dry the Yangtze River basin though a descending motion to the east of the Tibetan Plateau as well as dry (wet) the North (West) India through a lower level Rossby wave train.

5.2 Major contributions

The characterization of the regional spatiotemporal pattern of the surface radiation and energy budgets over the Tibetan Plateau using the fused data in this study is the first synthesized analysis at the spatial scale covering the entire plateau with continuous temporal coverage over two decades. The results of this study contribute to the understanding of the land-atmosphere interactions over the Tibetan Plateau and its impact on climate changes, the possible causes of the biases in the surface energy budget from climate models over the Tibetan Plateau, and the evidence of the linkage between the spring sensible heating over the Tibetan Plateau and the Asian summer monsoon rainfall.

The quantifications and discussions of the relationship between the observed evidence (i.e., the changes in the surface and atmospheric conditions) and the fused surface radiation and energy budgets over the Tibetan Plateau contribute to the understanding of climate change over the Tibetan Plateau in recent decades. The results imply that the coherent changes in the surface and atmospheric variables are related to the surface energy budget anomalies over the Tibetan Plateau by influencing the surface radiation budget, transpiration (evaporation) of vegetation (soil), or temperature gradient. This result highlights the importance of the land–biosphere–atmosphere interactions over the Tibetan Plateau in regulating the temporal variation of the surface sensible and latent heat fluxes. Furthermore, this analysis has the potential to infer critical components of the land-atmosphere interactions to advance the understanding of the impact of the changes in the surface radiation and energy budgets over the Tibetan Plateau on the local climate.

The confidence of the future projections from the CMIP5 models has been strengthened for the consistent seasonal cycles of the net radiation, sensible heat flux, and latent heat flux with those from the fused data. The biases of the downward longwave radiation and soil moisture are postulated to be the dominant factors causing the seasonal biases of the surface energy budget components over the Tibetan Plateau in CMIP5 models. It highlights the importance of the accurate representation of those fundamental surface and atmosphere variables that can propagate errors to the surface energy budget, which will benefit the model developments over the third pole and mountain areas that are sensitive to climate change.

In previous studies, the relationship that the changes of the sensible heat flux over the entire Tibetan Plateau is driving the changes of the East Asian summer monsoon has only been hypothesized by modeling; therefore, the physical evidence of such hypothesis using the surface energy budget components at a spatial-continuous scale over the Tibetan Plateau remains largely unknown. The assessment of the impact of the spring sensible heat anomalies over the Tibetan Plateau on the Asian summer monsoon rainfall fill in the gap by using correlation analysis, regression analysis, the Granger causality test, and composite analysis, based on the fused sensible heat flux. The inferred impact of the late spring sensible heat anomalies over the Tibetan Plateau on the Asian summer monsoon could contribute to the understanding of the possible drivers of the interannual variability of the Asian summer monsoon rainfall by delivering implications that will benefit local agriculture practices, disaster management, and climate change mitigation. The results also highlight the importance of the surface and atmospheric conditions over the Tibetan Plateau in the preceding spring, which are related to sensible heat anomalies

through the surface radiation and energy balance, and are therefore able to exert a notable influence on the Asian summer monsoon rainfall.

5.3 Future directions

This dissertation is a preliminary study in characterizing the surface radiation and energy budget over the Tibetan Plateau by integrating observational and reanalysis data sets. The validation results suggest the fused monthly surface radiation and energy budgets lower the RMSE_CVs than that of individual remote sensing or reanalysis dataset, but the fidelity of this validation is largely limited by the sparse and uneven-distributed ground observations over the Tibetan Plateau. Cautions should be exercised when comparing the fused datasets (as well as the gridded satellite or reanalysis datasets) with the ground measurements. The fidelity of such comparisons to infer the true accuracy is limited by the scale-mismatch (between the surface observations at a single point and the satellite retrievals over the pixel area), which is related to not only surface homogeneity (i.e., land cover type and topography) but also atmospheric conditions (i.e., cloud coverage, cloud type, and altitude variations) [*Li et al.*, 1995; *Li et al.*, 2005; *Hakuba et al.*, 2013]. Given that a dense observation network of the surface radiation and energy budgets has yet to be constructed over the Tibetan Plateau, the mismatch issue over the Tibetan Plateau is still open and recommended to be investigated in future after establishing a comprehensive observation network. In addition, the presented comparisons of various data fusion methods are limited to empirical method and do not include modeling. Therefore, comparisons of the results with those from data assimilation techniques remain a key topic for future research.

The study on the association between the surface and atmospheric variables and the surface energy and radiation anomalies over the Tibetan Plateau suggests that there is a seasonal dependence of the dominant variables. This result prompts interest in further understanding of the role of the changes in land–biosphere–atmosphere interactions over the Tibetan Plateau in regulating local climate. The physical mechanisms by which land–biosphere–atmosphere interactions mitigate or amplify the anomalies of the surface radiation and energy budgets over the Tibetan Plateau have received little attention; therefore, future investigation should address this challenge by using models capable of reproducing past climate changes and variations of the surface radiation and energy budgets over the Tibetan Plateau. It would also be interesting to disentangle the drivers and responses of the surface radiation and energy budget anomalies over the Tibetan Plateau in future research from evidences of modeling results.

The study presented here is considered to be an initial step in evidencing the linkage between the spring sensible heat anomalies over the Tibetan Plateau and the Asian summer monsoon rainfall anomalies. The interannual variability of the Asian summer monsoon may also be regulated by other external and internal factors that have not been explicitly examined here, such as variability of anthropogenic and natural aerosols [*Menon et al.*, 2002; *Vinoj et al.*, 2014], snow cover [*Liu and Yanai*, 2002; *Yim et al.*, 2010], and soil moisture [*Meehl*, 1994; *Zhang et al.*, 2011b]. Thus, gaining evidence of such linkages, and quantification of relative contributions and the interaction of multiple factors in relation to the Asian summer monsoon rainfall are recommended for future work.

Abbreviations

AAN	Asian Automatic Weather Station Network
ADF	Augmented Dickey-Fuller Test
AO	Arctic Oscillation
APHRODITE	Asian Precipitation—Highly Resolved Observational Data Integration Towards Evaluation of Water Resources Project
AVHRR	Advanced Very High Resolution Radiometer
BIC	Bayesian Information Criterion
BMA	Bayesian Model Averaging
CAMP/Tibet	CEOP Asia–Australia Monsoon Project on the Tibetan Plateau
CEOP	Coordinated Energy and Water Cycle Observation Project
CERES SYN	Regional Radiative Fluxes and Clouds Product from the Clouds and the Earth's Radiant Energy System
CFSR	Climate Forecast System Reanalysis
CLM	Common Land Model
CMA	Chinese Meteorological Administration
CMAP	Climate Prediction Center Merged Analysis of Precipitation
CRU	Climate Research Unit
D_R^2	Coefficient of Determination after Deseasonalization
EASM-CI	East Asian Summer Monsoon Circulation Index
EASM-PR	East Asian Summer Monsoon Precipitation Index for China
EASM-PR-NC	East Asian Summer Monsoon Precipitation Index for North China
EASM-PR-SC	East Asian Summer Monsoon Precipitation Index for South China
EASM-PR-YZ	East Asian Summer Monsoon Precipitation Index for Yangtze River Basin
ECMWF	European Centre for Medium-Range Weather Forecasts
ENSO	El Niño-Southern Oscillation
EOF	Empirical Orthogonal Function
ERA-Interim	ECMWF Interim Reanalysis
ERSST	Extended Reconstructed Sea Surface Temperature
FPE	Final Prediction Error
GAME/Tibet	GEWEX Asian Monsoon Experiment on the Tibetan Plateau
GEWEX-SRB	The Global Energy and Water Cycle Experiment Surface Radiation

	Budget
GIMMS	Global Inventory Modeling and Mapping Studies
GISS	Goddard Institute for Space Studies
GLDAS	Global Land Data Assimilation Systems version
GLEAM-LE	Global Land Evaporation: the Amsterdam Methodology
GPCC	Global Precipitation Climatology Centre
GPCP	Global Precipitation Climatology Project
IMD	India Meteorological Department
ISCCP-FD	International Satellite Cloud Climatology Project Global Radiative Flux Data Product
ISM-CI	Indian Summer Monsoon Circulation Index
ISM-OLR	Indian Summer Monsoon Outgoing Longwave Radiation Index
ISM-PR	All-India Precipitation Index
JMA/CRIEPI	Japan Meteorological Agency and Central Research Institute of Electric Power Industry
JRA-25	Japanese 25-year Reanalysis
MBE	Mean Bias Error
MERRA	Modern-Era Retrospective Analysis for Research and Applications
MODIS	Moderate Resolution Imaging Spectroradiometer
MOS	Mosaic Model
NAO	North Atlantic Oscillation
NASA	National Aeronautics and Space Administration
NCAR	National Center for Atmospheric Research
NCEP	National Centers for Environmental Prediction
NDVI	Normalized Differential Vegetation Index
NMIC	National Meteorological Information Center
NOAA	National Oceanic and Atmospheric Administration
NOAH	National Centers for Environmental Prediction/Oregon State University/Air Force/Hydrologic Research Lab Model
NRA-1	NCEP/NCAR Reanalysis 1
NRA-2	NCEP Department of Energy Atmospheric Model Intercomparison Project Reanalysis
OLR	Outgoing Longwave Radiation

PC	Principle Component
PCA	Principle Analysis Regression
PREC/L	Precipitation Reconstruction over Land
PU-LE	Evapotranspiration from a Princeton University Study
RF	Random Forest
RMSE	Root Mean Square Error
RMSE_CV	Root Mean Square Error from Cross Validation
SEASM-OLR	Southeast Asian Summer Monsoon Outgoing Longwave Radiation
SST	Sea Surface Temperature
STD	Standard Deviation
SVM	Supported Vector Regression

References

Adler, R. F., G. J. Huffman, A. Chang, R. Ferraro, P. P. Xie, J. Janowiak, B. Rudolf, U. Schneider, S. Curtis, D. Bolvin, A. Gruber, J. Susskind, P. Arkin, and E. Nelkin (2003), The version-2 global precipitation climatology project (GPCP) monthly precipitation analysis (1979-present), *Journal of Hydrometeorology*, *4*(6), 1147-1167.

An, Z., J. E. Kutzbach, W. L. Prell, and S. C. Porter (2001), Evolution of Asian monsoons and phased uplift of the Himalaya-Tibetan plateau since Late Miocene times, *Nature*, *411*(6833), 62.

Baldocchi, D., E. Falge, L. Gu, R. Olson, D. Hollinger, S. Running, P. Anthoni, C. Bernhofer, K. Davis, R. Evans, J. Fuentes, A. Goldstein, G. Katul, B. Law, X. Lee, Y. Malhi, T. Meyers, W. Munger, W. Oechel, K. T. Paw, K. Pilegaard, H. P. Schmid, R. Valentini, S. Verma, T. Vesala, K. Wilson, and S. Wofsy (2001), FLUXNET: a new tool to study the temporal and spatial variability of ecosystem-scale carbon dioxide, water vapor, and energy flux densities, *Bulletin of the American Meteorological Society*, *82*(11), 2415-2434.

Barnston, A. G., and R. E. Livezey (1987), Classification, seasonality and persistence of low-frequency atmospheric circulation patterns, *Monthly Weather Review*, *115*(6), 1083-1126.

Bjerknes, J. (1969), Atmospheric teleconnections from the equatorial pacific 1, *Monthly Weather Review*, *97*(3), 163-172.

Blockeel, H., and J. Struyf (2003), Efficient algorithms for decision tree cross-validation, *Journal of Machine Learning Research*, *3*(4-5), 621-650.

Bollasina, M. A., M. Yi, and V. Ramaswamy (2011), Anthropogenic aerosols and the weakening of the South Asian summer monsoon, *Science*, *334*(6055), 502-505.

Bounoua, L., G. J. Collatz, S. O. Los, P. J. Sellers, D. A. Dazlich, C. J. Tucker, and D. A. Randall (2000), Sensitivity of climate to changes in NDVI, *Journal of Climate*, *13*(13), 2277-2292.

Breiman, L. (2001), Random Forests, *Machine Learning*, *45*(1), 5-32.

Bristow, K. L., and G. S. Campbell (1984), On the relationship between incoming solar radiation and daily maximum and minimum temperature, *Agricultural and Forest Meteorology*, *31*(2), 159-166.

Chen, F., K. Mitchell, J. Schaake, Y. K. Xue, H. L. Pan, V. Koren, Q. Y. Duan, M. Ek, and A. Betts (1996), Modeling of land surface evaporation by four schemes and comparison with FIFE observations, *Journal of Geophysical Research: Atmospheres*, *101*(D3), 7251-7268.

Chen, M., W. Shi, P. Xie, V. B. S. Silva, V. E. Kousky, R. Wayne Higgins, and J. E. Janowiak (2008), Assessing objective techniques for gauge-based analyses of global daily precipitation, *Journal of Geophysical Research: Atmospheres*, *113*(D4), D04110.

Chen, M. Y., P. P. Xie, J. E. Janowiak, and P. A. Arkin (2002), Global land precipitation: A 50-yr monthly analysis based on gauge observations, *Journal of Hydrometeorology*, *3*(3), 249-266.

Chen, X., Z. Su, Y. Ma, K. Yang, and B. Wang (2013), Estimation of surface energy fluxes under complex terrain of Mt. Qomolangma over the Tibetan Plateau, *Hydrology and Earth System Sciences*, *17*(4), 1607-1618.

CMA (1996), *Meteorological radiation observation method*, 165 pp., Meteorol. Press, Beijing.

Collins, M., R. Knutti, J. Arblaster, J.-L. Dufresne, T. Fichefet, P. Friedlingstein, X. Gao, W. J. Gutowski, T. Johns, G. Krinner, M. Shongwe, C. Tebaldi, A. J. Weaver, and M. Wehne (2013), Long-term climate change: projections, commitments and irreversibility, in *Climate Change 2013: The Physical Science Basis. Contribution of Working Group I to the Fifth Assessment Report of the Intergovernmental Panel on Climate Changee*, edited by T. F. Stocker, D. Qin, G.-K. Plattner, M. Tignor, S. K. Allen, J. Boschung, A. Nauels, Y. Xia, V. Bex and P. M. Midgley, pp. 1029-1136, Cambridge University Press, Cambridge, United Kingdom and New York, NY, USA.

Cuo, L., Y. Zhang, Q. Wang, L. Zhang, B. Zhou, Z. Hao, and F. Su (2013), Climate change on the northern Tibetan Plateau during 1957-2009: Spatial patterns and possible mechanisms, *Journal of Climate*, *26*(1), 85-109.

Dee, D., S. M. Uppala, A. J. Simmons, P. Berrisford, P. Poli, S. Kobayashi, U. Andrae, M. A. Balmaseda, G. Balsamo, P. Bauer, P. Bechtold, A. C. M. Beljaars, L. van de Berg, J. Bidlot, N. Bormann, C. Delsol, R. Dragani, M. Fuentes, A. J. Geer, L. Haimberger, S. B. Healy, H. Hersbach, E. V. Hólm, L. Isaksen, P. Kållberg, M. Köhler, M. Matricardi, A. P. McNally, B. M. Monge-Sanz, J. J. Morcrette, B. K. Park, C. Peubey, P. de Rosnay, C. Tavolato, J. N. Thépaut, and F. Vitart (2011), The ERA-Interim reanalysis: configuration and performance of the data assimilation system, *Quarterly Journal of the Royal Meteorological Society*, *137*(656), 553-597.

Ding, Q. H., and B. Wang (2005), Circumglobal teleconnection in the Northern Hemisphere summer, *Journal of Climate*, *18*(17), 3483-3505.

Douville, H., J. F. Royer, and J. F. Mahfouf (1995), A new snow parameterization for the Météo-France climate model, *Climate Dynamics*, *12*(1), 21-35.

Douville, H., P. Viterbo, J.-F. Mahfouf, and A. C. M. Beljaars (2000), Evaluation of the optimum interpolation and nudging techniques for soil moisture analysis using FIFE data, *Monthly Weather Review*, *128*(6), 1733-1756.

Duan, A., and G. Wu (2006), Change of cloud amount and the climate warming on the

Tibetan Plateau, *Geophysical Research Letters*, *33*(22), L22704.

Duan, A., M. Wang, Y. Lei, and Y. Cui (2013), Trends in summer rainfall over China associated with the Tibetan Plateau sensible heat source during 1980-2008, *Journal of Climate*, *26*(1), 261-275.

Ebisuzaki, W., and L. Zhang (2011), Assessing the performance of the CFSR by an ensemble of analyses, *Climate Dynamics*, *37*(11), 2541-2550.

Ek, M. B., K. E. Mitchell, Y. Lin, E. Rogers, P. Grunmann, V. Koren, G. Gayno, and J. D. Tarpley (2003), Implementation of Noah land surface model advances in the National Centers for Environmental Prediction operational mesoscale Eta model, *Journal of Geophysical Research: Atmospheres*, *108*(D22), 8851.

Endo, H., and A. Kitoh (2014), Thermodynamic and dynamic effects on regional monsoon rainfall changes in a warmer climate, *Geophysical Research Letters*, *41*, 1704-1710.

Fairall, C., P. Persson, E. Bradley, R. Payne, and S. Anderson (1998), A new look at calibration and use of Eppley precision infrared radiometers. Part I: Theory and application, *Journal of Atmospheric and Oceanic Technology*, *15*(6), 1229-1242.

Fan, L., S.-I. Shin, Q. Liu, and Z. Liu (2013), Relative importance of tropical SST anomalies in forcing East Asian summer monsoon circulation, *Geophysical Research Letters*, *40*(10), 2471-2477.

Ferguson, C. R., and E. F. Wood (2010), An Evaluation of Satellite Remote Sensing Data Products for Land Surface Hydrology: Atmospheric Infrared Sounder*, *Journal of Hydrometeorology*, *11*(6), 1234-1262.

Foken, T., F. Wimmer, M. Mauder, C. Thomas, and C. Liebethal (2006), Some aspects of the energy balance closure problem, *Atmospheric Chemistry and Physics*, *6*, 4395-4402.

Foken, T. (2008), The energy balance closure problem: an overview, *Ecological Applications*, *18*(6), 1351-1367.

Fu, C. (2003), Potential impacts of human-induced land cover change on East Asia monsoon, *Global and Planetary Change*, *37*(3–4), 219-229.

Fu, Q., K. N. Liou, M. C. Cribb, T. P. Charlock, and A. Grossman (1997), Multiple scattering parameterization in thermal infrared radiative transfer, *Journal of the Atmospheric Sciences*, *54*(24), 2799-2812.

Gao, J., M. W. Williams, X. Fu, G. Wang, and T. Gong (2012), Spatiotemporal distribution of snow in eastern Tibet and the response to climate change, *Remote Sensing of Environment*, *121*(0), 1-9.

Gong, D.-Y., J. Yang, S.-J. Kim, Y. Gao, D. Guo, T. Zhou, and M. Hu (2011), Spring

Arctic Oscillation-East Asian summer monsoon connection through circulation changes over the western North Pacific, *Climate Dynamics*, *37*(11-12), 2199-2216.

Goswami, B. N., M. S. Madhusoodanan, C. P. Neema, and D. Sengupta (2006), A physical mechanism for North Atlantic SST influence on the Indian summer monsoon, *Geophysical Research Letters*, *33*(2), L02706.

Granger, C. W. (1969), Investigating causal relations by econometric models and cross-spectral methods, *Econometrica*, 424-438.

Gu, S., Y. H. Tang, M. Y. Du, T. Kato, Y. N. Li, X. Y. Cui, and X. A. Zhao (2003), Short-term variation of CO2 flux in relation to environmental controls in an alpine meadow on the Qinghai-Tibetan Plateau, *Journal of Geophysical Research: Atmospheres*, *108*(D21).

Gu, S., Y. H. Tang, X. Y. Cui, T. Kato, M. Y. Du, Y. N. Li, and X. Q. Zhao (2005), Energy exchange between the atmosphere and a meadow ecosystem on the Qinghai-Tibetan Plateau, *Agricultural and Forest Meteorology*, *129*(3-4), 175-185.

Gui, S., S. Liang, and L. Li (2010), Evaluation of satellite-estimated surface longwave radiation using ground-based observations, *Journal of Geophysical Research*, *115*(D18), D18214.

Hahn, D. G., and J. Shukla (1976), An apparent relationship between Eurasian snow cover and Indian monsoon rainfall, *Journal of Atmospheric Science*, *33*(12), 2461-2462.

Hakuba, M. Z., D. Folini, A. Sanchez-Lorenzo, and M. Wild (2013), Spatial representativeness of ground-based solar radiation measurements, *Journal of Geophysical Research: Atmospheres*, *118*(15), 8585-8597.

Harris, I., P. D. Jones, T. J. Osborn, and D. H. Lister (2014), Updated high-resolution grids of monthly climatic observations – the CRU TS3.10 Dataset, *International Journal of Climatology*, *34*(3), 623-642.

He, H., J. W. McGinnis, Z. Song, and M. Yanai (1987), Onset of the Asian summer monsoon in 1979 and the effect of the Tibetan Plateau, *Monthly Weather Review*, *115*(9), 1966-1995.

Huffman, G. J., R. F. Adler, D. T. Bolvin, and G. Gu (2009), Improving the global precipitation record: GPCP Version 2.1, *Geophysical Research Letters*, *36*.

Immerzeel, W. W., L. P. H. van Beek, and M. F. P. Bierkens (2010), Climate change will affect the Asian water towers, *Science*, *328*(5984), 1382-1385.

Jiang, B., and S. Liang (2013), Improved vegetation greenness increases summer atmospheric water vapor over Northern China, *Journal of Geophysical Research: Atmospheres*, *118*(15), 8129-8139.

Jiang, B., S. Liang, and W. Yuan (2015), Observational evidence for impacts of

vegetation change on local surface climate over northern China using the Granger Causality test, *Journal of Geophysical Research: Biogeosciences*, *120*, 1-12.

Jiménez, C., C. Prigent, and F. Aires (2009), Toward an estimation of global land surface heat fluxes from multisatellite observations, *Journal of Geophysical Research*, *114*(D6), D06305.

Jiménez, C., C. Prigent, B. Mueller, S. I. Seneviratne, M. F. McCabe, E. F. Wood, W. B. Rossow, G. Balsamo, A. K. Betts, P. A. Dirmeyer, J. B. Fisher, M. Jung, M. Kanamitsu, R. H. Reichle, M. Reichstein, M. Rodell, J. Sheffield, K. Tu, and K. Wang (2011), Global intercomparison of 12 land surface heat flux estimates, *Journal of Geophysical Research*, *116*(D2), D02102.

Jung, M., M. Reichstein, and A. Bondeau (2009), Towards global empirical upscaling of FLUXNET eddy covariance observations: validation of a model tree ensemble approach using a biosphere model, *Biogeosciences*, *6*(10), 2001-2013.

Jung, M., M. Reichstein, H. A. Margolis, A. Cescatti, A. D. Richardson, M. A. Arain, A. Arneth, C. Bernhofer, D. Bonal, J. Chen, D. Gianelle, N. Gobron, G. Kiely, W. Kutsch, G. Lasslop, B. E. Law, A. Lindroth, L. Merbold, L. Montagnani, E. J. Moors, D. Papale, M. Sottocornola, F. Vaccari, and C. Williams (2011), Global patterns of land-atmosphere fluxes of carbon dioxide, latent heat, and sensible heat derived from eddy covariance, satellite, and meteorological observations, *Journal of Geophysical Research*, *116*, G00J07.

Kajikawa, Y., T. Yasunari, H. Fujinami, and S. Yoshida (2012), Advanced Asian summer monsoon onset in recent decades, *Geophysical Research Letters*, *39*(3).

Kalnay, E., M. Kanamitsu, R. Kistler, W. Collins, D. Deaven, L. Gandin, M. Iredell, S. Saha, G. White, J. Woollen, Y. Zhu, A. Leetmaa, R. Reynolds, M. Chelliah, W. Ebisuzaki, W. Higgins, J. Janowiak, K. C. Mo, C. Ropelewski, J. Wang, R. Jenne, and D. Joseph (1996), The NCEP/NCAR 40-year reanalysis project, *Bulletin of the American Meteorological Society*, *77*(3), 437-471.

Kambezidis, H. D., D. G. Kaskaoutis, S. K. Kharol, K. K. Moorthy, S. K. Satheesh, M. C. R. Kalapureddy, K. V. S. Badarinath, A. R. Sharma, and M. Wild (2012), Multi-decadal variation of the net downward shortwave radiation over south Asia: The solar dimming effect, *Atmospheric Environment*, *50*(0), 360-372.

Kanamitsu, M., W. Ebisuzaki, J. Woollen, S.-K. Yang, J. J. Hnilo, M. Fiorino, and G. L. Potter (2002), NCEP–DOE AMIP-II Reanalysis (R-2), *Bulletin of the American Meteorological Society*, *83*(11), 1631-1643.

Kaufmann, R. K., and D. I. Stern (1997), Evidence for human influence on climate from hemispheric temperature relations, *Nature*, *388*(6637), 39-44.

Kiehl, J. T., and K. E. Trenberth (1997), Earth's annual global mean energy budget, *Bulletin of the American Meteorological Society*, *78*(2), 197-208.

Kim, J., A. Miyata, and G. Yu (2009), AsiaFlux-sustaining ecosystems and people through resilience thinking, paper presented at WCC-3 Climate Sense, Tudor Rose.

Koike, T. (2004), The Coordinated Enhanced Observing Period-an initial step for integrated global water cycle observation, *WMO Bulletin*, *53*(2), 115-121.

Koren, V., J. Schaake, K. Mitchell, Q. Y. Duan, F. Chen, and J. M. Baker (1999), A parameterization of snowpack and frozen ground intended for NCEP weather and climate models, *Journal of Geophysical Research: Atmospheres*, *104*(D16), 19569-19585.

Koster, R. D., and M. J. Suarez (1996), Energy and water balance calculations in the Mosaic LSM, NASA Tech. Memo. 104606, Vol. 9, NASA Goddard Space Flight Center, Greenbelt.

Koster, R. D., M. J. Suarez, A. Ducharne, M. Stieglitz, and P. Kumar (2000), A catchment-based approach to modeling land surface processes in a general circulation model: 1. Model structure, *Journal of Geophysical Research: Atmospheres*, *105*(D20), 24809-24822.

Kumar, K. K., B. Rajagopalan, and M. A. Cane (1999), On the weakening relationship between the Indian monsoon and ENSO, *Science*, *284*(5423), 2156-2159.

Kumar, K. K., B. Rajagopalan, M. Hoerling, G. Bates, and M. Cane (2006), Unraveling the mystery of Indian monsoon failure during El Nino, *Science*, *314*(5796), 115-119.

Kutzbach, J. E., W. L. Prell, and W. F. Ruddiman (1993), Sensitivity of Eurasian climate to surface uplift of the Tibetan Plateau, *Journal of Geology*, *101*(2), 177-190.

Lau, K. M., M. K. Kim, and K. M. Kim (2006), Asian summer monsoon anomalies induced by aerosol direct forcing: the role of the Tibetan Plateau, *Climate Dynamics*, *26*(7-8), 855-864.

Lau, K. M., and K. M. Kim (2006), Observational relationships between aerosol and Asian monsoon rainfall, and circulation, *Geophysical Research Letters*, *33*(21), L21810.

Li, Z., C. H. Whitlock, and T. P. Charlock (1995), Assessment of the global monthly mean surface insolation estimated from satellite measurements using global energy balance archive data, *Journal of Climate*, *8*(2), 315-328.

Li, Z., M. C. Cribb, F.-L. Chang, A. Trishchenko, and Y. Luo (2005), Natural variability and sampling errors in solar radiation measurements for model validation over the Atmospheric Radiation Measurement Southern Great Plains region, *Journal of Geophysical Research: Atmospheres*, *110*(D15), D15S19.

Liang, S., K. Wang, X. Zhang, and M. Wild (2010), Review on estimation of land surface radiation and energy budgets from ground measurement, remote sensing and model simulations, *IEEE Journal of Selected Topics in Applied Earth Observations and Remote Sensing*, *3*(3), 225-240.

Liang, S., X. Zhao, S. Liu, W. Yuan, X. Cheng, Z. Xiao, X. Zhang, Q. Liu, J. Cheng, H. Tang, Y. Qu, Y. Bai, Y. Qu, H. Ren, K. Yu, and J. Townshend (2013a), A long-term Global LAnd Surface Satellite (GLASS) dataset for environmental studies, *International Journal of Digital Earth*, *6*, 5-33.

Liang, S., X. Zhang, T. He, J. Cheng, and D. Wang (2013b), Remote sensing of Earth surface radiation budget, in *Remote Sensing of Land Surface Turbulent Fluxes and Soil Surface moisture Content: State of the Art*, edited by G. P. Petropoulos, pp. 125-165, CRC Press, Boca Raton, Florida.

Liebmann, B., and C. A. Smith (1996), Description of a complete (interpolated) outgoing longwave radiation dataset, *Bulletin of the American Meteorological Society*, *77*(6), 1275-1277.

Liu, B. H., M. Xu, M. Henderson, Y. Qi, and Y. Q. Li (2004), Taking China's temperature: Daily range, warming trends, and regional variations, 1955-2000, *Journal of Climate*, *17*(22), 4453-4462.

Liu, X., and M. Yanai (2002), Influence of Eurasian spring snow cover on Asian summer rainfall, *International Journal of Climatology*, *22*(9), 1075-1089.

Liu, Y., G. Wu, J. Hong, B. Dong, A. Duan, Q. Bao, and L. Zhou (2012a), Revisiting Asian monsoon formation and change associated with Tibetan Plateau forcing: II. Change, *Climate Dynamics*, *39*(5), 1183-1195.

Liu, Y., T. Hiyama, T. Yasunari, and H. Tanaka (2012b), A nonparametric approach to estimating terrestrial evaporation: Validation in eddy covariance sites, *Agricultural and Forest Meteorology*, *157*, 49-59.

Lu, R., B. Dong, and H. Ding (2006), Impact of the Atlantic Multidecadal Oscillation on the Asian summer monsoon, *Geophysical Research Letters*, *33*(24), L24701.

Luo, Y., H. Wang, R. Zhang, W. Qian, and Z. Luo (2012), Comparison of rainfall characteristics and convective properties of monsoon precipitation systems over South China and the Yangtze and Huai River Basin, *Journal of Climate*, *26*(1), 110-132.

Ma, Y., L. Zhong, Z. Su, H. Ishikawa, M. Menenti, and T. Koike (2006), Determination of regional distributions and seasonal variations of land surface heat fluxes from Landsat-7 Enhanced Thematic Mapper data over the central Tibetan Plateau area, *Journal of Geophysical Research*, *111*(D10), D10305.

Ma, Y., L. Zhong, B. Wang, X. Chen, W. Ma, and M. Li (2011), Determination of land surface heat fluxes over heterogeneous landscape of the Tibetan Plateau by using the MODIS and in-situ data, *Atmospheric Chemistry and Physics*, *11*(7), 19617-19638.

Mao, J., X. Shi, L. Ma, D. P. Kaiser, Q. Li, and P. E. Thornton (2010), Assessment of reanalysis daily extreme temperatures with China’s homogenized historical dataset during 1979–2001 using probability density functions, *Journal of Climate*, *23*(24), 6605-6623.

Marty, C., R. Philipona, C. Frohlich, and A. Ohmura (2002), Altitude dependence of surface radiation fluxes and cloud forcing in the alps: Results from the alpine surface radiation budget network, *Theoretical and Applied Climatology*, *72*(3), 137.

Meehl, G. A. (1994), Influence of the land surface in the Asian summer monsoon: External conditions versus internal feedbacks, *Journal of Climate*, *7*(7), 1033-1049.

Meng, J., R. Yang, H. Wei, M. Ek, G. Gayno, P. Xie, and K. Mitchell (2012), The land surface analysis in the NCEP Climate Forecast System Reanalysis, *Journal of Hydrometeorology*, *13*(5), 1621-1630.

Menon, S., J. Hansen, L. Nazarenko, and Y. F. Luo (2002), Climate effects of black carbon aerosols in China and India, *Science*, *297*(5590), 2250-2253.

Miralles, D. G., R. A. M. De Jeu, J. H. Gash, T. R. H. Holmes, and A. J. Dolman (2011a), Magnitude and variability of land evaporation and its components at the global scale, *Hydrology and Earth System Sciences*, *15*(3), 967-981.

Miralles, D. G., T. R. H. Holmes, R. A. M. De Jeu, J. H. Gash, A. G. C. A. Meesters, and A. J. Dolman (2011b), Global land-surface evaporation estimated from satellite-based observations, *Hydrology and Earth System Sciences*, *15*(2), 453-469.

Miralles, D. G., M. J. van den Berg, J. H. Gash, R. M. Parinussa, R. A. M. de Jeu, H. E. Beck, T. R. H. Holmes, C. Jiménez, N. E. C. Verhoest, W. A. Dorigo, A. J. Teuling, and A. Johannes Dolman (2014), El Niño–La Niña cycle and recent trends in continental evaporation, *Nature Climate Change*, *4*(2), 122-126.

Mokhov, I. I., D. A. Smirnov, P. I. Nakonechny, S. S. Kozlenko, E. P. Seleznev, and J. Kurths (2011), Alternating mutual influence of El-Niño/Southern Oscillation and Indian monsoon, *Geophysical Research Letters*, *38*(8), L00F04.

Mosedale, T. J., D. B. Stephenson, M. Collins, and T. C. Mills (2006), Granger causality of coupled climate processes: Ocean feedback on the North Atlantic oscillation, *Journal of Climate*, *19*(7), 1182-1194.

Mu, Q., F. A. Heinsch, M. Zhao, and S. W. Running (2007), Development of a global evapotranspiration algorithm based on MODIS and global meteorology data, *Remote Sensing of Environment*, *111*(4), 519-536.

Mu, Q., M. Zhao, and S. W. Running (2011), Improvements to a MODIS global terrestrial evapotranspiration algorithm, *Remote Sensing of Environment*, *115*(8), 1781-1800.

Mueller, B., M. Hirschi, C. Jimenez, P. Ciais, P. A. Dirmeyer, A. J. Dolman, J. B. Fisher, M. Jung, F. Ludwig, F. Maignan, D. Miralles, M. F. McCabe, M. Reichstein, J. Sheffield, K. C. Wang, E. F. Wood, Y. Zhang, and S. I. Seneviratne (2013), Benchmark products for land evapotranspiration: LandFlux-EVAL multi-data set synthesis, *Hydrology and Earth System Sciences*, *17*, 3707-3720.

Mueller, B., and S. I. Seneviratne (2014), Systematic land climate and evapotranspiration biases in CMIP5 simulations, *Geophysical Research Letters*, *41*(1), 128-134.

Oleson, K., Y. Dai, G. Bonan, M. Bosilovichm, R. Dickinson, P. Dirmeyer, F. Hoffman, P. Houser, S. Levis, G.-Y. Niu, P. Thornton, M. Vertenstein, Z.-L. Yang, and X. Zeng (2004), Technical Description of the Community Land Model (CLM), Technical Report NCAR/TN-461+STR, National Center for Atmospheric Research, Boulder, CO 80307-3000, USA.

Onogi, K., J. Tsutsui, H. Koide, M. Sakamoto, S. Kobayashi, H. Hatsushika, T. Matsumoto, N. Yamazaki, H. Kamahori, K. Takahashi, S. Kadokura, K. Wada, K. Kato, R. Oyama, T. Ose, N. Mannoji, and R. Taira (2007), The JRA-25 reanalysis, *Journal of the Meteorological Society of Japan*, *85*(3), 369-432.

Piao, S., J. Fang, L. Zhou, Q. Guo, M. Henderson, W. Ji, Y. Li, and S. Tao (2003), Interannual variations of monthly and seasonal normalized difference vegetation index (NDVI) in China from 1982 to 1999, *Journal of Geophysical Research: Atmospheres*, *108*(D14), 4401.

Piao, S., Z. Shen, S. Peng, L. Zhou, H. Liu, Y. Ma, K. Tan, J. Fang, P. Ciais, P. Friedlingstein, Y. Huang, Y. Yu, T. Zhang, J. Li, Y. Ding, and C. Liu (2010), The impacts of climate change on water resources and agriculture in China, *Nature*, *467*(7311), 43-51.

Pinker, R. T., and J. A. Ewing (1985), Modeling surface solar radiation: model formulation and validation, *Journal of Climate and Applied Meteorology*, *24*(5), 389-401.

Pinker, R. T., and I. Laszlo (1992), Modeling surface solar irradiance for satellite applications on a global scale, *Journal of Applied Meteorology*, *31*(2), 194-211.

Pohl, C., and J. L. Van Genderen (1998), Review article multisensor image fusion in remote sensing: concepts, methods and applications, *International Journal of Remote Sensing*, *19*(5), 823-854.

Pu, Z., and L. Xu (2009), MODIS/Terra observed snow cover over the Tibet Plateau: Distribution, variation and possible connection with the East Asian summer monsoon (EASM), *Theoretical and Applied Climatology*, *97*(3-4), 265-278.

Qian, Y., M. G. Flanner, L. R. Leung, and W. Wang (2011), Sensitivity studies on the impacts of Tibetan Plateau snowpack pollution on the Asian hydrological cycle and monsoon climate, *Atmos. Chem. Phys.*, *11*(5), 1929-1948.

Qin, J., K. Yang, S. Liang, and X. Guo (2009), The altitudinal dependence of recent rapid warming over the Tibetan Plateau, *Climatic Change*, *97*(1), 321-327.

Qin, J., K. Yang, S. Liang, H. Zhang, Y. Ma, X. Guo, and Z. Chen (2011), Evaluation of surface albedo from GEWEX-SRB and ISCCP-FD data against validated MODIS product over the Tibetan Plateau, *Journal of Geophysical Research*, *116*(D24), D24116.

Qiu, J. (2008), China: The third pole, *Nature*, *454*(7203), 393-396.

Qu, X., and A. Hall (2014), On the persistent spread in snow-albedo feedback, *Climate Dynamics*, *42*(1-2), 69-81.

R (2012), *R: A language and environment for statistical computing. R Foundation for Statistical Computing*, Vienna, Austria.

Raftery, A. E., T. Gneiting, F. Balabdaoui, and M. Polakowski (2005), Using Bayesian model averaging to calibrate forecast ensembles, *Monthly Weather Review*, *133*(5), 1155-1174.

Rajagopalan, B., and P. Molnar (2013), Signatures of Tibetan Plateau heating on Indian summer monsoon rainfall variability, *Journal of Geophysical Research*, *118*(3), 1170-1178.

Rajagopalan, B., and P. Molnar (2014), Combining regional moist static energy and ENSO for forecasting of early and late season Indian monsoon rainfall and its extremes, *Geophysical Research Letters*, *41*(12), 2014GL060429.

Rajeevan, M., J. Bhate, J. A. Kale, and B. Lal (2006), High resolution daily gridded rainfall data for the Indian region: Analysis of break and active monsoon spells, *Current Science*, *91*(3), 296-306.

Ramanathan, V., P. J. Crutzen, J. T. Kiehl, and D. Rosenfeld (2001), Atmosphere - Aerosols, climate, and the hydrological cycle, *Science*, *294*(5549), 2119-2124.

Ramanathan, V., C. Chung, D. Kim, T. Bettge, L. Buja, J. T. Kiehl, W. M. Washington, Q. Fu, D. R. Sikka, and M. Wild (2005), Atmospheric brown clouds: Impacts on South Asian climate and hydrological cycle, *Proceedings of the National Academy of Sciences of the United States of America*, *102*(15), 5326-5333.

Rienecker, M. M., M. J. Suarez, R. Gelaro, R. Todling, J. Bacmeister, E. Liu, M. G. Bosilovich, S. D. Schubert, L. Takacs, G.-K. Kim, S. Bloom, J. Chen, D. Collins, A. Conaty, A. da Silva, W. Gu, J. Joiner, R. D. Koster, R. Lucchesi, A. Molod, T. Owens, S. Pawson, P. Pegion, C. R. Redder, R. Reichle, F. R. Robertson, A. G. Ruddick, M. Sienkiewicz, and J. Woollen (2011), MERRA: NASAs modern-era retrospective analysis for research and applications, *Journal of Climate*, *24*(14), 3624-3648.

Robinson, D. A., K. F. Dewey, and R. R. Heim (1993), Global snow cover monitoring: An update, *Bulletin of the American Meteorological Society*, *74*(9), 1689-1696.

Rodell, M., P. R. Houser, U. Jambor, J. Gottschalck, K. Mitchell, C. J. Meng, K. Arsenault, B. Cosgrove, J. Radakovich, M. Bosilovich, J. K. Entin*, J. P. Walker, D. Lohmann, and D. Toll (2004), The global land data assimilation system, *Bulletin of the American Meteorological Society*, *85*(3), 381-394.

Rossow, W. B., and E. N. Dueñas (2004), The International Satellite Cloud Climatology

Project (ISCCP) web site: An online resource for research, *Bulletin of the American Meteorological Society*, *85*(2), 167-172.

Saha, S., S. Moorthi, H.-L. Pan, X. Wu, J. Wang, S. Nadiga, P. Tripp, R. Kistler, J. Woollen, D. Behringer, H. Liu, D. Stokes, R. Grumbine, G. Gayno, J. Wang, Y.-T. Hou, H.-Y. Chuang, H.-M. H. Juang, J. Sela, M. Iredell, R. Treadon, D. Kleist, P. Van Delst, D. Keyser, J. Derber, M. Ek, J. Meng, H. Wei, R. Yang, S. Lord, H. Van Den Dool, A. Kumar, W. Wang, C. Long, M. Chelliah, Y. Xue, B. Huang, J.-K. Schemm, W. Ebisuzaki, R. Lin, P. Xie, M. Chen, S. Zhou, W. Higgins, C.-Z. Zou, Q. Liu, Y. Chen, Y. Han, L. Cucurull, R. W. Reynolds, G. Rutledge, and M. Goldberg (2010), The NCEP Climate Forecast System Reanalysis, *Bulletin of the American Meteorological Society*, *91*(8), 1015-1057.

Salama, M. S., R. Van der Velde, L. Zhong, Y. M. Ma, M. Ofwono, and Z. B. Su (2012), Decadal variations of land surface temperature anomalies observed over the Tibetan Plateau by the Special Sensor Microwave Imager (SSM/I) from 1987 to 2008, *Climatic Change*, *114*(3-4), 769-781.

Sato, N., P. J. Sellers, D. A. Randall, E. K. Schneider, J. Shukla, J. L. Kinter, Y. T. Hou, and E. Albertazzi (1989), Effects of implementing the Simple Biosphere Model in a general circulation model, *Journal of the Atmospheric Sciences*, *46*(18), 2757-2782.

Schneider, U., A. Becker, P. Finger, A. Meyer-Christoffer, B. Rudolf, and M. Ziese (2011), GPCC full data reanalysis version 6.0 at 0.5°: Monthly land-surface precipitation from rain-gauges built on GTS-based and historic data. doi:10.5676/DWD_GPCC/FD_M_V6_050, edited.

Sellers, P. J., Y. Mintz, Y. C. Sud, and A. Dalcher (1986), A Simple Biosphere Model (SIB) for use within heneral circulation models, *Journal of the Atmospheric Sciences*, *43*(6), 505-531.

Sellers, P. J., D. A. Randall, G. J. Collatz, J. A. Berry, C. B. Field, D. A. Dazlich, C. Zhang, G. D. Collelo, and L. Bounoua (1996), A revised land surface parameterization (SiB2) for atmospheric GCMS. Part I: Model formulation, *Journal of Climate*, *9*(4), 676-705.

Shi, G. Y., T. Hayasaka, A. Ohmura, Z. H. Chen, B. Wang, J. Q. Zhao, H. Z. Che, and L. Xu (2008), Data quality assessment and the long-term trend of ground solar radiation in China, *Journal of Applied Meteorology and Climatology*, *47*(4), 1006-1016.

Shi, Q., and S. Liang (2013a), Characterizing the surface radiation budget over the Tibetan Plateau with ground-measured, reanalysis, and remote sensing data sets: 1. Methodology, *Journal of Geophysical Research: Atmospheres*, *118*(17), 9642-9657.

Shi, Q., and S. Liang (2013b), Characterizing the surface radiation budget over the Tibetan Plateau with ground-measured, reanalysis, and remote sensing data sets: 2. Spatiotemporal analysis, *Journal of Geophysical Research: Atmospheres*, *118*(16), 8921-8934.

Shi, Q., and S. Liang (2014), Surface-sensible and latent heat fluxes over the Tibetan Plateau from ground measurements, reanalysis, and satellite data, *Atmospheric Chemistry and Physics*, *14*(11), 5659-5677.

Shi, Q., and S. Liang (2015a), Biases of the surface energy budget over the Tibetan Plateau simulated by CMIP5 models and their possible causes and consequences, *Submitted to Atmospheric Sciences Letters*.

Shi, Q., and S. Liang (2015b), Assessing the impacts of the spring Tibetan Plateau sensible heat flux on Asian summer monsoon rainfall using observational and reanalysis data, *Submitted to Journal of Climate*.

Shukla, R. P., K. C. Tripathi, A. C. Pandey, and I. M. L. Das (2011), Prediction of Indian summer monsoon rainfall using Nino indices: A neural network approach, *Atmospheric Research*, *102*(1-2), 99-109.

Smith, T. M., R. W. Reynolds, T. C. Peterson, and J. Lawrimore (2008), Improvements to NOAA's historical merged land–ocean surface temperature analysis (1880–2006), *Journal of Climate*, *21*(10), 2283-2296.

Sperber, K. R., H. Annamalai, I. S. Kang, A. Kitoh, A. Moise, A. Turner, B. Wang, and T. Zhou (2013), The Asian summer monsoon: an intercomparison of CMIP5 vs. CMIP3 simulations of the late 20th century, *Climate Dynamics*, *41*(9-10), 2711-2744.

Stackhouse, P. W., S. K. Gupta, S. J. Cox, T. Zhang, J. C. Mikovitz, and L. M. Hinkelman (2011), The NASA/GEWEX surface radiation budget release 3.0: 24.5-year dataset, *GEWEX News*, *21*(1), 10-12.

Stephens, G. L., J. Li, M. Wild, C. A. Clayson, N. Loeb, S. Kato, T. L'Ecuyer, P. W. Stackhouse, M. Lebsock, and T. Andrews (2012), An update on Earth's energy balance in light of the latest global observations, *Nature Geoscience*, *5*(10), 691-696.

Stevens, B., and S. Schwartz (2012), Observing and modeling Earth's energy flows, *Surveys in Geophysics*, *33*(3), 779-816.

Stieglitz, M., A. Ducharne, R. Koster, and M. Suarez (2001), The impact of detailed snow physics on the simulation of snow cover and subsurface thermodynamics at continental scales, *Journal of Hydrometeorology*, *2*(3), 228-242.

Su, F., X. Duan, D. Chen, Z. Hao, and L. Cuo (2013), Evaluation of the global climate models in the CMIP5 over the Tibetan Plateau, *Journal of Climate*, *26*(10), 3187-3208.

Tang, W. J., K. Yang, J. Qin, C. C. K. Cheng, and J. He (2011), Solar radiation trend across China in recent decades: A revisit with quality-controlled data, *Atmospheric Chemistry and Physics*, *11*(1), 393-406.

Taylor, K. E., R. J. Stouffer, and G. A. Meehl (2012), An overview of CMIP5 and the experiment design, *Bull. Am. Meteorol. Soc.*, *93*(4), 485-498.

Teuling, A. J., and S. I. Seneviratne (2008), Contrasting spectral changes limit albedo impact on land-atmosphere coupling during the 2003 European heat wave, *Geophysical Research Letters*, *35*(3), L03401.

Tian, H. Q., J. M. Melillo, D. W. Kicklighter, S. F. Pan, J. Y. Liu, A. D. McGuire, and B. Moore (2003), Regional carbon dynamics in monsoon Asia and its implications for the global carbon cycle, *Global and Planetary Change*, *37*(3-4), 201-217.

Trenberth, K. E., J. T. Fasullo, and J. Kiehl (2009), Earth's global energy budget, *Bulletin of the American Meteorological Society*, *90*(3), 311-323.

Tucker, C. J. (1979), Red and photographic infrared linear combinations for monitoring vegetation, *Remote Sensing of Environment*, *8*(2), 127-150.

Tucker, C. J., J. E. Pinzon, M. E. Brown, D. A. Slayback, E. W. Pak, R. Mahoney, E. F. Vermote, and N. El Saleous (2005), An extended AVHRR 8-km NDVI dataset compatible with MODIS and SPOT vegetation NDVI data, *International Journal of Remote Sensing*, *26*(20), 4485-4498.

Turner, A. G., and H. Annamalai (2012), Climate change and the South Asian summer monsoon, *Nature Climate Change*, *2*(8), 587-595.

Uppala, S. M., P. W. KÅllberg, A. J. Simmons, U. Andrae, V. D. C. Bechtold, M. Fiorino, J. K. Gibson, J. Haseler, A. Hernandez, G. A. Kelly, X. Li, K. Onogi, S. Saarinen, N. Sokka, R. P. Allan, E. Andersson, K. Arpe, M. A. Balmaseda, A. C. M. Beljaars, L. V. D. Berg, J. Bidlot, N. Bormann, S. Caires, F. Chevallier, A. Dethof, M. Dragosavac, M. Fisher, M. Fuentes, S. Hagemann, E. Hólm, B. J. Hoskins, L. Isaksen, P. A. E. M. Janssen, R. Jenne, A. P. McNally, J. F. Mahfouf, J. J. Morcrette, N. A. Rayner, R. W. Saunders, P. Simon, A. Sterl, K. E. Trenberth, A. Untch, D. Vasiljevic, P. Viterbo, and J. Woollen (2005), The ERA-40 re-analysis, *Quarterly Journal of the Royal Meteorological Society*, *131*(612), 2961-3012.

Vapnik, V. (1999), *The Nature of Statistical Learning Theory*, Springer, New York.

Vickers, D., and L. Mahrt (1997), Quality control and flux sampling problems for tower and aircraft data, *Journal of Atmospheric and Oceanic Technology*, *14*(3), 512-526.

Vinoj, V., P. J. Rasch, H. Wang, J.-H. Yoon, P.-L. Ma, K. Landu, and B. Singh (2014), Short-term modulation of Indian summer monsoon rainfall by West Asian dust, *Nature Geoscience*, *7*(4), 308-313.

Vinukollu, R. K., E. F. Wood, C. R. Ferguson, and J. B. Fisher (2011a), Global estimates of evapotranspiration for climate studies using multi-sensor remote sensing data: Evaluation of three process-based approaches, *Remote Sensing of Environment*, *115*(3), 801-823.

Vinukollu, R. K., R. Meynadier, J. Sheffield, and E. F. Wood (2011b), Multi-model, multi-sensor estimates of global evapotranspiration: climatology, uncertainties and trends,

Hydrological Processes, *25*(26), 3993-4010.

Viterbo, P., and A. C. M. Beljaars (1995), An improved land surface parameterization scheme in the ECMWF Model and its validation, *Journal of Climate*, *8*(11), 2716-2748.

Viterbo, P., and A. K. Betts (1999), Impact on ECMWF forecasts of changes to the albedo of the boreal forests in the presence of snow, *Journal of Geophysical Research: Atmospheres*, *104*(D22), 27803-27810.

Wang, A., and X. Zeng (2012), Evaluation of multireanalysis products with in situ observations over the Tibetan Plateau, *Journal of Geophysical Research*, *117*(D5), D05102.

Wang, B., and Z. Fan (1999), Choice of South Asian summer monsoon indices, *Bulletin of the American Meteorological Society*, *80*(4), 629-638.

Wang, B., R. G. Wu, and K. M. Lau (2001), Interannual variability of the Asian summer monsoon: Contrasts between the Indian and the western North Pacific-East Asian monsoons, *Journal of Climate*, *14*(20), 4073-4090.

Wang, B., and LinHo (2002), Rainy season of the Asian-Pacific summer monsoon, *Journal of Climate*, *15*(4), 386-398.

Wang, B., Z. Wu, J. Li, J. Liu, C.-P. Chang, Y. Ding, and G. Wu (2008a), How to measure the strength of the East Asian summer monsoon, *Journal of Climate*, *21*(17), 4449-4463.

Wang, B., J. Yang, and T. Zhou (2008b), Interdecadal changes in the major modes of Asian–Australian monsoon variability: Strengthening relationship with ENSO since the late 1970s, *Journal of Climate*, *21*(8), 1771-1789.

Wang, B., Q. Bao, B. Hoskins, G. Wu, and Y. Liu (2008c), Tibetan Plateau warming and precipitation changes in East Asia, *Geophysical Research Letters*, *35*(14), L14702.

Wang, B., H.-J. Kim, K. Kikuchi, and A. Kitoh (2011a), Diagnostic metrics for evaluation of annual and diurnal cycles, *Climate Dynamics*, *37*(5-6), 941-955.

Wang, B., B. Xiang, and J.-Y. Lee (2013a), Subtropical High predictability establishes a promising way for monsoon and tropical storm predictions, *Proceedings of the National Academy of Sciences of the United States of America*, *110*(8), 2718-2722.

Wang, K., Z. Wan, P. Wang, M. Sparrow, J. Liu, X. Zhou, and S. Haginoya (2005), Estimation of surface long wave radiation and broadband emissivity using Moderate Resolution Imaging Spectroradiometer (MODIS) land surface temperature/emissivity products, *Journal of Geophysical Research*, *110*(D11), D11109.

Wang, K., Z. Li, and M. Cribb (2006), Estimation of evaporative fraction from a combination of day and night land surface temperatures and NDVI: A new method to determine the Priestley-Taylor parameter, *Remote Sensing of Environment*, *102*(3-4), 293-

305.

Wang, K., P. Wang, Z. Li, M. Cribb, and M. Sparrow (2007), A simple method to estimate actual evapotranspiration from a combination of net radiation, vegetation index, and temperature, *Journal of Geophysical Research*, *112*(D15), D15107.

Wang, K., and S. Liang (2008), An improved method for estimating global evapotranspiration based on satellite determination of surface net radiation, vegetation index, temperature, and soil moisture, *Journal of Hydrometeorology*, *9*(4), 712-727.

Wang, K., and S. Liang (2009), Global atmospheric downward longwave radiation over land surface under all-sky conditions from 1973 to 2008, *Journal of Geophysical Research: Atmospheres*, *114*(D19), D19101.

Wang, K., and R. E. Dickinson (2012), A review of global terrestrial evapotranspiration: observation, modeling, climatology, and climatic variability, *Reviews of Geophysics*, *50*(2), RG2005.

Wang, M., S. Zhou, and A. Duan (2012), Trend in the atmospheric heat source over the central and eastern Tibetan Plateau during recent decades: Comparison of observations and reanalysis data, *Chinese Science Bulletin*, *57*(5), 548-557.

Wang, W., P. Xie, S.-H. Yoo, Y. Xue, A. Kumar, and X. Wu (2011b), An assessment of the surface climate in the NCEP climate forecast system reanalysis, *Climate Dynamics*, *37*(7), 1601-1620.

Wang, Z., A. Duan, and G. Wu (2013b), Time-lagged impact of spring sensible heat over the Tibetan Plateau on the summer rainfall anomaly in East China: Case studies using the WRF model, *Climate Dynamics*, 1-14.

Webb, E. K., G. I. Pearman, and R. Leuning (1980), Correction of flux measurements for density effects due to heat and water vapour transfer, *Quarterly Journal of the Royal Meteorological Society*, *106*(447), 85-100.

Wielicki, B. A., B. R. Barkstrom, E. F. Harrison, R. B. Lee III, G. Louis Smith, and J. E. Cooper (1996), Clouds and the Earth's Radiant Energy System (CERES): An earth observing system experiment, *Bulletin of the American Meteorological Society*, *77*(5), 853-868.

Wild, M. (2012), Enlightening global dimming and brightening, *Bulletin of the American Meteorological Society*, *93*(1), 27-37.

Wild, M., D. Folini, C. Schaer, N. Loeb, E. G. Dutton, and G. Koenig-Langlo (2013), The global energy balance from a surface perspective, *Climate Dynamics*, *40*(11-12), 3107-3134.

Wild, M., D. Folini, M. Hakuba, C. Schär, S. Seneviratne, S. Kato, D. Rutan, C. Ammann, E. Wood, and G. König-Langlo (2014), The energy balance over land and

oceans: an assessment based on direct observations and CMIP5 climate models, *Climate Dynamics*, 1-37.

WMO (1981), *Meteorological aspects of utilization of solar radiation as an energy source, WMO 557*, 273 pp., Switzerland, Geneva.

Wohlfahrt, G., A. Haslwanter, L. Hörtnagl, R. L. Jasoni, L. F. Fenstermaker, J. A. Arnone Iii, and A. Hammerle (2009), On the consequences of the energy imbalance for calculating surface conductance to water vapour, *Agricultural and Forest Meteorology*, *149*(9), 1556-1559.

Wonsick, M. M., and R. T. Pinker (2014a), The radiative environment of the Tibetan Plateau, *International Journal of Climatology*, *34*(7), 2153-2162.

Wonsick, M. M., R. T. Pinker, and Y. Ma (2014b), Investigation of the "elevated heat pump" hypothesis of the Asian monsoon using satellite observations, *Atmospheric Chemistry and Physics*, *14*(16), 8749-8761.

Wu, G., Y. Liu, Q. Zhang, A. Duan, T. Wang, R. Wan, X. Liu, W. Li, Z. Wang, and X. Liang (2007), The influence of mechanical and thermal forcing by the Tibetan Plateau on Asian climate, *Journal of Hydrometeorology*, *8*(4), 770-789.

Wu, G., Y. Liu, B. He, Q. Bao, A. Duan, and F. Jin (2012a), Thermal controls on the Asian summer monsoon, *Scientific Reports*, *2*, 404.

Wu, G., A. Duan, Y. Liu, J. Mao, R. Ren, Q. Bao, B. He, B. Liu, and W. Hu (2015), Tibetan Plateau climate dynamics: recent research progress and outlook, *National Science Review*, *2*(1), 100-116.

Wu, H., X. Zhang, S. Liang, H. Yang, and G. Zhou (2012b), Estimation of clear-sky land surface longwave radiation from MODIS data products by merging multiple models, *Journal of Geophysical Research: Atmospheres*, *117*(D22), D22107.

Wu, Z., B. Wang, J. Li, and F.-F. Jin (2009), An empirical seasonal prediction model of the East Asian summer monsoon using ENSO and NAO, *Journal of Geophysical Research*, *114*.

Xie, P., and P. A. Arkin (1997), Global precipitation: A 17-year monthly analysis based on gauge observations, satellite estimates, and numerical model outputs, *Bulletin of the American Meteorological Society*, *78*(11), 2539-2558.

Xie, P., M. Chen, S. Yang, A. Yatagai, T. Hayasaka, Y. Fukushima, and C. Liu (2007), A gauge-based analysis of daily precipitation over East Asia, *Journal of Hydrometeorology*, *8*(3), 607-626.

Xue, B.-L., L. Wang, X. Li, K. Yang, D. Chen, and L. Sun (2013), Evaluation of evapotranspiration estimates for two river basins on the Tibetan Plateau by a water balance method, *Journal of Hydrology*, *492*(0), 290-297.

Yanai, M., and C. F. Li (1994), Mechanism of heating and the boundary layer over the Tibetan Plateau, *Monthly Weather Review*, *122*(2), 305-323.

Yanai, M. H., C. F. Li, and Z. S. Song (1992), Seasonal heating of the Tibetan Plateau and its effects on the evolution of the Asian summer monsoon, *Journal of the Meteorological Society of Japan*, *70*(1B), 319-351.

Yang, J., Q. Liu, and Z. Liu (2010), Linking observations of the Asian monsoon to the Indian Ocean SST: Possible roles of Indian Ocean basin mode and dipole mode, *Journal of Climate*, *23*(21), 5889-5902.

Yang, K., T. Koike, P. Stackhouse, C. Mikovitz, and S. J. Cox (2006), An assessment of satellite surface radiation products for highlands with Tibet instrumental data, *Geophysical Research Letters*, *33*(22), L22403.

Yang, K., T. Koike, H. Ishikawa, J. Kim, X. Li, H. Liu, S. Liu, Y. Ma, and J. Wang (2008a), Turbulent flux transfer over bare-soil surfaces: characteristics and parameterization, *Journal of Applied Meteorology and Climatology*, *47*(1), 276-290.

Yang, K., Y. Ma, R. T. Pinker, M. M. Wonsick, T. Koike, S. J. Cox, Y. Zhang, and P. Stackhouse (2008b), Evaluation of satellite estimates of downward shortwave radiation over the Tibetan Plateau, *Journal of Geophysical Research*, *113*(17).

Yang, K., J. Qin, X. Guo, D. Zhou, and Y. Ma (2009), Method development for estimating sensible heat flux over the Tibetan Plateau from CMA data, *Journal of Applied Meteorology and Climatology*, *48*(12), 2474-2486.

Yang, K., X. Guo, and B. Wu (2011a), Recent trends in surface sensible heat flux on the Tibetan Plateau, *Science China Earth Sciences*, *54*(1), 19-28.

Yang, K., X. Guo, J. He, J. Qin, and T. Koike (2011b), On the climatology and trend of the atmospheric heat source over the Tibetan Plateau: An experiments-supported revisit, *Journal of Climate*, *24*(5), 1525-1541.

Yang, K., B. Ye, D. Zhou, B. Wu, T. Foken, J. Qin, and Z. Zhou (2011c), Response of hydrological cycle to recent climate changes in the Tibetan Plateau, *Climatic Change*, *109*(3), 517-534.

Yang, K., B. Ding, J. Qin, W. Tang, N. Lu, and C. Lin (2012), Can aerosol loading explain the solar dimming over the Tibetan Plateau?, *Geophysical Research Letters*, *39*(20), L20710.

Yang, K., H. Wu, J. Qin, C. Lin, W. Tang, and Y. Chen (2014), Recent climate changes over the Tibetan Plateau and their impacts on energy and water cycle: A review, *Global and Planetary Change*, *112*, 79-91.

Yao, Y., S. Liang, Q. Qin, K. Wang, and S. Zhao (2011a), Monitoring global land surface drought based on a hybrid evapotranspiration model, *International Journal of Applied*

Earth Observation and Geoinformation, *13*(3), 447-457.

Yao, Y., S. Liang, Q. Qin, K. Wang, S. Liu, and S. Zhao (2011b), Satellite detection of increases in global land surface evapotranspiration during 1984-2007, *International Journal of Digital Earth*, 1-20.

Yatagai, A., K. Kamiguchi, O. Arakawa, A. Hamada, N. Yasutomi, and A. Kitoh (2012), APHRODITE: Constructing a long-term daily gridded precipitation dataset for Asia based on a dense network of rain gauges, *Bulletin of the American Meteorological Society*, *93*(9), 1401-1415.

Ye, D., and Y. Gao (1979), *The meteorology of the Qinghai-Xizang (Tibet) Plateau (in Chinese)*, Science Press, Beijing.

Ye, D., and G. Wu (1998), The role of the heat source of the Tibetan Plateau in the general circulation, *Meteorology and Atmospheric Physics*, *67*(1-4), 181-198.

Ye, J., F. Li, G. Sun, and A. Guo (2010), Solar dimming and its impact on estimating solar radiation from diurnal temperature range in China, 1961–2007, *Theoretical and Applied Climatology*, *101*(1-2), 137-142.

Yim, S.-Y., J.-G. Jhun, R. Lu, and B. Wang (2010), Two distinct patterns of spring Eurasian snow cover anomaly and their impacts on the East Asian summer monsoon, *Journal of Geophysical Research*, *115*(D22), D22113.

Yim, S.-Y., B. Wang, J. Liu, and Z. Wu (2013), A comparison of regional monsoon variability using monsoon indices, *Climate Dynamics*, 1-15.

You, Q., A. Sanchez-Lorenzo, M. Wild, D. Folini, K. Fraedrich, G. Ren, and S. Kang (2012), Decadal variation of surface solar radiation in the Tibetan Plateau from observations, reanalysis and model simulations, *Climate Dynamics*, 1-14.

Yu, G. R., X. F. Wen, X. M. Sun, B. D. Tanner, X. Lee, and J. Y. Chen (2006), Overview of ChinaFLUX and evaluation of its eddy covariance measurement, *Agricultural and Forest Meteorology*, *137*(3-4), 125-137.

Yu, R., J. Li, W. Yuan, and H. Chen (2010), Changes in characteristics of late-summer precipitation over eastern China in the past 40 years revealed by hourly precipitation data, *Journal of Climate*, *23*(12), 3390-3396.

Zhang, G., Y. Zhang, J. Dong, and X. Xiao (2013), Green-up dates in the Tibetan Plateau have continuously advanced from 1982 to 2011, *Proceedings of the National Academy of Sciences of the United States of America*, *110*(11), 4309-4314.

Zhang, J., L. Wu, G. Huang, W. Zhu, and Y. Zhang (2011a), The role of May vegetation greenness on the southeastern Tibetan Plateau for East Asian summer monsoon prediction, *Journal of Geophysical Research*, *116*(D5), D05106.

Zhang, J., L. Wu, and W. Dong (2011b), Land-atmosphere coupling and summer climate variability over East Asia, *Journal of Geophysical Research*, *116*(D5), D05117.

Zhang, K., J. S. Kimball, Q. Mu, L. A. Jones, S. J. Goetz, and S. W. Running (2009), Satellite based analysis of northern ET trends and associated changes in the regional water balance from 1983 to 2005, *Journal of Hydrology*, *379*(1–2), 92-110.

Zhang, K., J. S. Kimball, R. R. Nemani, and S. W. Running (2010), A continuous satellite-derived global record of land surface evapotranspiration from 1983 to 2006, *Water Resources Research*, *46*(9), W09522.

Zhang, Y.-C., W. B. Rossow, and A. A. Lacis (1995), Calculation of surface and top of atmosphere radiative fluxes from physical quantities based on ISCCP data sets: 1. Method and sensitivity to input data uncertainties, *Journal of Geophysical Research*, *100*(D1), 1149-1165.

Zhang, Y., W. B. Rossow, A. A. Lacis, V. Oinas, and M. I. Mishchenko (2004a), Calculation of radiative fluxes from the surface to top of atmosphere based on ISCCP and other global data sets: Refinements of the radiative transfer model and the input data, *Journal of Geophysical Research*, *109*(D19), D19105.

Zhang, Y. S., T. Li, and B. Wang (2004b), Decadal change of the spring snow depth over the Tibetan Plateau: The associated circulation and influence on the East Asian summer monsoon, *Journal of Climate*, *17*(14), 2780-2793.

Zhu, X., Y. Liu, and G. Wu (2012), An assessment of summer sensible heat flux on the Tibetan Plateau from eight data sets, *Science China Earth Sciences*, *55*(5), 779-786.

Zou, H. (2006), The adaptive lasso and its oracle properties, *Journal of the American Statistical Association*, *101*(476), 1418-1429.